

**Department of Physics and Astronomy
University of Heidelberg**

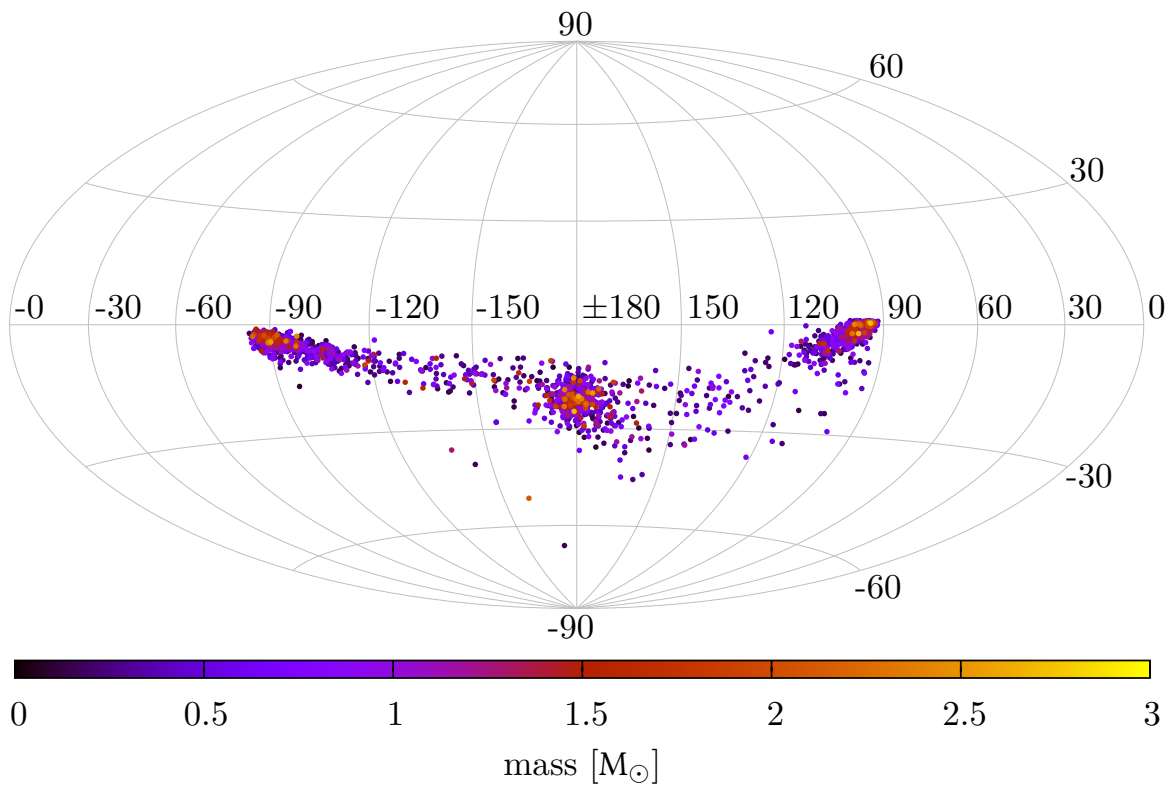
Bachelor Thesis in Physics
submitted by

Tobias Buck

born in Eutin (Germany)

2013

Dynamical analysis of the Hyades star cluster using direct N -body simulations



This Bachelor Thesis has been carried out by Tobias Buck at the
Astronomisches Rechen-Institut in Heidelberg
under the supervision of
Prof. Dr. Andreas Just

“The story so far: In the beginning the Universe was created. This has made a lot of people very angry and been widely regarded as a bad move.”

(Douglas Adams)

Zusammenfassung

In dieser Arbeit wird die Dynamik der Hyaden auf Grundlage von direkten N -Körper Einzelstern-Simulationen von King Modellen des King-Parameters $W_0 = 6$ und neuen Pan-STARRS1 Beobachtungsdaten studiert. Die Auswirkung des anfänglichen Verhältnisses von Jacobiradius und 99% Massenradius auf die Entwicklung der Massensegregation und das kumulative Massenprofil wird untersucht. Durch Vergleich der kumulativen Massenprofile verschiedener Modelle mit dem Massenprofil der Beobachtungsdaten wird das ursprüngliche Verhältnis von R_{Jac} zu $R_{99\%}$ für die Hyaden bestimmt. Für diese Modell wird die Auswirkung der zufälligen Initialisierung der anfänglichen Massenfunktion (IMF) im Simulationsprogramm durch zehn Simulationen mit unterschiedlichen Zufallszahlen untersucht. Die Auswirkungen der Konvergenzpunktmethode auf die Abstandsbestimmung der Sterne und die Geschwindigkeitsdispersion wird untersucht. Das beste Modell des Ensembles wird dann weiter auf die Haufenform untersucht. Dieses Modell besitzt eine anfängliche Masse von $1697 M_\odot$, eine ursprüngliche Anzahl von 2750 Sternen und ein anfängliches Verhältnis von Jacobiradius zu 99% Massenradius von 0.44. Die Entfernungsbestimmung anhand der Konvergenzpunktmethode zeigt einen systematischen Fehler von bis zu 4% und die Geschwindigkeitsdispersion in den Simulationen ist um fast einen Faktor zwei kleiner als in den Beobachtungen. Deshalb müssen weitere Simulationen mit Doppelsternen durchgeführt werden um die Unterschiede in der Geschwindigkeitsdispersion genauer zu untersuchen.

Abstract

This thesis studies the dynamics of the Hyades based on direct N -body single star simulations of King models with King parameter $W_0 = 6$ and new observational data from Pan-STARRS1. The effect of initial ratio of Jacobi radius to 99% mass radius on both the mass segregation and the cumulative mass profile is analyzed. By comparing the cumulative mass profiles of different models with that of the observations the initial ratio of R_{Jac} to $R_{99\%}$ for the Hyades will be determined. For this model an ensemble run with ten different random number seeds for initialization is done. The effects of the convergent point method on the distance determination of the stars and the velocity dispersion is investigated. The best fitting model of the ensemble is then further investigated for the cluster shape. This model has an initial mass of $1697 M_\odot$, an initial number of 2750 stars and an initial ratio of Jacobi radius to 99% mass radius of 0.44. For the distance determination with the convergent point method, a systematic error of up to 4% is calculated and the comparison between the simulated and observed velocity dispersion reveals a difference of a factor of two. Therefore further simulations including binaries are required.

Contents

1.	<i>Introduction</i>	1
1.1.	Outline	2
2.	<i>Potential theory</i>	5
2.1.	Basic principles	5
2.2.	Potential energy	8
3.	<i>Open star clusters - Models and properties</i>	11
3.1.	Jacobi radius	11
3.2.	Collisionless Boltzmann Equation	13
3.3.	King Model	16
3.3.1.	Cluster shape	18
3.3.2.	Velocity dispersion	20
3.4.	Galactic potential	23
4.	<i>Distance determination with the convergent point method</i>	25
4.1.	Transformation of proper motion	25
4.2.	Convergent point method	27
4.2.1.	Distance determination	28
5.	<i>NBODY6TID</i>	31
5.1.	Individual and block time steps	33
5.2.	Ahmad-Cohen scheme	33
5.3.	Nbody-units	34
5.4.	Input files	36
5.4.1.	Input file: <i>galax.dat</i>	36

Contents

5.4.2. Input file: <i>inmodel</i>	36
5.5. Path integration	37
5.6. Star cluster initialization	39
6. <i>Observations</i>	41
6.1. Membership determination	42
6.1.1. Kinematic selection of candidates	42
6.1.2. Photometric membership determination	43
6.2. Observational quantities	44
6.2.1. Cumulative mass profile	44
6.2.2. Kolmogorov-Smirnov-test	44
6.2.3. Mass function	45
6.2.4. Mass segregation	46
6.2.5. Velocity dispersion	47
7. <i>Simulation results</i>	49
7.1. Calculation of the scaling factor \bar{R}	49
7.2. Data processing	50
7.3. Ensemble 2750W6	51
7.3.1. Initial mass function and stellar evolution	52
7.3.2. Cumulative mass profile	54
7.3.3. Present-day mass function	56
7.3.4. Density profile	58
7.3.5. Mass segregation	59
7.4. Evolutionary effect of initial ratio of Jacobi radius to 99% mass radius	61
7.4.1. Mass profile - final ratio of half-mass radius to Jacobi radius	62
7.4.2. Agreement of observation and simulation for different ratios of Jacobi radius to 99% mass radius	65
7.4.3. Mass segregation: Minimum spanning tree	66
7.5. Velocity dispersion, kinematic distance and cluster shape	68
7.5.1. Velocity dispersion	68
7.5.2. Kinematic distance	72
7.5.3. Cluster shape	76

8. Conclusion	81
A. Appendix	85
A.1. Physical constants	85
A.2. Detailed discussion of the Kolmogorov-Smirnov-test	85
A.3. Additional data	87
A.4. Additional diagrams	90
<i>References</i>	93
<i>List of Figures</i>	97
<i>List of Tables</i>	99

1. Introduction

The Hyades, within Germany also known as "rain stars" ("Regengestirn") and further listed as *Melotte 25* or *Collinder 50*, is an open star cluster located in the constellation of Taurus, close to the Pleiades ("Seven Sisters"). They can be seen on the northern sky from September to April. Its age is about 625 Myr and it comprises about 700 stars with a total mass of about $460 M_{\odot}$ within a radius of 30 pc from the cluster centre (Goldman et al. [in press]). Because of its proximity to the Sun of just 46 pc there are very good observational data (Röser et al. [2011]). In this work direct N -body simulations are run to model the Hyades cluster, compare it to the observational data and to study the dynamics within the cluster. Previous simulations of the Hyades were done by Ernst et al. [2011] (also see references therein) with the direct N -body code `NBODY6TIDGPU`, which is based on `Nbody6` (see Aarseth [1999], Aarseth [2003] and Nitadori & Aarseth [2012]). These studies tried to model the Hyades using an older set of data (Röser et al. [2011]), providing masses, positions and velocities for the probable member stars.

The basis for this work is an observational data set of the Hyades provided by Goldman et al. [in press], which presents 41 new candidates as Hyades member stars down to masses as low as $0.1 M_{\odot}$. Thus the declining faint end of the initial mass function (IMF) indicated by the sample of Röser et al. [2011] is confirmed. Therefore during a lab a model IMF was adapted from the observational data to simulate the Hyades. In this work the present-day mass function, the cumulative mass profile and the mass segregation will be investigated. In order to find the optimal model for the Hyades, simulations with different initial ratios of R_{Jac} to $R_{99\%}$ were run and tested for the influence on the cumulative mass profile. In this connection an initial Roche lobe overfilling of the Hyades at the time of their formation was discovered. In a second step the effect of the membership determination on the kinematics of the cluster was analyzed. The membership is determined with the convergent point method (van Leeuwen [2009]) calculating the distances of the stars from their proper motions and

1. Introduction

the assumption that all stars in the cluster share the same velocity. But since the stars follow their individual orbits there has to be a velocity dispersion, such that the distance calculated from the convergent point method must contain an uncertainty. By applying the convergent point method to the stars in the simulation and comparing the result to the actual distance given in the simulation, the uncertainty on the distance determination and the velocity dispersion was estimated. As result a systematic error of up to 4% on the distance determination was found.

1.1. Outline

This thesis is structured as follows:

1. The theoretical background and the potential theory of stellar systems are presented.
2. The Jacobi radius will be introduced and the family of King models as special star cluster models will be shortly discussed. Moreover the Plummer-Kuzmin model as an analytical model of the Milky Way will be illustrated.
3. The convergent point method and its application to the distance determination of stars from their proper motion will be detailed.
4. The observational data set and the membership determination of the Hyades stars will be explained.
5. The simulation program `NBODY6TID` will be introduced and its use exemplified. In addition the initial parameters for the velocity and the position of the Hyades are calculated.
6. The results of the simulations are presented, compared to the observations and discussed.

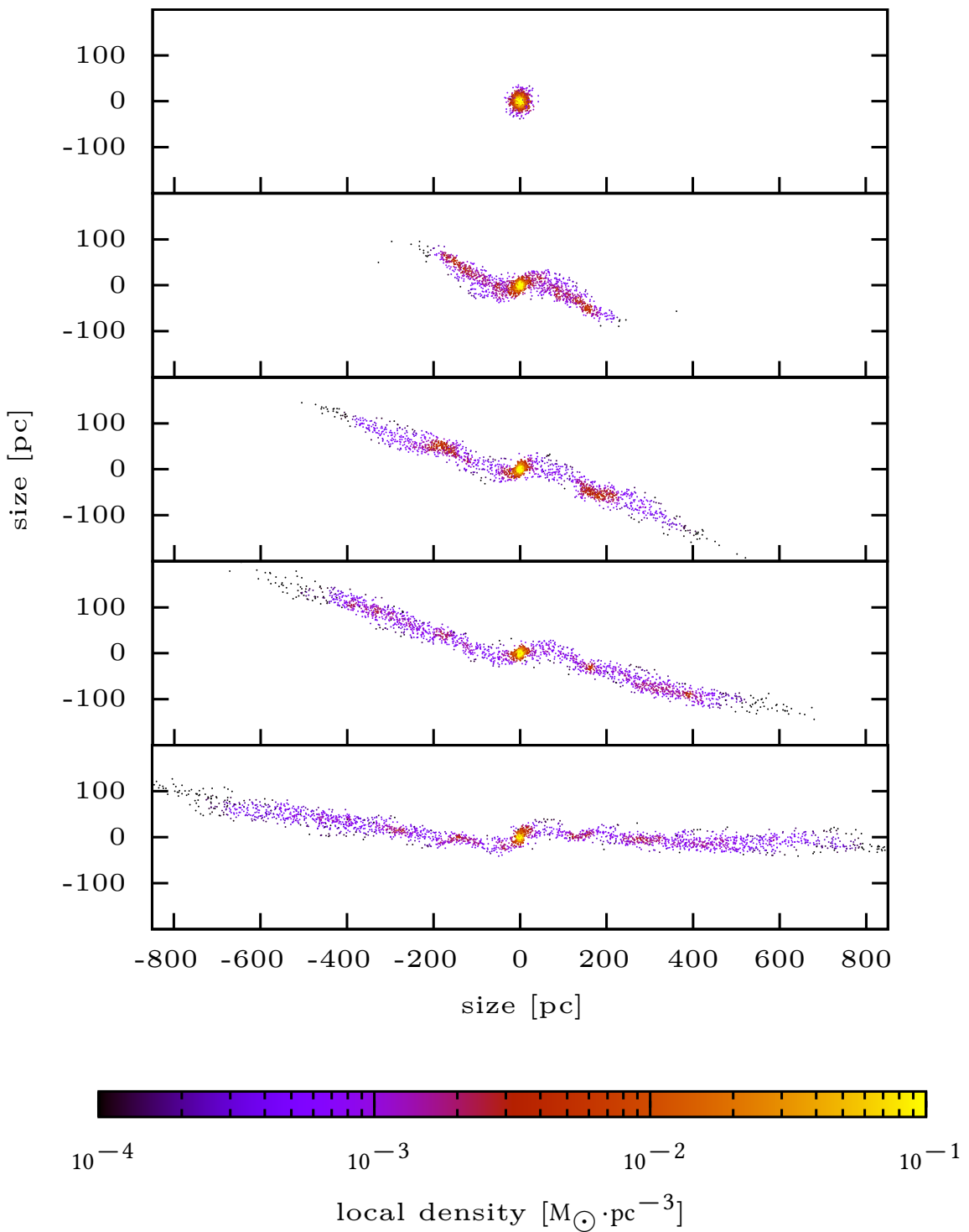


Fig. 1.1.: Tidal tails of the Hyades as they evolve in the simulation 2750W6. The color coding represents the local density in logarithmic scale. *The top panel* shows the Hyades at the beginning of the simulation (after ≈ 6 Myr). *The second panel* shows the tidal tails after 200 Myr of evolution, the *third panel* shows the tidal tails after 306 Myr, the *fourth panel* after 412 Myr and *the bottom panel* shows the tidal tails as they are at present-day.

2. Potential theory

To calculate the orbits of stars in a star cluster one needs the total gravitational potential of the ensemble of stars forming the star cluster, the Galactic potential and the initial conditions. The potential of the star cluster can be calculated by simply adding up all single star potentials. But for a huge number of stars, like in star clusters, this becomes very complex. Therefore it is easier and for most calculations also sufficient to calculate the potential of a smooth density distribution formed by smoothing out the single stars. The connection between potential, density (and with this also the mass) and the force acting on each unit of mass within the considered system should be derived in this chapter. It will provide the theoretical background for the prescription of the dynamics within gravitationally bound systems following Binney & Tremaine [2008, eq. (2.1) to (2.18)]. Starting point for the derivation will be Newton's law of gravitation.

2.1. Basic principles

The differential *Newtonian law of gravitation* per unit mass at the position \mathbf{x} caused by a density distribution $\varrho(\mathbf{x}')$ reads as follows:

$$\delta\mathbf{F}(\mathbf{x}) = G \frac{\mathbf{x}' - \mathbf{x}}{|\mathbf{x}' - \mathbf{x}|^3} \delta m(\mathbf{x}') \quad (2.1a)$$

$$= G \frac{\mathbf{x}' - \mathbf{x}}{|\mathbf{x}' - \mathbf{x}|^3} \varrho(\mathbf{x}') \delta^3(\mathbf{x}') \quad (2.1b)$$

where G denotes the gravitational constant and $(\mathbf{x}' - \mathbf{x})$ is the distance between the position of the unit mass and the position of the mass element $\delta m(\mathbf{x})$. The total force $\mathbf{F}_{tot}(\mathbf{x})$ can be obtained by integrating over the whole space and thus by summing up

all contributions from the small volume elements $\delta^3(\mathbf{x}')$ at position \mathbf{x}' .

$$\mathbf{F}_{tot}(\mathbf{x}) = G \int \frac{\mathbf{x}' - \mathbf{x}}{|\mathbf{x}' - \mathbf{x}|^3} \varrho(\mathbf{x}') d\mathbf{x}' \quad (2.2)$$

With the vector identity for the gradient operator ∇_x

$$\nabla_x \left(\frac{1}{|\mathbf{x}' - \mathbf{x}|} \right) = \frac{\mathbf{x}' - \mathbf{x}}{|\mathbf{x}' - \mathbf{x}|^3} \quad (2.3)$$

it follows that the total force $\mathbf{F}_{tot}(\mathbf{x})$ may be written as

$$\mathbf{F}_{tot}(\mathbf{x}) = G \nabla_x \int \frac{\varrho(\mathbf{x})}{|\mathbf{x}' - \mathbf{x}|} d\mathbf{x}' \quad (2.4)$$

and therefore it holds that the gravitational force is conservative (its curl vanishes because the rotation of the gradient is zero) and with the expression for the gravitational potential

$$\Phi(\mathbf{x}) = -G \int \frac{\varrho(\mathbf{x}')}{|\mathbf{x}' - \mathbf{x}|} d\mathbf{x}' \quad (2.5)$$

it can be written as the gradient of a scalar potential:

$$\boxed{\mathbf{F}(\mathbf{x}) = -\nabla \Phi} \quad (2.6)$$

For clarity the subscript on the gradient operator ∇ is omitted.

The following contains the derivation of *Poisson's equation* and *Gauss's theorem*, which give the relation between the potential and the density and between the potential and the mass respectively. The starting point for the derivation of *Poisson's equation* will be Equation 2.2. By dividing this equation through the test mass m_t one obtains the force per unit test mass $\mathbf{F}_m(\mathbf{x})$. The divergence of this equation gives:

$$\nabla \cdot \mathbf{F}_m(\mathbf{x}) = G \int \nabla_x \cdot \frac{\mathbf{x}' - \mathbf{x}}{|\mathbf{x}' - \mathbf{x}|^3} \varrho(\mathbf{x}') d\mathbf{x}' \quad (2.7a)$$

and given that

$$\nabla_x \cdot \left(\frac{\mathbf{x}' - \mathbf{x}}{|\mathbf{x}' - \mathbf{x}|^3} \right) = 0 \quad \text{for } (\mathbf{x}' \neq \mathbf{x}) \quad (2.7b)$$

the only contribution to the integral of Equation 2.7a comes from the point $\mathbf{x} = \mathbf{x}'$. Hence the volume integration can be limited to a sufficiently small sphere with radius r around this point, so that the density $\varrho(\mathbf{x}')$ will be almost constant within this sphere. For this reason the density can be taken out of the integral and the remaining factors can be written as:

$$\nabla \cdot \mathbf{F}_m(\mathbf{x}) = G\varrho(\mathbf{x}) \int_{|\mathbf{x}'-\mathbf{x}| \leq r} \nabla_{\mathbf{x}} \cdot \left(\frac{\mathbf{x}' - \mathbf{x}}{|\mathbf{x}' - \mathbf{x}|^3} \right) d\mathbf{x}' \quad (2.7c)$$

This equation can be rewritten under the use of the divergence theorem to convert the volume integral into a surface integral. For detailed derivation of the next step see [eq. (2.9a), BT, p. 57]. Equation 2.7a consequently becomes the form:

$$\nabla \cdot \mathbf{F}_m(\mathbf{x}) = -G\varrho \int d\Omega = -4\pi G\varrho(\mathbf{x}) \quad (2.8)$$

where $d\Omega$ is the element of solid angle. To obtain *Poisson's equation* one has to substitute $\nabla \cdot \mathbf{F}_m(\mathbf{x})$ with Equation 2.6. This gives the relation between potential Φ and density ϱ :

$$\boxed{\Delta\Phi = 4\pi G\varrho} \quad (2.9)$$

This equation becomes *Laplace's equation* for the special case of $\varrho = 0$.

$$\boxed{\Delta\Phi = 0} \quad (2.10)$$

In this equation $\Delta = \nabla^2$ is the *Laplacian*, the divergence of the gradient.

Now the step from *Poisson's equation* to *Gauss' theorem* is a simple one. Consider an arbitrary volume containing the total mass M . Integration of both sides of Equation 2.9 and applying the divergence theorem leads to

$$4\pi G \int \varrho d\mathbf{x} = 4\pi GM = \int \Delta\Phi d\mathbf{x} = \int \nabla\Phi d\mathbf{S} \quad (2.11)$$

where $d\mathbf{S}$ is a small surface element. Therefore *Gauss's theorem* shows that the closed surface integral over the gradient of the potential Φ is equal to the total enclosed mass M times $4\pi G$.

2.2. Potential energy

Following the derivation in Binney & Tremaine [2008, eq. (2.13-2.18)], the equation for the potential energy of a stellar system can be obtained by looking at the work done by bringing a test mass δm from infinity to the place \mathbf{x} under the influence of some potential $\Phi(\mathbf{x})$ caused by a density distribution $\varrho(\mathbf{x})$. The work done by this process is then simply $\delta m\Phi(\mathbf{x})$. This means one adds some increment $\delta\varrho(\mathbf{x})$ to the density distribution and thus the potential energy changes by:

$$\delta W = \int \delta\varrho(\mathbf{x})\Phi(\mathbf{x}) \, d\mathbf{x} \quad (2.12)$$

From *Poisson's equation* follows that the change in potential must satisfy the equation $\Delta(\delta\Phi) = 4\pi G(\delta\varrho)$ and therefore Equation 2.12 becomes:

$$\delta W = \frac{1}{4\pi G} \int \Phi \Delta(\delta\Phi) \, d\mathbf{x} \quad (2.13)$$

This can be rewritten using the divergence theorem and the fact that the surface integral vanishes for large r^1 .

$$\delta W = \frac{1}{4\pi G} \int \Phi \nabla \cdot (\delta\Phi) \, d\mathbf{S} - \frac{1}{4\pi G} \int \nabla\Phi \cdot \nabla(\delta\Phi) \, d\mathbf{x} \quad (2.14)$$

Equation 2.13 then becomes

$$\delta W = -\frac{1}{8\pi G} \delta \left(\int |\nabla\Phi|^2 \, d\mathbf{x} \right) \quad (2.15)$$

And hence the sum of all contributions δW leads to the equation for the total potential energy:

$$W = -\frac{1}{8\pi G} \int |\nabla\Phi|^2 \, d\mathbf{x} \quad (2.16)$$

¹The surface integral vanishes because for the potential it applies $\Phi \propto r^{-1}$ and for $r \rightarrow \infty$ $|\nabla\delta\Phi| \propto r^{-2}$, hence the integrand is proportional to r^{-3} while the total surface area of a sphere is proportional to r^2 . Furthermore $\frac{1}{2}\delta|\nabla\Phi| = \frac{1}{2}(\nabla\Phi \cdot \nabla\Phi) = \nabla\Phi \cdot \nabla(\delta\Phi)$.

Using once again the divergence theorem one obtains:

$$W = \frac{1}{2} \int \varrho(\mathbf{x}) \Phi(\mathbf{x}) d\mathbf{x} \quad (2.17)$$

For N individual stars in a star cluster the gravitational potential energy can also be defined by:

$$W = - \sum_{i=1}^N \sum_{j=1, i < j}^N G \frac{m_i m_j}{|\mathbf{x}_i - \mathbf{x}_j|} \quad (2.18)$$

where $m_{i,j}$ are the masses of the i^{th} and j^{th} star, G is the gravitational constant and $|\mathbf{x}_i - \mathbf{x}_j|$ is the distance between the considered stars. The restriction $i < j$ is needed because every pair of stars should appear only once in the sum.

3. Open star clusters - Models and properties

Within the Milky Way many small stellar systems of about 10^2 to a few times 10^6 stars can be found, called star clusters. In our Milky Way two different types can be distinguished (Binney & Tremaine [2008, p. 29]): The old and massive *globular clusters* contain 10^4 to 10^6 old stars of the same metallicity; Younger and smaller stellar systems consisting of 10^2 to 10^4 young stars are called *open clusters*. The latter are less compact stellar systems of stars of the same age and metallicity, originated from the same molecular cloud. Most *open clusters* in our Galaxy are younger than 1 Gyr and new open clusters continuously form in star forming regions in the Galactic disk (Binney & Tremaine [2008, p. 29]). Due to their low mass and the resulting weak mutual attraction of the stars, open star clusters loose their stars in the tidal field of the Galaxy and slowly dissolve. Therefore it is likely that a large fraction of stars in the Galactic disk have formed in open clusters which have been totally dissolved (Binney & Tremaine [2008, p. 29]).

This chapter deals with the *collisionless Boltzmann equation* as an analytical approach to describe the dynamics of a star cluster. It will introduce the two parametric King model for the description of star clusters and the Plummer-Kuzmin model as an analytical galaxy model used to describe the Milky Way. Furthermore the velocity dispersion and the star cluster shape in the tidal field of the Galaxy will be discussed.

3.1. Jacobi radius

Since open star clusters are systems of gravitationally bound stars in the tidal field of a galaxy, there has to be a limiting radius marking the border between bound and

unbound stars. For distances from the barycentre less than this limiting radius stars can be considered as gravitationally bound to the cluster (although there are a number of potential escapers within this limiting radius with Jacobi energies higher than the one needed to escape the cluster). For slightly larger radii the stars can be considered as loosely bound and for much higher radii the stars are no longer part of the star cluster. However this limiting radius is not well defined. A derivation for the value of this radius is given in King [1962]. It follows the approach that a value for this limiting radius can be obtained by calculating the distance between cluster barycentre and that point on the line connecting the cluster barycenter and the Galactic centre at which the acceleration acting on a star is zero with respect to the cluster barycentre. Therefore the relative acceleration between the cluster center and a star lying on the line between galactic centre and cluster barycentre has to be calculated. The acceleration of the cluster barycentre at radius R from the galactic centre is given by:

$$\frac{d^2}{dt^2}R = R\Omega^2 - \frac{d}{dR}\Phi_G \quad (3.1)$$

where the angular velocity is denoted by Ω and Φ refers to the Galactic potential. The acceleration of the star at radius R_s from the galactic centre is given by the equation:

$$\frac{d^2}{dt^2}R_s = R_s\Omega^2 - \left(\frac{d}{dR}\Phi \right)_{R_s} - \frac{GM(R_s - R)}{|R_s - R|^3} \quad (3.2)$$

The first two terms on the right side represent the acceleration of the star due to its orbit around the galactic centre, the second part describes the impact of the cluster mass M on the star's acceleration. From Equation 3.1 and Equation 3.2 the relative acceleration of the star with respect to the cluster barycentre is:

$$\begin{aligned} \frac{d^2}{dt^2}(R_s - R) &= (R_s - R)\Omega^2 - \left(\frac{d}{dR}\Phi \right)_{R_s} + \frac{d}{dR}\Phi - \frac{GM(R_s - R)}{|R_s - R|^3} \\ &\simeq \left(\Omega^2 - \frac{d^2}{dR^2}\Phi - \frac{GM}{|R_s - R|^3} \right) (R_s - R) \end{aligned} \quad (3.3)$$

Where the approximation

$$\frac{\frac{d}{dR}\Phi - \left(\frac{d}{dR}\Phi\right)_{R_s}}{(R - R_s)} \cong \frac{d^2}{dR^2}\Phi \quad (3.4)$$

for small values of $(R - R_s)$ was used to simplify the equation. For $\frac{d^2}{dt^2}(R_s - R) = 0$ the non-trivial solution to Equation 3.3 gives the formula for the limiting radius $R_{Jac}^3 := |R_s - R|^3$.

$$R_{Jac}^3 = \frac{GM}{\Omega^2 - \frac{d^2}{dR^2}\Phi} \quad (3.5)$$

Using the definition of the epicycle frequency κ

$$\kappa^2 = \frac{d^2}{dR^2}\Phi + 3\Omega^2 \quad (3.6)$$

(compare Binney & Tremaine [2008, p. 165, eq. (3.79a) and (3.79c)])

this reduces to:

$$R_{Jac} = \left(\frac{GM}{4\Omega^2 - \kappa^2} \right)^{\frac{1}{3}} \quad (3.7)$$

And using the term $\beta = \frac{\kappa}{\Omega}$ we can write R_{Jac} as:

$$R_{Jac} = \left(\frac{GM}{(4 - \beta^2)\Omega^2} \right)^{\frac{1}{3}} \quad (3.8)$$

where β^2 equals 1 for a Kepler potential and $\beta^2 = 2$ for a galaxy with flat rotation curve.

3.2. Collisionless Boltzmann Equation

By approximating the potential of N individual stars through a smooth potential of a density distribution, the calculated orbit of a star will deviate from the actual orbit the star would take in the unsmoothed potential. The timescale needed to significantly change the orbit of the star in the smooth potential compared to the orbit in

the unsmoothed potential is called *relaxation time* t_{relax} (Binney & Tremaine [2008, p. 37]). The deviation of the orbit in the actual N star potential compared to the smoothed potential is small for timescales smaller than the relaxation time. In certain approximation, the relaxation time can be defined as:

$$t_{\text{relax}} = 0.1 \frac{N}{\ln(N)} t_{\text{cross}} \quad (3.9)$$

where $t_{\text{cross}} = R/v$ is the *crossing time* defined by the radius R of the cluster and its central velocity dispersion v , the typical timescale needed for a star to cross the cluster ($t_{\text{cross}} \sim t_{\text{dyn}}$ Binney & Tremaine [2008, eq. (2.40)]), and N is the number of stars in the cluster. The factor 0.1 results from the actual calculation with impact parameters (see Binney & Tremaine [2008, p. 36]). For the Hyades the initial crossing time can be calculated with the parameters given in Table 7.2 to $t_{\text{cross}} \approx 20$ Myr and thus the initial relaxation time is calculated to $t_{\text{relax}} \approx 1.3$ Gyr. This value is more than twice as large as the Hyades age of 625 Myr. From this it follows, that it is appropriate to start the star cluster model in dynamical equilibrium since the star cluster would relax into dynamical equilibrium after a few *crossing times*, which is much shorter than the lifetime of the cluster. Furthermore it is appropriate to describe the dynamics of the stars within the Hyades and the current state by a smooth potential. But the process of mass segregation acts on a timescale of the order of the *relaxation time* due to two-body relaxation, which can not be described by a smooth potential. The relaxation time for different star types is proportional to $M_{\text{star}}/m_{\text{mean}}$, where M_{star} is the mass of the considered star type and m_{mean} the mean stellar mass of the stars in the cluster. Therefore a direct N -body approach has to be undertaken.

The deduction of the *collisionless Boltzmann equation* in this section follows basically that in Binney & Tremaine [2008, p. 275-276]. At any time a full description of a collisionless system can be given for each type of stars by a distribution function (DF) $f(\mathbf{x}, \mathbf{v}, t) \geq 0$ specifying the probability $p = f(\mathbf{x}, \mathbf{v}, t) d\mathbf{x} d\mathbf{v}$ of finding a star at time t with position in the small space volume $d\mathbf{x}$ around \mathbf{x} and velocity in the small velocity range $d\mathbf{v}$ around \mathbf{v} . With the initial conditions for position and velocity $f(\mathbf{x}, \mathbf{v}, t_0)$ for every star - and the Newtonian laws - the value for $f(\mathbf{x}, \mathbf{v}, t)$ for every time t is known. In phase space the movement of the stars around their orbits can be described

by a six-dimensional coordinate vector \mathbf{w} and its six-dimensional velocity $\dot{\mathbf{w}}$:

$$\begin{aligned} (\mathbf{x}, \mathbf{v}) &\equiv \mathbf{w} \\ \dot{\mathbf{w}} = (\dot{\mathbf{x}}, \dot{\mathbf{v}}) &= (\mathbf{v}, -\nabla\Phi) \end{aligned} \tag{3.10}$$

The stars whose motion is described by $\dot{\mathbf{w}}$ drift smoothly through phase space, which means that the motion $\dot{\mathbf{w}}$ conserves stars, no new stars are created and no stars are destroyed. Therefore $f(\mathbf{w}, t)$ satisfies a continuity equation, such as the one used in fluid mechanics.

$$\frac{\partial f}{\partial t} + \sum_{\alpha=1}^6 \frac{\partial(f\dot{w}_\alpha)}{\partial w_\alpha} = 0 \tag{3.11}$$

By integrating this equation over some volume of phase space the meaning of this equation becomes clear. The first term describes the change with time of the probability of finding a star in the specified volume, while the second term describes the rate at which stars flow out of the considered volume. Equation 3.11 can be simplified with the following relation for $\dot{\mathbf{w}}$:

$$\sum_{\alpha=1}^6 \frac{\partial \dot{w}_\alpha}{\partial w_\alpha} = \sum_{i=1}^3 \left(\frac{\partial v_i}{\partial x_i} + \frac{\partial \dot{v}_i}{\partial v_i} \right) = \sum_{i=1}^3 -\frac{\partial}{\partial v_i} \left(\frac{\partial \Phi}{\partial x_i} \right) = 0 \tag{3.12}$$

In this equation the derivative $\left(\frac{\partial v_i}{\partial x_i}\right)$ becomes zero because the position x_i and the velocity v_i are independent coordinates of phase space. The second step follows because $\nabla\Phi$ is independent of the velocity. Plugging this relation into Equation 3.11 leads to the *collisionless Boltzmann equation*:

$$\frac{\partial f}{\partial t} + \sum_{\alpha=1}^6 \dot{w}_\alpha \frac{\partial f}{\partial w_\alpha} = 0 \tag{3.13a}$$

or rewritten by using the definition of w this yields:

$$\frac{\partial f}{\partial t} + \sum_{i=1}^3 \left(v_i \frac{\partial f}{\partial x_i} - \frac{\partial \Phi}{\partial x_i} \frac{\partial f}{\partial v_i} \right) = 0 \tag{3.13b}$$

and in vector notation this equation becomes:

$$\frac{\partial f}{\partial t} + \mathbf{v} \cdot \nabla f - \nabla \Phi \cdot \frac{\partial f}{\partial \mathbf{v}} = 0 \quad (3.13c)$$

This can also be written with Hamilton's formalism (see Binney & Tremaine [2008, p. 797]) if we consider $\mathbf{w} = (\mathbf{x}, \mathbf{v}) = (\mathbf{q}, \mathbf{p})$ and $\dot{\mathbf{w}} = (\dot{\mathbf{x}}, \dot{\mathbf{v}}) = (\dot{\mathbf{q}}, \dot{\mathbf{p}})$ as arbitrary canonical variables. Subsequently Equation 3.13a becomes:

$$\frac{\partial f}{\partial t} + \dot{\mathbf{q}} \frac{\partial f}{\partial \mathbf{q}} + \dot{\mathbf{p}} \frac{\partial f}{\partial \mathbf{p}} = 0 \quad (3.14)$$

And by substituting *Hamilton's equations*:

$$\dot{\mathbf{q}} = \frac{\partial H}{\partial \mathbf{p}} \quad \dot{\mathbf{p}} = -\frac{\partial H}{\partial \mathbf{q}} \quad (3.15)$$

into Equation 3.14, this can be written as:

$$\begin{aligned} 0 &= \frac{\partial f}{\partial t} + \frac{\partial f}{\partial \mathbf{q}} \cdot \frac{\partial H}{\partial \mathbf{p}} - \frac{\partial f}{\partial \mathbf{p}} \cdot \frac{\partial H}{\partial \mathbf{q}} \\ &= \frac{\partial f}{\partial t} + [f, H] \end{aligned} \quad (3.16)$$

where in the last step the second and third term were rewritten under the use of the *Poisson bracket* (see Binney & Tremaine [2008, p. 800]).

If the number of stars is not conserved, which can be true for times larger than the relaxation time t_{relax} , the *collisionless Boltzmann equation* should be adjusted by a correction term on the left side of Equation 3.16. Since this is not the case for the Hyades this will not be discussed here.

3.3. King Model

Star clusters are not unlimited in spatial extent. The tidal forces of the host galaxy set a finite boundary to their spatial extent. Thus star clusters are objects consisting of a finite number of stars with finite velocities limited by the velocity required to reach the outer boundary of the cluster, where the tidal forces of the galaxy can rip the

stars away. Such models with a certain cutoff velocity were discussed by King [1966]. According to King [1966] a suitable distribution function for the energy of the stars in the cluster is given by:

$$f_K(\varepsilon) = \begin{cases} \zeta \left[\exp\left(\frac{\varepsilon}{\sigma^2}\right) - 1 \right] & \varepsilon > 0 \\ 0 & \varepsilon \leq 0 \end{cases} \quad (3.17)$$

where $\zeta = \rho (2\pi\sigma^2)^{-\frac{3}{2}}$ is some constant and $\varepsilon = \Psi(r) - \frac{v^2}{2}$ is the relative energy. For the relative potential $\Psi(r) = \Phi_t - \Phi(r)$ the constant Φ_t is chosen such that at the outer boundary of the star cluster the relative potential Ψ vanishes (see Binney & Tremaine [2008, p. 222,232]). Thus a relative energy of zero corresponds to the ability to reach the outer boundary of the star cluster.

King models can be simply characterized by one parameter W_0 , called the King parameter. The King parameter is given by:

$$W_0 = \frac{\Psi(0)}{\sigma^2} \quad (3.18)$$

where $\Psi(0)$ is the value for the potential in the cluster centre and σ the King velocity dispersion (Binney & Tremaine [2008, p. 235]) as in Equation 3.17. The King radius r_K describes the size of the flat core and can be expressed in terms of the central density ϱ_0 , the King velocity dispersion σ and the gravitational constant:

$$r_K = \sqrt{\frac{9\sigma^2}{4\pi G\varrho_0}} \quad (3.19)$$

Another characteristic value is the "concentration" c of a King model, where:

$$c = \log_{10}\left(\frac{r_t}{r_K}\right) \quad (3.20)$$

r_t is the limiting radius: the radius where the density of the King model drops to zero. It is not equal to the Jacobi radius presented in Equation 3.8. To obtain the density of the King model Equation 3.17 is written in terms of Ψ as well as the velocity v and then integrated over all velocities. This yields the density in terms of Ψ and therefore

implicitly for all radii.

$$\begin{aligned}\varrho_K(\Psi) &= 4\pi\zeta \int_0^{\sqrt{2\Psi}} \left[\exp\left(\frac{\Psi - \frac{1}{2}v^2}{\sigma^2}\right) - 1 \right] v^2 dv \\ &= \rho \left[\exp\left(\frac{\Psi}{\sigma^2}\right) \operatorname{erf}\left(\frac{\sqrt{\Psi}}{\sigma}\right) - \sqrt{\frac{4\Psi}{\pi\sigma^2}} \left(1 + \frac{2\Psi}{3\sigma^2}\right) \right]\end{aligned}\quad (3.21)$$

In this equation erf is the error function. By substituting this into *Poisson's equation* (Equation 2.9) and integrating it numerically one can obtain the potential Ψ as a function of the radius r . Resubstituting this into Equation 3.21 yields then the density ϱ_k as a function of the radius.

3.3.1. Cluster shape

The cluster shape of Roche volume filling clusters in the presence of the tidal field of the Galaxy is not spherical as for an isolated cluster. However the shape of the star cluster in the tidal field can be investigated by looking at the last closed equipotential surface of the effective potential and by calculating the cluster ellipsoid of the second order momenta of the space coordinates (compare Röser et al. [2011, ch. 5.1]). The effective potential Φ_{eff} of the star cluster can be expressed as the sum of the Galactic potential Φ_G and a term for the centrifugal potential Φ_c :

$$\Phi_{eff} = \Phi_G + \Phi_c \quad (3.22)$$

In Galactic coordinates and under the assumption of a Kepler potential for the cluster's gravitational potential, which is a good approximation for the outer part of the cluster's potential (see Ernst et al. [2010]), the effective potential to second order reads as follows:

$$\Phi_{eff} = \Phi_{eff,0} - \frac{GM}{\sqrt{x^2 + y^2 + z^2}} + \frac{1}{2} (\beta^2 - 4) \Omega^2 x^2 + \frac{1}{2} \delta^2 \Omega^2 z^2 \quad (3.23)$$

where β denotes, as before, the ratio of the epicycle frequency κ and the circular frequency Ω . δ denotes the dimensionless vertical frequency $\frac{\nu}{\Omega}$. The values for $(\beta, \delta) = (1.37, 2.86)$ were taken for the Milky Way for a cluster radius of 8 kpc. The value of the effective potential at the last closed equipotential surface can be calculated from

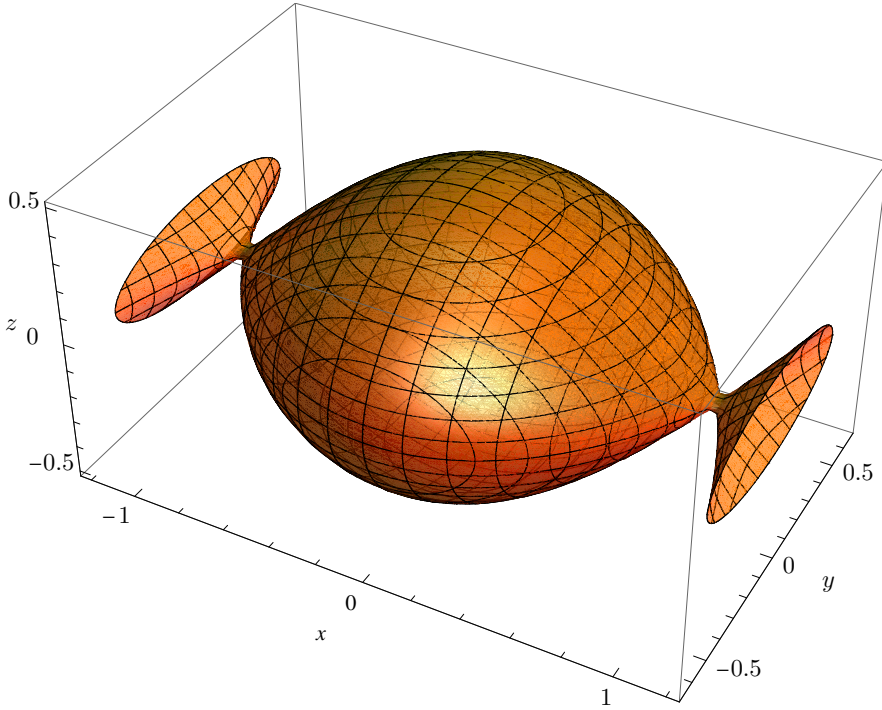


Fig. 3.1.: Sketch of the last closed equipotential surface of the effective potential of a star cluster in the tidal field of the Galaxy. The directions of the coordinate axis correspond to the orientation of the Galactic coordinate system.

the formula for the Jacobi radius (Equation 3.8) and Equation 3.23:

$$\Phi_{eff,last} = \Phi_{eff,0} - \frac{3}{2} \frac{GM}{r_{Jac}} \quad (3.24)$$

From this the dimension of the cluster in units of the Jacobi radius can be calculated. In x-direction this is simply the Jacobi radius $x_{max} = r_{Jac}$ itself while in y-direction this gives a value of $y_{max} = \frac{2}{3}r_{Jac}$. In z-direction the maximal distance from the cluster centre for the last closed equipotential surface is given by $z_{max} = 0.503 r_{Jac}$. A sketch of the last closed equipotential surface of a star cluster in the tidal field of the Galaxy can be found in Figure 3.1.

The second order momenta ellipsoid of the cluster can be calculated in the same way the moment of inertia tensor is calculated, just calculating the tensor without

weighting with the masses.

$$\mathcal{M} = \sum_{i=0}^N \begin{bmatrix} y_i^2 + z_i^2 & -x_i y_i & -x_i z_i \\ -y_i x_i & x_i^2 + z_i^2 & -y_i z_i \\ -z_i x_i & -z_i y_i & x_i^2 + y_i^2 \end{bmatrix} \quad (3.25)$$

This results in a symmetric tensor and hence this tensor can be diagonalized with the eigenvalues \hat{X} , \hat{Y} and \hat{Z} and the associated eigenvectors \hat{x} , \hat{y} and \hat{z} . The eigenvectors can be investigated to calculate the orientation of the cluster ellipsoid relative to the galactic coordinate system while the eigenvalues can be used to calculate the semi-major axis:

$$\eta_k = \frac{1}{\sqrt{\hat{k}}} \quad (3.26)$$

where η_k is the semi-major axis in the k^{th} direction and $k = \hat{x}, \hat{y}, \hat{z}$. The orientation of the ellipsoid is indicated by calculating the angles Ψ , Φ and Θ , whereat Ψ is the angle between the X-axis and the projection of \hat{x} onto the XZ-plane, Φ the angle between the X-axis and the projection of \hat{x} onto the XY-plane and Θ the angle between the Y-axis and the projection of \hat{y} onto the YZ-plane (see Figure 3.2).

3.3.2. Velocity dispersion

The velocity dispersion tensor is given by the equation:

$$\sigma_{ij}^2 \equiv \overline{(v_i - \bar{v}_i)(v_j - \bar{v}_j)} = \bar{v}_i \bar{v}_j - \bar{v}_i \bar{v}_j \quad (3.27)$$

Binney & Tremaine [2008, eq: 4.26]

where \bar{v}_i and \bar{v}_j are the mean values of the velocity in the considered direction and the mixed term $\bar{v}_i \bar{v}_j$ is given by:

$$\overline{v_i v_j} = \frac{1}{\mu(\mathbf{x})} \int v_i v_j f(\mathbf{x}, \mathbf{v}) d\mathbf{v} \quad \mu(\mathbf{x}) := \int f(\mathbf{x}, \mathbf{v}) d\mathbf{v} \quad (3.28)$$

In this connection $\mu(\mathbf{x})$ specifies the spatial probability density of finding a star at position \mathbf{x} independent of its velocity \mathbf{v} . For N individual stars with given velocities

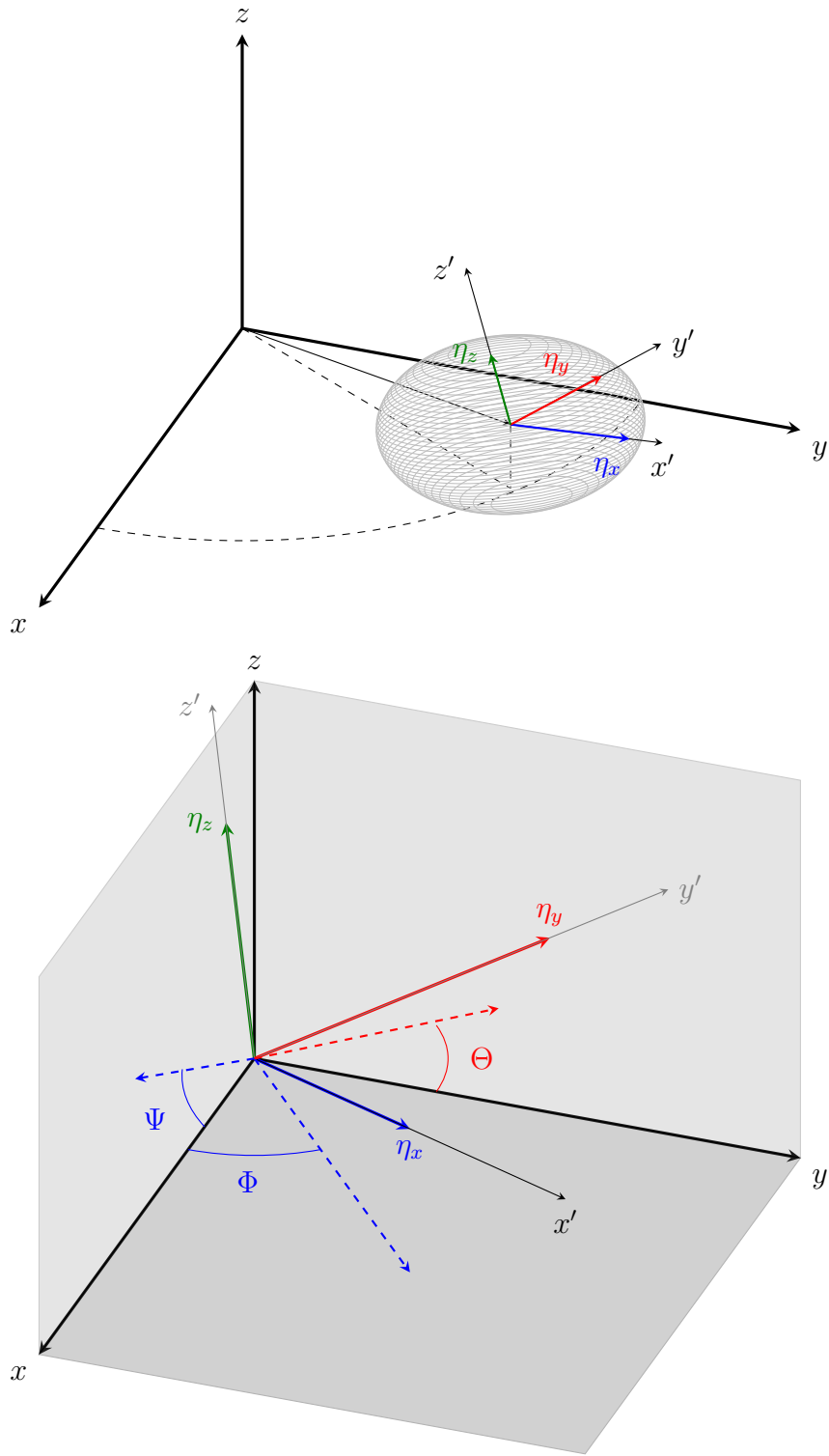


Fig. 3.2.: *Top* shows the star cluster ellipsoid and the orientation of its principal axis in the Galactic coordinate system. *Bottom* shows where the angles Ψ , Φ and Θ are measured to determine the orientation of the cluster ellipsoid.

this can be written as:

$$\overline{v_i v_j} = \frac{1}{N} \sum_{k=0}^N v_i v_j \quad (3.29)$$

Equation 3.27 yields for the three space directions the following velocity dispersion tensor:

$$\sigma^2 = \begin{bmatrix} \sigma_{xx}^2 & \sigma_{xy}^2 & \sigma_{xz}^2 \\ \sigma_{yx}^2 & \sigma_{yy}^2 & \sigma_{yz}^2 \\ \sigma_{zx}^2 & \sigma_{zy}^2 & \sigma_{zz}^2 \end{bmatrix} \quad (3.30)$$

This is as before the moment of inertia tensor a symmetric tensor so that one can find a basis B in which the tensor is diagonal with the eigenvalues $\sigma_{\hat{x}}$, $\sigma_{\hat{y}}$ and $\sigma_{\hat{z}}$.

$$\sigma^2 = \begin{bmatrix} \sigma_{\hat{x}}^2 & 0 & 0 \\ 0 & \sigma_{\hat{y}}^2 & 0 \\ 0 & 0 & \sigma_{\hat{z}}^2 \end{bmatrix} \quad (3.31)$$

The coordinate system B in which this tensor is diagonal build the principal axes for an ellipsoid with semi-major axis lengths given by $\frac{1}{\sigma_{\hat{x}}}$, $\frac{1}{\sigma_{\hat{y}}}$ and $\frac{1}{\sigma_{\hat{z}}}$. This ellipsoid is called *velocity ellipsoid*. And as before the relative orientation of the axis of the coordinate system B compared to the Galactic coordinate system yields the relative orientation of the velocity ellipsoid in the main coordinate system (see Figure 3.2).

For a star cluster in dynamical equilibrium (which is mainly true for stars within its Jacobi radius) the virial theorem $2T = -V$ holds approximately, where T is the total kinetic energy and V the total potential energy of the isolated cluster (Binney & Tremaine [2008, p. 360]). The kinetic energy of a star cluster is given by:

$$T = \frac{1}{2} \sum_{i=1}^N m_i v_i^2 = \frac{1}{2} M \langle v^2 \rangle \quad (3.32)$$

where N is the total number of stars in the system, m_i and v_i are the mass respectively the velocity of the individual stars, M the total mass of the system and $\langle v^2 \rangle$ is the mean-squared velocity of the system. Therefore from the virial theorem one can derive

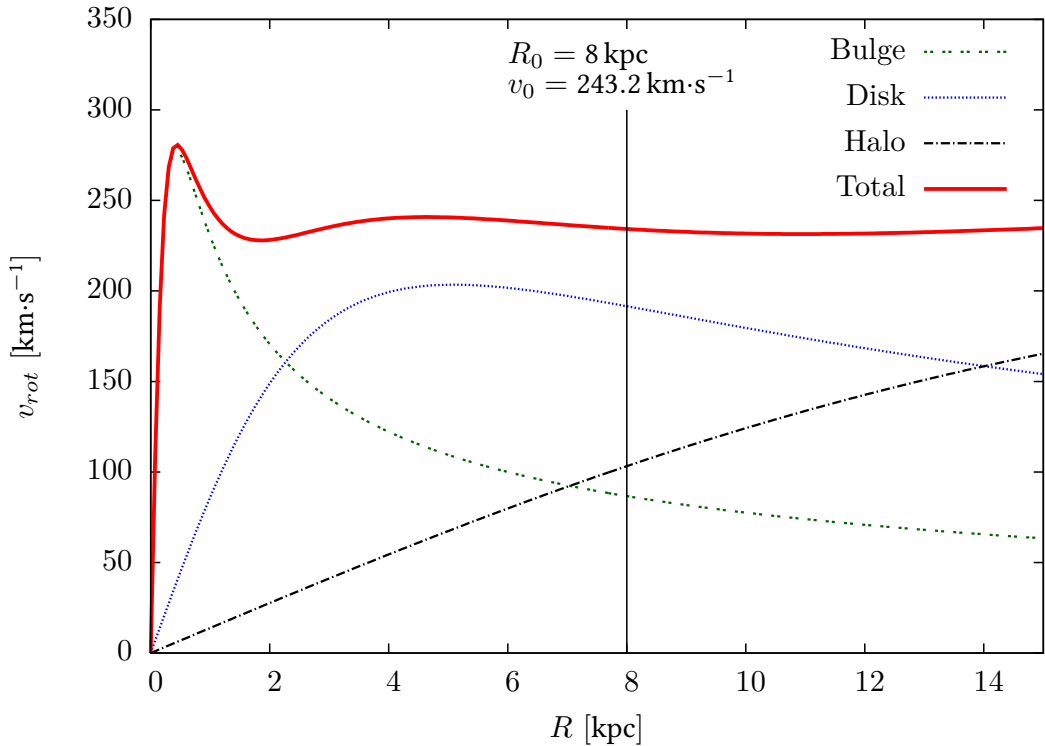


Fig. 3.3.: Rotation curve of the Milky Way. Shown are the rotation curves of the components of the Milky Way as well as the entire rotation curve of all components. The vertical line indicates the position of the sun at 8 kpc.

the squared velocity dispersion as follows:

$$\sigma^2 = \langle v^2 \rangle = \frac{|V|}{M} \quad (3.33)$$

This equation can be used to proof whether a given star cluster is in dynamical equilibrium or not.

3.4. Galactic potential

In this thesis a three-component Plummer-Kuzmin model is used to model the potential of the Milky Way, consisting of components for the Disk, the Bulge and the Halo. The Plummer-Kuzmin model is a composition of the spherical symmetric Plummer model and the axisymmetric Kuzmin disk (see Miyamoto & Nagai [1975]).

The Plummer model is a model with finite mass and corresponds to a stellar polytrope model of index $n = 5$. The distribution function is given by:

$$f_P(\varepsilon) = \begin{cases} \zeta \varepsilon^{7/2} & \varepsilon > 0 \\ 0 & \varepsilon \leq 0 \end{cases} \quad (3.34)$$

(Binney & Tremaine [2008, eq. (4.83)]) where $\varepsilon = \Psi(r) - \frac{v^2}{2}$ is the relative energy and $\Psi(r) = \Phi_t - \Phi(r)$ is the relative potential. The corresponding potential for the Plummer model is then given by:

$$\Phi_P(r) = -\frac{GM}{\sqrt{r^2 + b^2}} \quad (3.35)$$

(Plummer [1911], Binney & Tremaine [2008, eq. (2.44a)]). The equation for the potential of the Kuzmin disk in cylindrical coordinates (R, z) is given by:

$$\Phi_{KZ}(R, z) = -\frac{GM}{\sqrt{R^2 + (a + |z|)^2}} \quad (3.36)$$

(see Miyamoto & Nagai [1975], Binney & Tremaine [2008, eq. (2.68a)]). From Equation 3.35 and Equation 3.36 the potential of the Plummer-Kuzmin model follows as:

$$\Phi(R, z) = -\frac{GM}{\sqrt{R^2 + (a + \sqrt{z^2 + b^2})^2}} \quad (3.37)$$

which for $a = 0$ reduces to a Plummer model (Plummer [1911]) and for $b = 0$ to a flattened Kuzmin disk. The corresponding density distribution is given by:

$$\varrho(R, z) = \left(\frac{b^2 M}{4\pi} \right) \frac{a R^2 + (a + 3\sqrt{z^2 + b^2})(a + \sqrt{z^2 + b^2})^2}{\left[R^2 + (a + \sqrt{z^2 + b^2})^2 \right]^{5/2} (z^2 + b^2)^{3/2}} \quad (3.38)$$

(Miyamoto & Nagai [1975])

The parameters for the three-component Plummer-Kuzmin model of the Milky Way can be found in Table 5.1.

4. Distance determination with the convergent point method

For nearby star clusters like the Hyades the convergent point method is a suitable method to three-dimensionally resolve the star cluster. For this purpose the proper motions of individual stars are used to resolve the star cluster along the line of sight by determining the individual distances of the stars from the sun. This method was used by i.e. van Leeuwen [2009]; Röser et al. [2011] to resolve the Hyades three-dimensionally. Basic assumptions for this method are that all cluster-member stars have the same space velocity and that they have the same age and metallicity. Another advantage of this method is that by determining the membership through the proper motion the internal velocity dispersion can be estimated. The underlying equations for this method will be introduced in this chapter and the procedure of the convergent point method will be discussed.

4.1. Transformation of proper motion

The derivation of the connection between proper motion and space velocity follows from the conversion of spherical coordinates to cartesian coordinates and the time derivative of the position vector in spherical coordinates. The derivation given here follows the one in van Leeuwen [2009, eq. 1 to 6]. The position vector of a star or the cluster centre in the Galactic rectangular coordinate system X, Y, Z is $\mathbf{R} = [x, y, z]$, where X is the axis with direction towards the Galactic centre, Y the axis pointing in the direction of Galactic rotation and Z the axis pointing towards the Galactic north pole. The representation of the vector \mathbf{R} in Galactic longitude and latitude is given by

4. Distance determination with the convergent point method

the transformation into spherical coordinates $[R, l, b]$ by:

$$\mathbf{R} = R \cdot \begin{bmatrix} \cos(l) \cos(b) \\ \sin(l) \cos(b) \\ \sin(b) \end{bmatrix} \quad (4.1)$$

where $R = \sqrt{x^2 + y^2 + z^2}$ is the distance from the sun to this point and l and b are the Galactic longitude and accordingly the Galactic latitude of this point. From this the velocity vector can be determined by time derivative.

$$\dot{\mathbf{R}} = \begin{bmatrix} \cos(l) \cos(b) & -\sin(l) & -\cos(l) \sin(b) \\ \sin(l) \cos(b) & \cos(l) & -\sin(l) \cos(b) \\ \sin(b) & 0 & \cos(b) \end{bmatrix} \cdot \begin{bmatrix} \dot{R} \\ R \dot{l} \cos(b) \\ R \dot{b} \end{bmatrix} \quad (4.2)$$

In this connection the vector on the right relate to the observed velocity components. Therefore the components of this vector can be written in terms of the radial velocity and the proper motion.

$$\begin{aligned} \dot{R} &= V_{rad} \\ R \dot{l} \cos(b) &= \varkappa \frac{\mu_{l*}}{\varpi} \\ R \dot{b} &= \varkappa \frac{\mu_b}{\varpi} \end{aligned} \quad (4.3)$$

In this equation $\varkappa = 4.74047$ is the conversion factor from $1 \text{ mas}\cdot\text{yr}^{-1}$ at 1 kpc to $1 \text{ km}\cdot\text{s}^{-1}$, ϖ the secular parallax and $\mu_{l*} \equiv \mu_l \cos(b)$ the proper motion in l -direction, respectively μ_b the proper motion in b -direction. Now Equation 4.2 can be inverted and the observed velocity vector can be expressed in terms of the space velocity vector so that the transformation from space velocity to proper motion and radial velocity is given.

$$\begin{bmatrix} V_{rad} \\ \varkappa \frac{\mu_{l*}}{\varpi} \\ \varkappa \frac{\mu_b}{\varpi} \end{bmatrix} = \begin{bmatrix} \cos(l) \cos(b) & \sin(l) \cos(b) & \sin(b) \\ -\sin(l) & \cos(l) & 0 \\ -\cos(l) \sin(b) & -\sin(l) \cos(b) & \cos(b) \end{bmatrix} \cdot \dot{\mathbf{R}} \quad (4.4)$$

With this transformation and the assumption that all stars in a star cluster move with the same space velocity (which is assumed to be the space velocity of the cluster center) the proper motion of the individual stars for every point on the sky can be determined from the cluster's barycentre motion. For this the velocity vector of the cluster centre is left multiplied with the matrix from Equation 4.4, which for short now is called \mathbf{A}_i . The matrix from Equation 4.2 will be called \mathbf{A}_i^{-1} from now. The index i was added to reference individual stars in the cluster with individual (l_i, b_i) . So the relation between space velocity of the cluster centre $\dot{\mathbf{R}}$ and proper motion reads:

$$\mathbf{v}_i = \mathbf{A}_i \dot{\mathbf{R}} = \begin{bmatrix} V_{rad} \\ \varkappa \frac{\mu_{l*}}{\varpi} \\ \varkappa \frac{\mu_b}{\varpi} \end{bmatrix} \quad (4.5)$$

In the same way the space velocity vector for every point on the sky can be calculated from the observed proper motion, the observed parallax and the measured radial velocity by multiplying with the matrix from Equation 4.2.

$$\dot{\mathbf{R}} = \mathbf{A}_i^{-1} \mathbf{v}_i \quad (4.6)$$

4.2. Convergent point method

Stars of a star cluster are gravitational bound to each other and therefore share nearly the same space velocity apart from some internal velocity dispersion. Since not too distant star cluster occupy enough space at the sky, the projection of the space velocities of each star onto the plane perpendicular to the line of sight creates a direction towards a common point called convergent point (compare Figure 4.1). Another way to determine the direction towards the convergent point is to take the velocity of the centre of mass of the star cluster and calculate its projection onto the plane perpendicular to the line of sight. This vector directly points towards the convergent point. With the assumption that all cluster members share the same space velocity one can then establish a criteria to test the membership of stars to a certain star cluster by determining the distances to the stars by their proper motions. For that purpose the proper motion has to be split

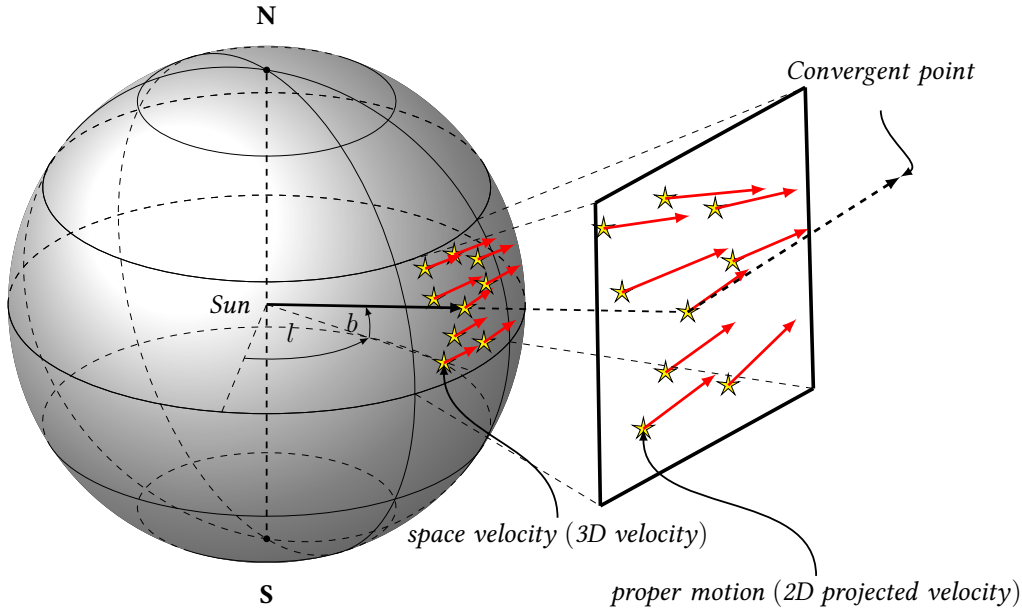


Fig. 4.1.: Connection between space velocity and proper motion and the occurrence of a convergent point as a result of projection. The red arrows on the sphere represent the nearly parallel space velocities of the stars while the arrows on the plane on the right represent the proper motion of the stars.

into a part parallel to the direction of the convergent point and one part perpendicular to that. If the velocities of the stars were all the same as the star cluster's centre of mass velocity the latter one would be zero. But since this is not true, the component of the proper motion perpendicular to the direction towards the convergent point can be used to study the velocity dispersion in a star cluster while the proper motion component parallel to the direction of the convergent point can be used to determine the distance to the star.

4.2.1. Distance determination

The actual direction towards the convergent point depends on the position on the sky. So for every star one has to calculate the appropriate direction towards the convergent point and from the given cluster velocity one has to calculate the predicted proper motion for this star. By comparing this value with the measured value for the proper motion, the secular parallax and hence the distance of the star can be determined.

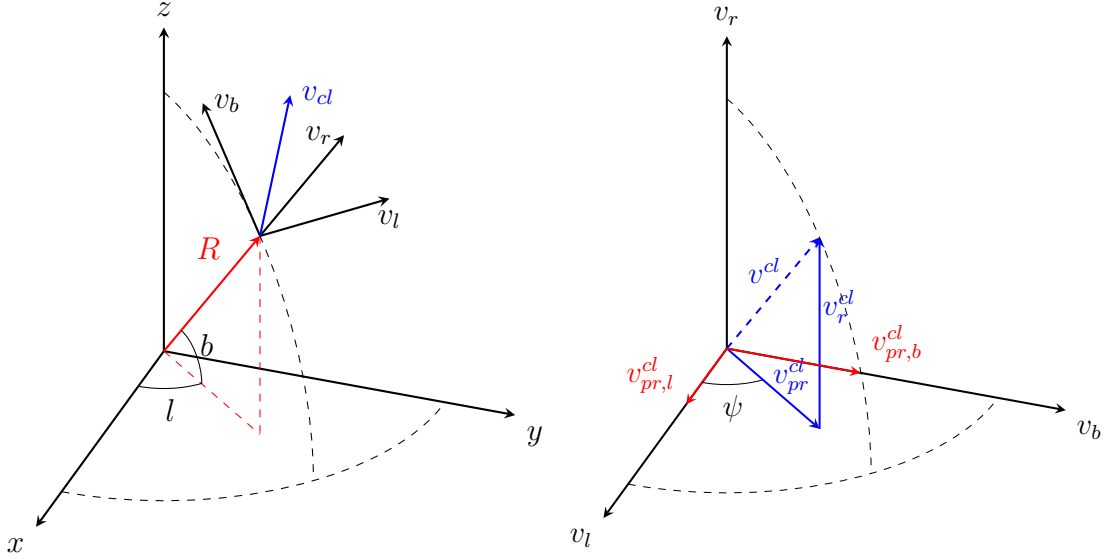


Fig. 4.2.: *Left* shows the position vector of a star cluster (red arrow), its space velocity (blue arrow) and the coordinate system for the cluster velocity with the three axis for radial velocity v_r and tangential velocity in l and b direction. *Right* shows the velocity coordinate system from the left and prescribes how the cluster velocity vector (blue dashed arrow) is decomposed into radial and tangential velocity vector (blue solid arrows). The red arrows indicate the velocity components in l and b direction.

Therefore a rotation has to be applied to the measured proper motion so that it is aligned with the direction towards the convergent point. This is done by multiplying the measured velocity vector given in Equation 4.5 with the matrix:

$$B_i = \begin{bmatrix} 1 & 0 & 0 \\ 0 & \cos(\psi_i) & \sin(\psi_i) \\ 0 & -\sin(\psi_i) & \cos(\psi_i) \end{bmatrix} \quad (4.7)$$

The angle ψ_i is determined for every star by the predicted proper motion calculated with equation Equation 4.5 from the cluster's space velocity:

$$\psi_i = \arctan \left(\frac{\mu_{b,i,p}}{\mu_{l*,i,p}} \right) \quad (4.8)$$

where the index p refers to the fact that the used proper motions are predicted ones. With this rotation the proper motion component parallel ($\mu_{||}$) to the direction towards

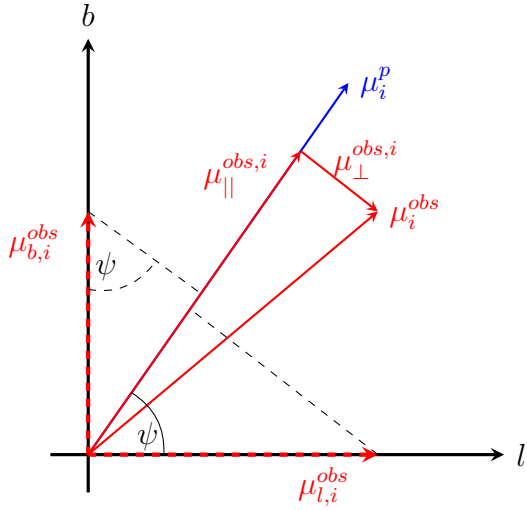


Fig. 4.3.: Observed proper motion components parallel and perpendicular to the direction towards the convergent point (blue arrow). Also shown are the observed components of the proper motion in l and b direction (dashed red lines). The dashed black lines indicate the projection of the observed proper motion components in l and b direction on the direction towards the convergent point.

the convergent point and perpendicular (μ_{\perp}) to this direction can be determined. Comparison of the observed and rotated proper motion with the calculated velocity component from the cluster centre of mass in direction to the convergent point yields the secular parallax ϖ through:

$$\varpi = \varkappa \frac{\mu_{||}}{v_{||}} \quad (4.9)$$

where \varkappa is once again the conversion factor from $1 \text{ mas}\cdot\text{yr}^{-1}$ at 1 kpc to $1 \text{ km}\cdot\text{s}^{-1}$, $\mu_{||}$ the observed proper motion in direction towards the convergent point and $v_{||}$ is the velocity component of the cluster's space velocity at the considered point on the sky in direction towards the convergent point (compare Röser et al. [2011, eq. 2]). Then the parallax directly leads to the distance of a star through the formula:

$$d [\text{pc}] = \frac{1}{\varpi[\text{arcsec}]} = \frac{v_{||}}{\varkappa \cdot \mu_{||}} \cdot 1000 \quad (4.10)$$

Here the factor 1000 is needed because the distance is given in kpc when it is calculated from the proper motions given in mas/yr with the conversion factor \varkappa .

5. NBODY6TID

This chapter presents the program **NBODY6TID**. It will discuss the principles used to derive numerical solutions to the N -body problem and will explain the procedure to scale the star cluster to N -body units. In addition the parameters needed to start a simulation will be introduced and the backwards integration in time to derive the initial position of the Hyades will be exposed. In a final step the initial position and velocity of the Hyades will be calculated.

The program **NBODY6TID** is a direct N -body code, developed in the stellar dynamics group at ARI by Ernst, Just and Spurzem and based on the code **NBODY6** by Aarseth [2003]. It solves the N -body problem in an analytical background potential (for more details see Ernst [2012]). In contrast to **NBODY6** the program **NBODY6TID** includes the implementation of the Galactic tidal field derived from different approximation for the Galactic background potential. Some available models are:

- three component Plummer-Kuzmin model (Miyamoto & Nagai [1975])
- power law models
- Dehnen models (Dehnen [1993] and Tremaine et al. [1994])
- and Plummer model (Plummer [1911])

The program also provides evolutionary data for all stars in the simulation and is available in three different variants:

- **NBODY6TID**, the standard serial code for runs on single CPU systems
- **NBODY6TIDPAR**, the code for runs on parallel machines (based on **NBODY6++** by Spurzem [1999])

- NBODY6TIDGPU, a code version for runs on multicore processors with one or two GPUs (Nitadori & Aarseth [2012])

For this work the standard code variant NBODY6TID was used with a three-component-Plummer-Kuzmin model of the Milky Way as background potential (Miyamoto & Nagai [1975]), whose parameters are shown in Table 5.1. For the solution of the N -body problem a calculation of the acceleration and higher derivatives of it for any star in the simulation is required. Since the acting forces in the simulation are due to gravitational self-attraction of the N stars and the employed background potential, the equation of motion for gravitation has to be solved. This requires computing times proportional to N^2 . For every particle i the acceleration reads:

$$\ddot{\mathbf{r}}_i = -\nabla\Phi(\mathbf{r})|_{\mathbf{r}_i} - G \sum_{j=1; j \neq i}^N \frac{m_j(\mathbf{r}_i - \mathbf{r}_j)}{|\mathbf{r}_i - \mathbf{r}_j|^3} \quad (5.1)$$

(Aarseth [2003, p. 6])

Given the initial values for mass, position and velocity $m_i, \mathbf{r}_i, \mathbf{v}_i$ for every star i in the simulation at some time t_0 the set of $3N$ second-order differential equation defines the solution for the position $r_i(t)$ for every time t . In order to get numerical solutions for the position one starts to calculate the acceleration for the time t_0 and then calculates the new positions and velocities for the time $t_1 = t_0 + \Delta t$ for a small time step Δt .

$$\begin{aligned} \mathbf{v}_i(t) &= \ddot{\mathbf{r}}_i \Delta t + \mathbf{v}_i(t_0) \\ \mathbf{r}_i(t) &= \frac{1}{2} \ddot{\mathbf{r}}_i \Delta t^2 + \mathbf{v}_i(t_0) \Delta t + \mathbf{r}_i(t_0) \end{aligned} \quad (5.2)$$

(see Aarseth [2003, p. 14])

Since this simple approximation leads to considerable errors after a short time, a fourth order Hermite scheme is used in NBODY6TID. This scheme uses Taylor expansions up to the fourth order as well as the jerk, the time derivative of the acceleration. For detailed information about the Hermite scheme see Aarseth [2003] and Ernst [2012]. Hence the computing time depends highly on the size of the time step Δt and the particle number N . For small time steps Δt and large particle numbers N the computing time increases enormously. But since the number of particles in one simulation is high and a good accuracy of the integration needs small time steps, one requires a solution to

Table 5.1.: Galaxy parameters for the 3PLK Milky Way model

Components	$M [M_{\text{sun}}]$	$a [\text{kpc}]$	$b [\text{kpc}]$
Bulge	$1.4 \cdot 10^{10}$	0.0	0.3
Disk	$9.0 \cdot 10^{10}$	3.3	0.3
Halo	$7.0 \cdot 10^{11}$	0.0	25.0

give acceptable computing times. In the N -body code this is done by two algorithms. One for adjusting the time steps for close encounters, and one to reduce the actual number of stars for calculating the acting gravitational force.

5.1. Individual and block time steps

Star cluster systems involve many processes acting over different time scales, from the short time scales of close orbiting binaries (some days) up to the relaxation time of the whole star cluster. The forces caused by the slower evolving subsystems have minimal impact on the acting forces on the faster evolving system. So, in order to get a minimal computing time, the slower evolving subsystems are evaluated with different time-steps than the fast evolving system. For example, the fast evolving system is evaluated at every time-step Δt_i while the slow evolving subsystem is evaluated at every fourth time-step, while for the other time steps its evolution is interpolated.

For the force calculation of close encounters of two bodies there is even another algorithm called KS-regularization. This involves replacing a close binary by its centre of mass in the main simulation and just calculating the forces for the centre of mass without resolving the two stars while the exact orbit of the binary is calculated by switching to another coordinate system making calculations easier (for more details see Aarseth [2003]; Khalisi & Spurzem [2006])

5.2. Ahmad-Cohen scheme

This algorithm was first suggested by Ahmad & Cohen [1973]. As stated above, the full force calculation for every star i makes the simulation very time consuming. Since the forces acting on a star i generated by very distant stars are small due to the inverse

square law of gravitation one can split the forces into two parts using a neighbor scheme.

$$\mathbf{a}_i = \mathbf{a}_{i,irr} + \mathbf{a}_{i,reg} \quad (5.3)$$

The first term $\mathbf{a}_{i,irr}$ is called irregular force term and is the force generated by stars within a certain radius around the considered star i . This force underlies a more frequent change due to the proximity of these stars and therefore is calculated more often than the second part. The second term $\mathbf{a}_{i,reg}$ is called regular force term and is generated by the stars more distant from the considered star i . These stars do not change their relative distance as quickly as close stars and hence the force created by them has not to be calculated as often as the irregular term. The result is, that by selecting a subset of neighbors for every particle i the full summation over N particles in Equation 5.1 reduces to a summation over N_{nb} neighbor particles and so the computation time reduces (compare Aarseth [2003, p. 32ff] and Khalisi & Spurzem [2006]).

5.3. Nbody-units

The program NBODY6TID uses special N -body-units, which are obtained by setting the gravitational constant G and the initial cluster mass M and the virial radius r_{vir} equal to 1. With the formula for the virial radius

$$r_{vir} = \frac{GM^2}{4|E|} \quad (5.4)$$

a total energy E equal to -0.25 is calculated. These definitions of gravitational constant, mass and virial radius also determine the unit of velocity and time. With the typical velocity for stars in a cluster:

$$v_{NB} = \sqrt{\frac{GM}{r_{vir}}} \quad (5.5)$$

the unit of velocity has the value $v_{NB} = 1$. And by assuming r_{vir} as a typical length one unit of time gets:

$$\tau_{NB} = \frac{r_{vir}}{v_{NB}} = \sqrt{\frac{r_{vir}^3}{GM}} = \frac{GM^{5/2}}{(4|E|)^{3/2}} = 1 \quad (5.6)$$

In the last step the formula for the virial radius and the velocity were plugged in. With the formula for the crossing time inside a star cluster:

$$t_{cr} = \frac{GM^{5/2}}{(2|E|)^{3/2}} \quad (5.7)$$

the crossing time in N -body-units is simply given by: $t_{cr} = 2\sqrt{2}\tau_{NB}$ (c.f. Khalisi & Spurzem [2006]).

In physical units it is convenient to express the length scales \bar{R} in pc, the stellar mass \bar{M} in M_\odot , the time scale \bar{T} in Myr and the velocity in \bar{V} in $\text{km}\cdot\text{s}^{-1}$. Then the conversion from N -body units to physical units is simply done by

$$\begin{aligned} r_{ph} [\text{pc}] &= \bar{R} \cdot r [\text{NBU}] \\ m_{ph} [M_\odot] &= \bar{M} \cdot m [\text{NBU}] \\ t_{ph} [\text{Myr}] &= \bar{T} \cdot t [\text{NBU}] \\ v_{ph} [\text{km}\cdot\text{s}^{-1}] &= \bar{V} \cdot v [\text{NBU}] \end{aligned} \quad (5.8)$$

where NBU stands for one N -body unit of the considered scale. The conversion factor \bar{R} for the length scale and \bar{M} for the mass directly arises from the definition of one N -body unit of length and mass. So that $\bar{R} = r_{vir}$ and $\bar{M} = M_{cl} = Nm_{mean}$, where m_{mean} is the mean mass of a star in the star cluster. The conversion factor for the time unit is obtained by taking the second part of Equation 5.6 and plugging in the numbers to express r_{vir} in [pc], M in [M_\odot] and the value of $G = 4.48 \cdot 10^{-3} \text{ pc}^3 \cdot M_\odot^{-1} \cdot \text{Myr}^{-2}$. This yields a numerical factor of 14.94 and converting to the cluster parameters for length \bar{R} and mass \bar{M} gives

$$\bar{T} = 14.94 \cdot \sqrt{\frac{\bar{R}^3}{\bar{M}}} \quad (5.9)$$

The conversion factor for the velocity is obtained in the same way by using Equation 5.5 and plugging in physical units for G , M and r_{vir} and converting to cluster scales so that one gets:

$$\bar{V} = 6.71 \cdot 10^{-2} \cdot \sqrt{\frac{\bar{M}}{\bar{R}}} \quad (5.10)$$

(cf. Aarseth [2003]).

5.4. Input files

The simulation program **NBODY6TID** requires two files with input parameters. One is used for the description of the galaxy and its tidal field, and is called *galax.dat*. The other is used for the parameters of the star cluster and is called *inmodel*. Once the parameters for the host galaxy of the star cluster are chosen the file *galax.dat* can be generated and used for every star cluster model in this particular galaxy. The parameters in *galax.dat* are given in physical units and scaled to N -body units in the program after specifying the scaling parameters. In contrast the file *inmodel* has to be adjusted for every new star cluster simulation.

5.4.1. Input file: *galax.dat*

The file *galax.dat* takes 28 different parameters to characterise the host galaxy. Among them are the galactic centre position and velocity as well as the type of the galaxy model and its mass. Further parameters relate to dynamical friction and treatment of cluster mass (constant or evolving) or the accuracy of galactic center integration (Ernst [2012, p. 13]). As a galaxy model for the simulations in this work a three component Plummer-Kuzmin-model (3PLK) (Miyamoto & Nagai [1975]) with parameters given in Table 5.1 was chosen. The galactic centre position and velocity for the starting point of the simulation were determined by a backwards integration (see section 5.5) of the present-day position and velocity of the Hyades barycentre. The calculated values for the cluster position and velocity 625 Myr ago can be found in Equation 5.14..

5.4.2. Input file: *inmodel*

The file *inmodel* takes 95 parameters for the modeling of the star cluster. The most important are: the total number of stars, a random number seed, the scaling factors for conversion from N -body units to physical units for the mass and the size of the cluster, a time termination parameter, a parameter for choosing a star cluster model and its initial mass distribution. A description of all other parameters can be found in Khalisi & Spurzem [2006]. For the simulations done in this work most parameters were chosen the same as for the work in Ernst et al. [2011]. Just the shape of the IMF for the initialization of stellar masses and the ratio of initial $R_{Jac}/R_{99\%}$ was changed. And this

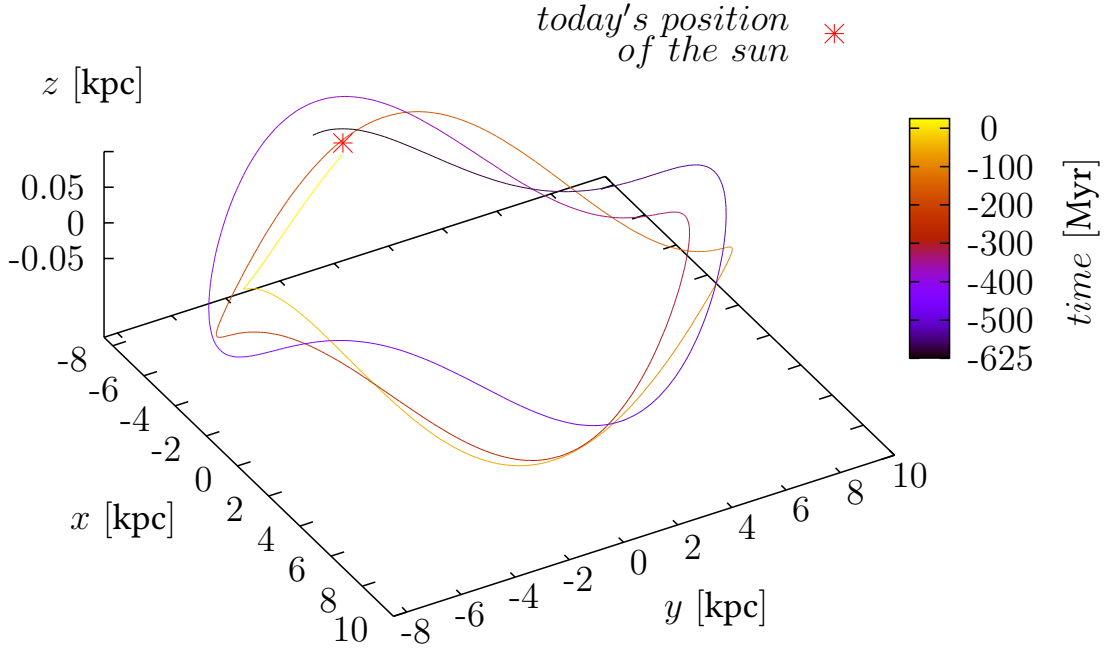


Fig. 5.1.: Three dimensional orbit of the Hyades as result of the integration in the three-component-Plummer-Kuzmin model of the Milky Way. The time 0 Myr corresponds to the present time while -625 Myr corresponds to the time when the Hyades originated. The red star shows the today's position of the sun.

involves a change of particle number and scaling factor for mass and length. Detailed prescription of the procedure of changing this values can be found in section 7.1.

5.5. Path integration

For the simulation of the Hyades evolution over the past 625 Myr one needs the initial conditions for the Hyades barycentre at the start time of the simulation. To obtain the position and velocity for the Hyades barycentre 625 Myr ago the centre of mass orbit was integrated backwards in time in the analytical background potential of the Milky Way starting with the present-day position and velocity of the Hyades. The resulting orbit around the Galactic centre is shown in Figure 5.1. The Hyades completed nearly 3 full orbits in its lifetime up to now. The direction of rotation is clockwise around

the Galactic centre seen from the Galactic north pole. In the Galactic plane the orbit is slightly eccentric with radii between 7.087 kpc and 8.638 kpc. In z -direction the Hyades show an oscillation up to a height of 74 pc either side of the Galactic disk (Ernst et al. [2011]). The backwards integration is calculated in galactocentric coordinates. For the present-day position of the Hyades in galactocentric coordinates the values of Ernst et al. [2011] were taken:

$$\begin{aligned}x_0 &= -44.26 \text{ pc} - 8000 \text{ pc} \\y_0 &= 0.31 \text{ pc} \\z_0 &= -16.89 \text{ pc} + 20 \text{ pc}\end{aligned}\tag{5.11}$$

where the first terms in Equation 5.11 relate to the Hyades barycentre with respect to the position of the sun (8 kpc from the Galactic centre). The second terms are the result of the translation of the point of origin from the sun to the Galactic centre. For the position of the sun in the Milky Way the values of Piskunov et al. [2006] were used. The present-day velocity of the Hyades with respect to the sun is given by:

$$\begin{aligned}v_{x,0} &= -41.18 \text{ km}\cdot\text{s}^{-1} \\v_{y,0} &= -19.04 \text{ km}\cdot\text{s}^{-1} \\v_{z,0} &= -1.27 \text{ km}\cdot\text{s}^{-1}\end{aligned}\tag{5.12}$$

To convert this into galactocentric velocities the velocity of the peculiar motion of the sun with respect to the local standard of rest (LSR) and the orbital velocity of the LSR have to be taken into account. For the velocity of the Hyades centre of mass with respect to the Galactic centre follows:

$$\begin{aligned}v_{x,0} &= -41.18 \text{ km}\cdot\text{s}^{-1} + 11.10 \text{ km}\cdot\text{s}^{-1} \\v_{y,0} &= -19.04 \text{ km}\cdot\text{s}^{-1} + 12.24 \text{ km}\cdot\text{s}^{-1} + 234.20 \text{ km}\cdot\text{s}^{-1} \\v_{z,0} &= -1.27 \text{ km}\cdot\text{s}^{-1} + 7.25 \text{ km}\cdot\text{s}^{-1}\end{aligned}\tag{5.13}$$

The first terms in Equation 5.13 are the velocities of the Hyades centre of mass with respect to the sun, the second terms correspond to the sun's peculiar motion with respect to the LSR (Schönrich et al. [2010]) and the third term corresponds to the orbital

velocity of the LSR around the Galactic centre at 8 kpc.

For a backwards integration in time the integrator takes the galactocentric position and the negative galactocentric velocity (because its going backwards in time) of the Hyades barycentre. The result of the integration leads to the position and the velocity of the Hyades barycentre 625 Myr ago. To obtain the right velocity the sign of the velocity has to change once again to give an orbit forward in time. The resulting position and (forward in time) velocity of the Hyades are:

$$\begin{aligned} x_{-625} &= -7212.38 \text{ pc} & v_{x,-625} &= -78.06 \text{ km}\cdot\text{s}^{-1} \\ y_{-625} &= -1566.08 \text{ pc} & v_{y,-625} &= 236.68 \text{ km}\cdot\text{s}^{-1} \\ z_{-625} &= 66.63 \text{ pc} & v_{z,-625} &= -1.03 \text{ km}\cdot\text{s}^{-1} \end{aligned} \quad (5.14)$$

Since `NBODY6TID` works in a coordinate system with origin in the cluster barycentre one has to convert the given position and velocity of the Hyades barycentre into coordinates and velocities for the galactic centre with respect to the cluster centre. Therefore the signs of the position and the velocity changes again when creating the input file of `NBODY6TID`.

5.6. Star cluster initialization

For the initialization of the star cluster masses, positions and velocities for each star have to be calculated consistent with the chosen star cluster model. For this work a King model with King-parameter $W_0 = 6$ was used. Positions and velocities were calculated by an external program called *rotinit*. The program randomly assigns positions and velocities to the stars under the constraint that the conditions of the King model are fulfilled. The program takes as parameters a random number seed and the number of stars of the star cluster. The masses of the stars are calculated by `NBODY6TID` itself using a routine by Kroupa and Weidner (see within Ernst et al. [2011]). They are drawn randomly from a specified initial mass function (IMF). For this work a three-part broken power law IMF giving the number of stars for logarithmic mass intervals was used. The IMF was adapted by the author while a project lab from new observational data of the Hyades provided by Goldman et al. [in press]. The IMF for the three different mass

intervals reads:

$$\frac{dN}{d\log m} = \begin{cases} c_1 m^{+2.0}, & 0.08 \leq m [\text{M}_\odot] < 0.18 \\ c_2 m^{0.0}, & 0.18 \leq m [\text{M}_\odot] < 1.00 \\ c_3 m^{-3.3}, & 1.00 \leq m [\text{M}_\odot] < 100 \end{cases} \quad (5.15)$$

The constants c_1 to c_3 are determined by normalization and the requirement of a smooth transition between the mass regimes. In the simulation the lowest and the highest mass were forced to take the value $m_{low} = 0.08 \text{ M}_\odot$ and $m_{high} = 100 \text{ M}_\odot$.

6. *Observations*

This chapter deals with the observational data used for this thesis. It will present the principle of choice used to determine Hyades member candidates as well as the observed properties studied in this work.

The observational data used for this work is a new data set of 774 Hyades stars provided by Goldman et al. [in press] containing Hyades stars down to masses as low as $0.09 M_{\odot}$. This data set contains, among other information, the mass, the position, luminosity and the proper motion of the Hyades stars. With the convergent point method information about the velocity perpendicular and parallel to the convergent point, the radial velocity as well as parallax values were calculated. The basis for this data file was a data set provided by Röser et al. [2011] using the PPMXL (Roeser et al. [2010]) and CMC14 (Copenhagen University et al. [2006]) catalogues. The new reduction by Goldman et al. [in press] with the Pan-STARRS1 (Panoramic Survey Telescope And Rapid Response System) catalogue complements the data set by Röser et al. [2011] down to $0.09 M_{\odot}$. Both reductions use a three step membership selection process for the Hyades stars. Initially, member candidates are selected by the convergent point method (section 4.2) predicting also radial velocities. Then the created sample will be restricted by a photometric membership selection, and in the last step the proper motions given by Pan-STARRS1 will be verified by cross-checking with PPMXL entries extrapolated to the epoch of observation by Pan-STARRS1. Thus the proper motions are verified or further candidates will be rejected. In this process of membership determination a small fraction of non-member stars remain in the sample of member stars. According to Goldman et al. [in press] the contamination with field stars in the pure sample is <10% for distances to the cluster centre smaller than 18 pc. In the outer shell from 18 pc to 30 pc the contamination rises to 17%. Goldman et al. [in press] expect almost all contaminants to be dwarfs (92%), with few giants (8%).

6. Observations

Table 6.1.: Parameters of the Hyades determined from the observations. The numbers in parentheses refer to the clean sample with $|v_{\perp}| \leq 2 \text{ km}\cdot\text{s}^{-1}$

Quantity	Value
Lowest mass m_l	$0.09 M_{\odot}$
Highest mass m_h	$2.6 M_{\odot}$
Maximum radius r_{max}	30 pc
Number of stars $N(r_{max})$	773 (668)
Total mass $M(r_{max})$	$477.8 M_{\odot}$ ($424.71 M_{\odot}$)
Jacobi radius r_J	8.4 pc (8.2 pc)
Number of stars $N(r_J)$	363 (334)
Total mass $M(r_J)$	$270.7 M_{\odot}$ ($252.8 M_{\odot}$)
Core radius r_c	3 pc
Number of stars $N(r_c)$	100 (91)
Total mass $M(r_c)$	$102.8 M_{\odot}$ ($95.5 M_{\odot}$)
Completeness limit	$0.1 M_{\odot}$

6.1. Membership determination

6.1.1. Kinematic selection of candidates

For the kinematic selection of Hyades member stars the convergent point method (section 4.2) with the constraint that cluster membership is given if the difference between cluster velocity \mathbf{v}_c and velocity of the candidate \mathbf{v} is smaller than some limiting boundary ϵ

$$|\mathbf{v}_c - \mathbf{v}| \leq \epsilon \quad (6.1)$$

(c.f. Röser et al. [2011, eq. (1)]) is used. Since the radial velocity is not observed but fixed by this method to be the same as the projection of the cluster centre of mass velocity onto the line of sight and the velocity parallel to the direction towards the convergent point is fixed to be the same as that calculated from the cluster centre of mass velocity for the position of the star on the sky, Equation 6.1 reduces to:

$$|v_{\perp}| \leq \epsilon \quad (6.2)$$

(Röser et al. [2011, eq. (2)]) Furthermore the expectation value of v_{\perp} is zero and hence $\langle v_{\perp}^2 \rangle^{1/2}$ is an estimate for the one-dimensional velocity dispersion in the cluster.

In the work of Goldman et al. [in press] the limiting boundary ϵ was chosen to be $4 \text{ km}\cdot\text{s}^{-1}$; additionally the angle between the direction towards the convergent point and the proper motion vector was limited to a maximum value of 9.5° . To guarantee a more pure sample, the candidates chosen in Goldman et al. [in press] can be further restricted to have a perpendicular velocity $|v_\perp| \leq 2 \text{ km}\cdot\text{s}^{-1}$. According to Goldman et al. [in press] this reduces the field contamination by a factor of two while a value of $2 \text{ km}\cdot\text{s}^{-1}$ is still much larger than the internal velocity dispersion of the cluster (compare subsection 7.5.1). This selection of Hyades probable members is not a final confirmation since radial velocity and kinematic parallax and thereby distances are predicted. These quantities can be confirmed by using the kinematic parallax to construct the color-magnitude diagram, and to check if the positions of the candidate stars in this diagram are valid or not.

6.1.2. Photometric membership determination

With photometric membership determination, the color-absolute-magnitude diagrams for the candidates, which have passed the kinematic selection, are created. In these diagrams true Hyades member stars should lie on a narrow sequence, while field stars should form a cloud below this sequence. Field stars lie below the Hyades sequence because of the proximity of the Hyades to the Sun while field stars are farther away from the sun than the Hyades. As stated in Goldman et al. [in press] available theoretical isochrones do not fit the Hyades sequence. Thus the Hyades sequence in the color-absolute-magnitude-diagrams is modeled with a second order polynomial to set the photometric criteria for membership.

The reason why the field stars do not share the Hyades sequence is that the absolute magnitude calculated by the kinematic parallax, and determined on the basis of the convergent point method, is too small. Hence the stars are fainter than stars at the distance of the Hyades should be. Therefore the calculated secular parallax for the field stars could not be true. They have to be farther away from the Sun and thus lie behind the Hyades such that their proper motion fits that of Hyades stars just by chance.

6.2. Observational quantities

From the observational data file, different distinctive quantities such as the mass function, the cumulative mass profile, the density profile, the average cumulative mass function, the shape of the cluster and its velocity dispersion were determined. The same quantities were determined for the simulations and compared to that of the observations.

6.2.1. Cumulative mass profile

Another way to compare the observational properties of the Hyades with the simulation is the cumulative mass profile. This is the mass of the star cluster as a function of the radius. To get the mass of the star cluster as a function of the radius, all the masses of the stars within a given radius from the cluster centre are summed up. This is done for several values of the radius from the cluster centre. The resulting curve is shown in Figure 7.3. In the inner part up to the Jacobi radius, the increase of the mass cumulative mass function corresponds well to a isothermal density profile with $\varrho \propto r^{-2}$, while in the outer part the stars are ripped away by the tidal forces of the Galaxy so that the trend of the mass function is declining. One way to quantify the agreement of observed and simulated cumulative mass profile is with the Kolmogorov-Smirnov-test (compare Smirnov [1948, 1939]). This test is also used to determine the agreement of the cumulative mass profiles for different initial values of ξ with the observations and to find the best fitting model among them.

6.2.2. Kolmogorov-Smirnov-test

The Kolmogorov-Smirnov-test is a statistical test to analyse whether two random variables follow the same empirical distribution function or not, and was suggested by Smirnov [1939]. For the test procedure the vertical difference d_i between two normalized cumulative functions is calculated for all data points within the sample and the supremum d_{max} is selected. For the cumulative mass profile of observation and

Table 6.2.: Values of D_α for different statistical significances α

Level of significance	D_α
20%	1.07
10%	1.22
5%	1.36
2%	1.52
1%	1.63
0.01%	2.23

simulation this means:

$$d_i(r_i) = \left| \frac{M_{obs}(r_i)}{M_{obs}(r_{max})} - \frac{M_{sim}(r_i)}{M_{sim}(r_{max})} \right|$$

$$d_{max} = \sup_{r_i} d(r_i)$$
(6.3)

In this equation $M_{obs}(r_i)$ refers to the value of the cumulative mass profile of the observation at the radius r_i , $M_{obs}(r_{max})$ to the total mass within a given maximal radius r_{max} and $M_{sim}(r_i)$ and $M_{sim}(r_{max})$ to the same quantities of the simulation. The index i refers to the i^{th} data point in the sample. The higher the value d_{max} the worse the accordance of the two cumulative mass profiles. By rescaling the calculated value of d_{max} to the number n, m of data points in the samples one can also give an estimate of the statistical significance of the agreement. The rescaled value of d_{max} is calculated as follows:

$$\hat{d} = d_{max} \sqrt{\frac{nm}{n+m}}$$
(6.4)

where n is the number of data points in the simulation and m the one in the observations. If the value of \hat{d} is higher than a given value D_α the agreement of the two cumulative mass profiles can be rejected with a statistical significance α . The value of D_α for different statistical significances α is given in Table 6.2.

6.2.3. Mass function

The first characteristic quantity for comparing observations and simulations is the present-day mass function, the number of stars within a certain mass range. For the

6. Observations

Hyades the mass function is calculated in logarithmic mass bins of 0.1 dex size. It starts with a lower mass limit of $0.08 M_{\odot}$ and ends at a high mass limit of about $2.5 M_{\odot}$. The present-day mass function is calculated for 3 radii regimes of 3 pc (the core), 9 pc (Jacobi radius) and 30 pc from the cluster centre. In a log-log-diagram the shape of the mass function follows a three-component broken power law similar to the initial mass function. The comparison of the present-day mass function of observation for the whole sample and for the clean sample (just those stars with $v_{\perp} < 2 \text{ km}\cdot\text{s}^{-1}$) as well as the ensemble 2750W6 is shown in Figure 7.5.

6.2.4. Mass segregation

The equipartition of kinetic energy due to two body relaxation leads to a slow down of massive stars and a speed up of low mass stars. Therefore the low mass stars can reach higher orbits in the star cluster while the massive stars sink down into lower orbits deeper in the cluster centre. Thus this phenomenon leads to a separation of the stars by mass, called mass segregation. The mass segregation can be seen by plotting the mean stellar mass as a function of radius from the cluster centre. Another way to quantify the mass segregation in a star cluster is the minimum spanning tree method (Olczak et al. [2011]). The minimum spanning tree is the sum over all connection lines of a graph connecting all vertices within a given sample of stars with the lowest possible sum of edges and no closed loops. Thus the length of this graph is a measure of compactness of a sample of stars in the star cluster. An algorithm for the derivation of the spanning tree is given in Gower & Ross [1969]. An improved method for the minimum spanning tree Γ_{MST} is given in Olczak et al. [2011]. With this method one can obtain information about the compactness of samples of objects but not about their actual position in the star cluster. However, since the average cumulative mass indicates a mass segregation towards the centre of the star cluster, this method can quantify the indicated mass segregation. As a measure of mass segregation Olczak

et al. [2011] define the dimensionless value Γ_{MST} :

$$\begin{aligned}\Gamma_{MST} &= \frac{\gamma_{MST}^{ref}}{\gamma_{MST}^m} \\ \gamma_{MST} &= \left(\prod_{i=1}^n e_i \right)^{1/n} = \exp \left(\frac{1}{n} \sum_{i=1}^n \ln(e_i) \right)\end{aligned}\quad (6.5)$$

where e_i is length of the i^{th} edge of the spanning tree. The superscript *ref* refers to a random sample of $n + 1$ stars out of the entire population while the superscript *m* refers to a sample of the $n + 1$ most massive stars.

No mass segregation leads to a value of $\Gamma_{MST} = 1$, while a mass segregated cluster should hold a value of $\Gamma_{MST} > 1$. The higher the value of n of the sample of considered stars, the lower the value of Γ_{MST} so that if n is equal to the whole sample of stars one obtains $\Gamma_{MST} = 1$.

6.2.5. Velocity dispersion

The velocity dispersion in one dimension k for data with N stars in the sample can be calculated according to Equation 3.27 by:

$$\sigma_k^2 = \frac{1}{N-1} \sum_{i=1}^N (v_i - \bar{v})^2 \quad (6.6)$$

where v_i is the velocity of the i^{th} star and \bar{v} is the mean velocity of the sample. For the observations this result must be corrected for the measurement errors to obtain the real velocity dispersion. The corrected velocity dispersion can be written as:

$$\sigma_{k,corr}^2 = \sigma_k^2 - \frac{1}{N} \sum_{i=1}^N \epsilon_i^2 \quad (6.7)$$

In this equation ϵ_i is the measurement error of the velocity of the i^{th} star. The mean errors of the velocity dispersion are then computed as:

$$\Delta\sigma_k = \frac{1}{\sqrt{2N}} \sigma_k + \Delta\epsilon_i \quad (6.8)$$

6. Observations

where $\Delta\epsilon_i$ is the uncertainty of the velocity error determination dependent on the way the velocity and its error are determined (compare van Altena [2013, p. 365]). Since there is no information for this value the error component was not calculated and the uncertainty of the velocity dispersion was taken to be:

$$\Delta\sigma_k = \frac{1}{\sqrt{2N}}\sigma_k \quad (6.9)$$

which is just the randomnoise due to the finite sample of stars in the determination of the velocity dispersion. Given that the convergent point method predicts that the velocity dispersion perpendicular to the direction towards the convergent point to be a measure for the one dimensional velocity dispersion, this value was calculated for the observations and compared to the value obtained from the simulations.

7. *Simulation results*

This chapter discusses the results of the simulations undertaken in this work. It will present the topics of interest, the parameters used to start the simulations and the calculated outputs as well as the evaluated results. First the mass function, the cumulative mass profile, the density profile and the mass segregation of the ensemble 2750W6 will be explained and the effect of N -body noise on this quantities will be examined. Afterwards the effect of different initial ratios of Jacobi radius and 99% mass radius on the evolution of the cumulative mass profile and the mass segregation of star cluster will be studied. At last a detailed analysis of the velocity dispersion and the effect of the convergent point method on the distance determination of the stars in the Hyades will be undertaken.

7.1. *Calculation of the scaling factor \bar{R}*

To set up the simulations for the Hyades the parameters for scaling the cluster to N -body units were calculated according to section 5.3. The initialization with a special value for $R_{Jac}/R_{99\%}$ was done by adjusting the value \bar{R} . With the value R_K for the King radius in N -body units taken from Gürkan et al. [2004, Table 1] and the numerical calculated value for the ratio $R_{99\%}/R_K$, taken from a set of data provided by Andreas Ernst (priv. com.), the value for $R_{99\%}$ in N -body units was calculated as follows:

$$R_{99\%} \text{ [NBU]} = \frac{R_{99\%}}{R_K} R_K \text{ [NBU]} \quad (7.1)$$

The mass M_{cl} of the star cluster was then calculated from the mean stellar mass \bar{m} determined by the IMF and the number of stars N in the simulation. From this the Jacobi radius R_{Jac} was determined by Equation 3.8. With the scaling formula from

7. Simulation results

Table 7.1.: Parameters for the determination of the scaling factor \bar{R}

Quantity	Value
King radius R_k	0.32 [NBU]
ratio $R_{99\%}/R_K$	11.82
99% mass radius $R_{99\%}$	3.7824 [NBU]
Mean stellar mass \bar{m}	$0.619 M_\odot$
circular velocity V_{Cir} at 8 kpc	234.2154 km·s ⁻¹
$\beta = \kappa/\Omega$ at 8 kpc	1.3664

Equation 5.8 for the length scale, this can be expressed in N -body units:

$$R_{Jac} [\text{NBU}] = \frac{R_{Jac} [\text{pc}]}{\bar{R}} \quad (7.2)$$

And it follows, given the ratio for $\xi = R_{Jac}/R_{99\%}$, that the scaling factor \bar{R} reads as:

$$\bar{R} = \frac{R_{Jac} [\text{pc}]}{\xi \cdot R_{99\%} [\text{NBU}]} \quad (7.3)$$

The values for the calculation of the scaling factor \bar{R} are given in Table 7.1.

7.2. Data processing

The output file of NBODY6TID contains for every N -body time step information about the position, velocity, mass and evolutionary state (after a classification from Hurley et al. [2000]) of every star. Since only main sequence stars are intended to be compared to observational data, stars which are non main sequence stars should be removed from the simulated data. These are mainly black holes, neutron stars and white dwarfs. Black holes and neutron stars originate from the most massive stars at the beginning of the simulation. White dwarfs however originate from lower massive stars which original mass is too low to form a black hole or neutron star. In any case, the majority of the stars stay unevolved, since an evolutionary time of 625 Myr is too short for the evolution of most main sequence stars in the simulation. For example Padova isochrones yield about $2.6 M_\odot$ for the mass of a star to leave the main sequence in a time scale of 625 Myr.

Table 7.2.: Initial parameters of the ensemble 2750W6

Quantity	Value
King Parameter W_0	6
Particle number N_0	2750
Mean stellar mass \bar{m}	$0.619 M_{\odot}$
Total mass M_0 calculated	$1702.25 M_{\odot}$
Total mass M_0 from IMF	$(1688.9 \pm 25.3) M_{\odot}$
Jacobi radius r_J	$(16.12 \pm 0.01) \text{ pc}$
99% mass radius $R_{99\%}$	$(36.84 \pm 1.09) \text{ pc}$
ratio $R_{Jac}/R_{99\%}$	0.44 ± 0.01

Therefore all stars below this mass limit stay essentially unevolved over the whole simulation.

A further correction has to be applied to the density centre of the star cluster. At the beginning the density centre lies at the origin but with dynamical evolution the density centre changes. The corrected position of the density centre is calculated with the method from Casertano & Hut [1985] and the position of every star is subsequently corrected such that the density centre corresponds to the origin.

7.3. Ensemble 2750W6

In the first part of this work the effect of different random initializations of one model was investigated. For the Hyades, an improved model of the best fitting model of Ernst et al. [2011] was adopted. The model was improved by the author during a project lab. The main parameters of one ensemble averaging ten runs of this model are shown in Table 7.2. A detailed comparison of the numbers of stars and the masses within different radii from the cluster centre can be found in Table A.1 in the Appendix. Furthermore a list with the number of White dwarfs within the cluster can be found in Table A.2 in the Appendix. A detailed analysis of the effect of the random initialization on

- the mass function
- the cumulative mass profile
- the present day mass function

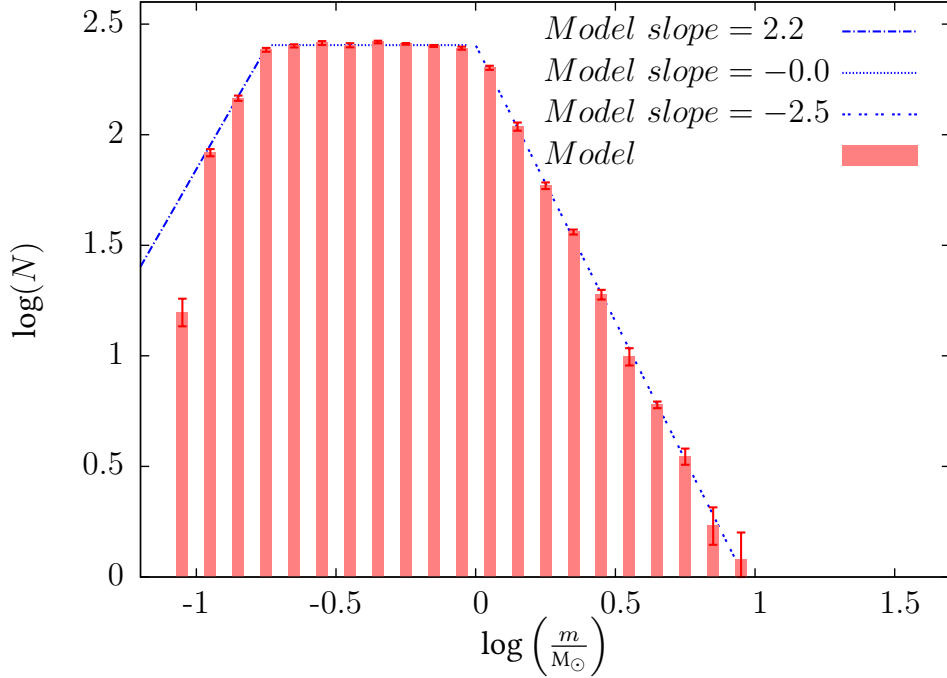


Fig. 7.1.: Average realization of the three-part broken power law initial mass function of ensemble 2750W6. The diagram shows the mean value of the logarithm of the number of stars $\log(N)$ with a mass within a certain mass bin of width 0.1 dex calculated from the ensemble, averaging over ten runs. The error bars show the 1σ standard error. The initial particle number of the ensemble 2750W6 is 2750 stars. The analytical slopes of the broken power law are plotted in blue dashed lines with different line styles for the different parts. The long-dashed blue line shows the first part in the lower mass regime, the dotted blue line shows the intermediated flat part and the short-dashed blue line shows the decreasing part in the high-mass regime.

- the density profile
- and the mass segregation

was undertaken, and detailed below.

7.3.1. Initial mass function and stellar evolution

The initial mass function (IMF) used to calculate the mass of the stars in the simulation is in a log-log diagram a three-part broken power law. The slopes of the used power law are given in Equation 5.15. For the mass interval from $0.08 M_\odot$ to $0.18 M_\odot$ the slope is

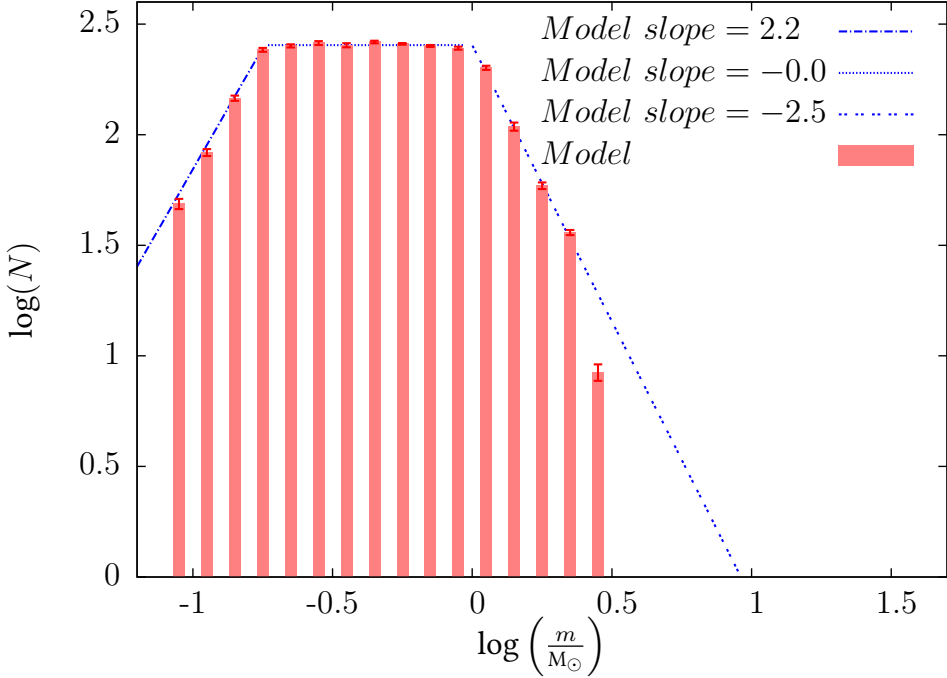


Fig. 7.2.: Average realization of the three-part broken power law mass function of ensemble 2750W6 after 625 Myr of evolution. The diagram shows the mean value of the logarithm of the number of stars $\log(N)$ with a mass within a certain mass bin of width 0.1 dex calculated from the ensemble, averaging over ten runs. The error bars show the 1σ standard error. The analytical slopes of the broken power law initial mass function are plotted in blue dashed lines with different line styles for the different parts. The long-dashed blue line shows the first part in the lower mass regime, the dotted blue line shows the intermediated flat part and the short-dashed blue line shows the decreasing part in the high-mass regime.

2.2, for the intermediate-mass interval from $0.18 M_\odot$ to $1 M_\odot$ the mass function is flat with a slope of 0, and in the high-mass regime from $1 M_\odot$ to the highest mass (taken to be $100 M_\odot$) the IMF is decreasing with a slope of -2.5 . The average realization of this IMF in the ensemble 2750W6 is shown in Figure 7.1. The error bars are 1σ standard error bars calculated from the ensemble, averaging over ten runs, with each an initial number of 2750 stars. The theoretical trend of the three-part power law is plotted in blue lines with different line styles for the different components. The long-dashed blue line shows the first part in the lower mass regime, the dotted blue line shows the intermediate flat part and the short-dashed blue line shows the decreasing part in the

high-mass regime. The same plot of the mean value of the logarithm of the number of stars $\log(N)$ with a mass within a certain mass bin of width 0.1 dex calculated from the ensemble, averaging over ten runs, was created for the end of the simulation after 625 Myr of evolution to see the effect of stellar evolution. The result is shown in Figure 7.2. In this plot, as well as in the following diagrams, only main sequence stars are shown. For illustration the analytical trends of the initial mass function as well were plotted in dashed blue lines in this diagram. Only the high-mass stars, greater than $2.5 M_{\odot}$, have disappeared due to stellar evolution. The rest of the stars stayed relatively unchanged in their evolution over the time scale of 625 Myr.

7.3.2. Cumulative mass profile

Figure 7.3 shows the effect of the random initialization on the cumulative mass profile. All ten models were initialized by the same number of stars, the same IMF and the same ratio of $R_{Jac}/R_{99\%}$, but with different random number seeds for the distribution of positions, velocities and masses of the stars. Figure 7.3 shows the observational data (black lines), the ensemble average cumulative mass profile (thick red line) and its standard deviation (red area) as well as the best-fitting run (green dotted line) and a curve calculated from Equation 3.8 showing the mass within a given Jacobi radius (blue dotted line). The crossing point of this line with the one for the cumulative mass profile gives the Jacobi radius of the system. Except for the inner most part ($r < 2.5$ pc) of the star cluster the relative dispersion of the models is about $1/4$. Within the Jacobi radius the mean value lies well above the observed curve. However the best-fitting model describes the observed data within the Jacobi radius very well. But the high dispersion has to be kept in mind while analyzing just one model run. The agreement of the cumulative mass profiles was quantified by a Kolmogorov-Smirnov-test for the inner 9 pc region. The value for \hat{d} for the average of the cumulative mass profiles is about 2.46. The highest value of a single run was determined to be 2.35. This may be a hint that simple ensemble averaging is distorting the shape of the cumulative mass profile and hence not a right approach. However the value for the best-fitting model (green curve) was calculated to 1.05 while the lowest value obtained for one cumulative mass profile within the ensemble was 0.72. But by looking at the cumulative mass profile of this run and comparing it to the observational data one can find that it does

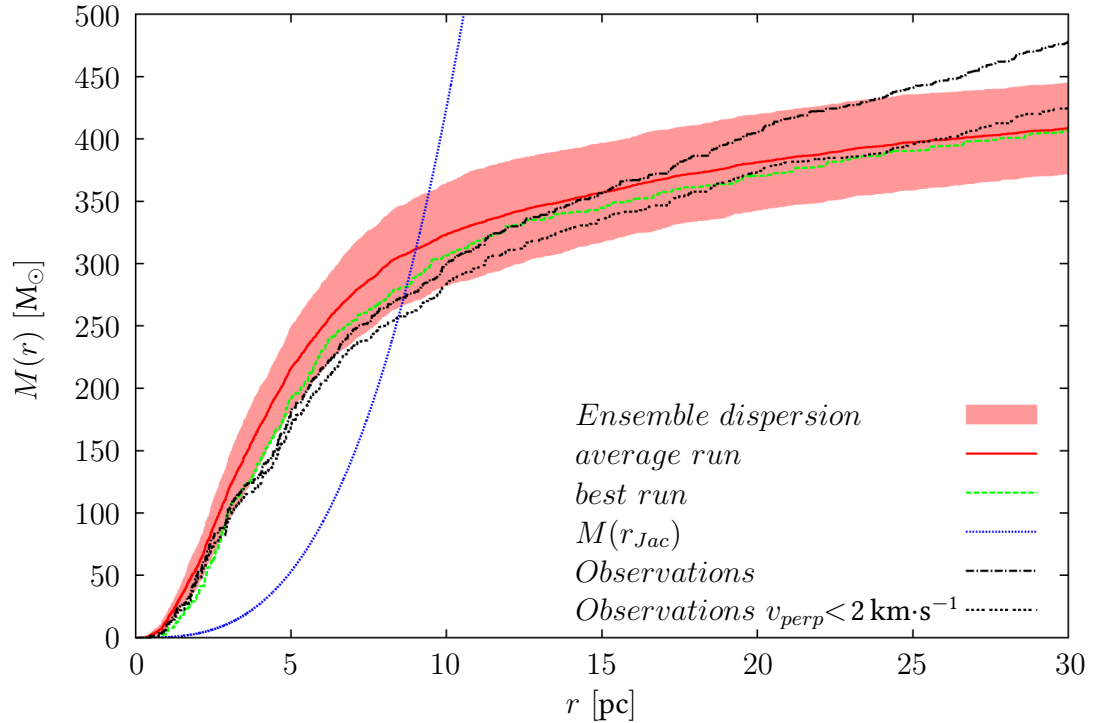


Fig. 7.3.: Present-day cumulative mass profile of observation and ensemble. The black long-dashed line shows the observational data for all stars. The short-dashed black line shows the observational data those stars which have a perpendicular velocity smaller than $2 \text{ km}\cdot\text{s}^{-1}$. The red solid line represents the average cumulative mass profile of the ten runs, the light red area shows the standard deviation of the ensemble. The blue dashed line shows the mass within a given Jacobi radius calculated with Equation 3.8. The green dashed line shows the best-fitting model run.

not really fit better the observational data than a mass profile with higher value for \hat{d} . Its curve runs nearly parallel to the observed curve and contains more mass within the Jacobi radius than the observational data (see Figure 7.4). Therefore finally the decision for the best-fitting model of the ensemble 2750W6 was done by eye and by quantifying the result through the Kolmogorov-Smirnov-test. For detailed discussion of the effect that in special cases the Kolmogorov-Smirnov-test may be useless see section A.2 in the Appendix. The parameters of the best fitting model are also shown in Table A.4 in the Appendix.

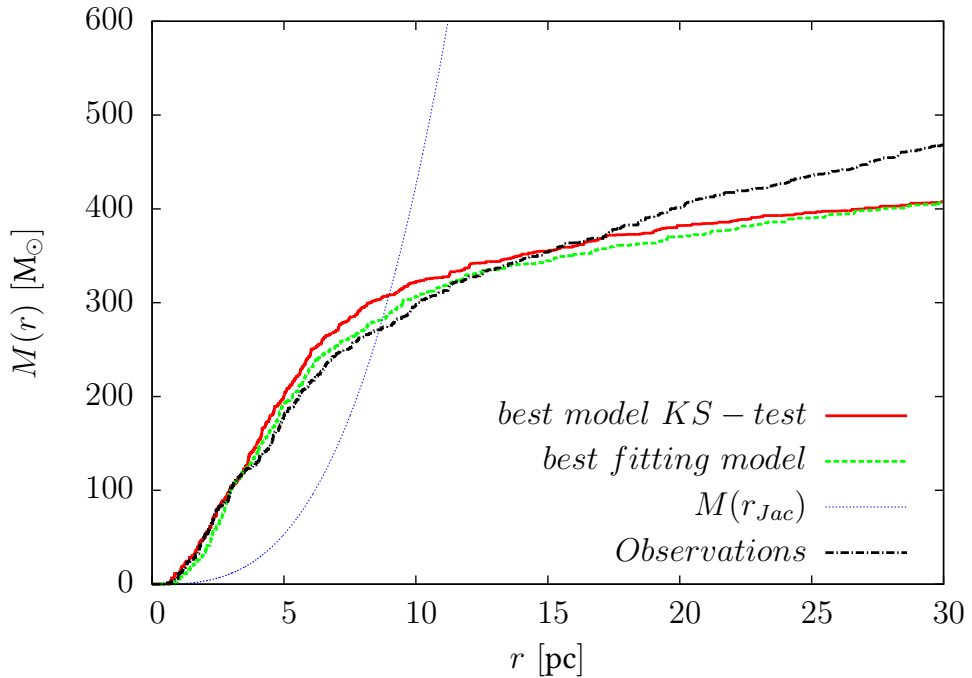


Fig. 7.4.: Best-fitting model according to the Kolmogorov-Smirnov-test. *The red line* shows the best fitting model according to the Kolmogorov-Smirnov-test, *the green line* shows the chosen best-fitting model and *the black line* shows the observational data (here the whole sample of stars is used). *The blue line* as before shows the mass within the Jacobi radius as a function of radius.

7.3.3. Present-day mass function

Figure 7.5 represents the comparison of the present-day mass function (PDMF) between observations and simulations for stars within 3 pc (*top panel*), 9 pc (*middle panel*) and 30 pc (*bottom panel*) from the cluster centre. The diagram shows the logarithm of the average value of the number of stars within a certain mass bin of width 0.1 dex. The simulated results are shown in red bars where a sample of $N = 588 \pm 43$ stars within a radius of 30 pc was used. The error bars show the 1σ standard error calculated from the ensemble of ten runs. For the whole observational data (dark blue bars) a sample of $N = 773$ stars within a radius of 30 pc was used. And the clean observational data (light blue), of stars with a velocity perpendicular to the line of sight with $v_{perp} < 2 \text{ km}\cdot\text{s}^{-1}$, leaving a sample of $N = 668$ stars to calculate the PDMF (see also Table A.1).

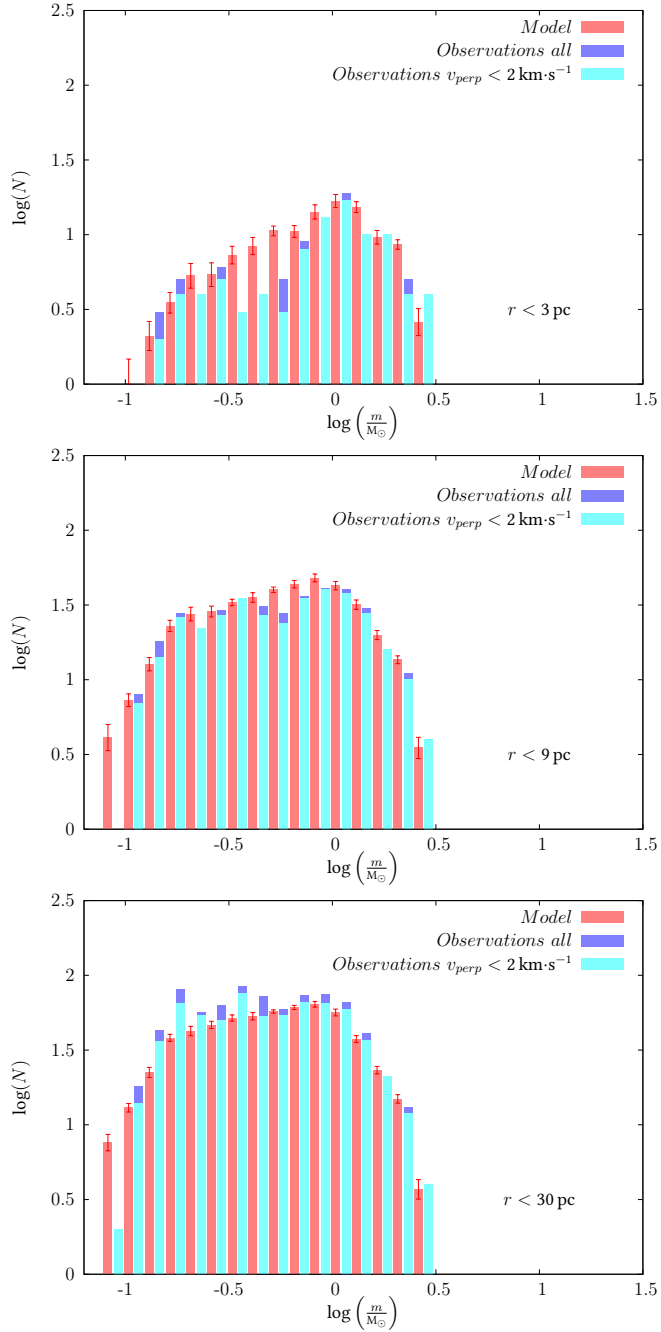


Fig. 7.5.: Comparison of the PDMFs of observations and ensemble 2750W6 for stars within 3 pc, 9 pc and 30 pc from the cluster centre. *Top panel:* stars within a radius of 3 pc (core), *middle panel:* stars within a radius of 9 pc (Jacobi radius) and *bottom panel* stars within a radius of 30 pc from the centre. Shown are for the simulation in red bars the mean values of $\log(N)$ calculated from the ensemble, averaging over ten runs. The error bars show the 1σ standard error. The dark blue bars show the values for all stars in the observational data while the light blue bars show the values for just those stars with $v_{\text{perp}} < 2 \text{ km}\cdot\text{s}^{-1}$.

The ensemble 2750W6 fits the observational data very well although there is a difference of 78 stars between the total number of stars within 30 pc in the clean sample of observations and the simulations. Hence the number of stars in the observation and simulation do not agree within the uncertainty range of the the number of stars in the simulation. However, the overall shape of the mass function is reproduced for all three radii regimes. The observational data shows a nearly bimodal behavior for the core. There is a lack of stars with a mass from $0.4 M_{\odot}$ to $0.6 M_{\odot}$ which does not occur in the simulation. This could be due to unresolved binaries in the core region, or as Ernst et al. [2011] stated, this is at the same position as the Wielen dip, related to the mass-luminosity relation. For the whole radius region of 30 pc there is a slight overabundance of stars with a mass of $\sim 0.2 M_{\odot}$ to $0.5 M_{\odot}$ in the observations. This could be due to contamination with field stars in the outer part. Another interesting result is that nearly all massive stars with masses higher than about $1.5 M_{\odot}$ are located in the core. This can be seen by comparing the mass function for the innermost 3 pc with that one of the total radius regime of 30 pc. All stars with a mass higher than $1.5 M_{\odot}$ within 30 pc can already be found within 3 pc. This can also be seen in Figure A.2 in the Appendix where the spatial extend of the observed cluster is compared to the simulated one.

7.3.4. Density profile

The density profile of both simulation and observations are shown in Figure 7.6. The observed density profile is plotted in blue, the simulated density profile is shown in red. Both profiles have a flat core and then decrease towards the outer parts of the star cluster. In the outermost parts ($r > 10$ pc), beyond the Jacobi radius, the star density becomes increasingly small ($\rho < 0.01 M_{\odot} \cdot pc^{-3}$) and hence the noise is very high. Within the Jacobi radius the observed density is well characterized by the simulation. It lies in between the dispersion of the ten runs. In the outer part, beyond the Jacobi radius, the simulated density is to low to fit the observed values. One reason for this is the contamination with field stars in the observation within this region. In the log-log diagram the total spread of the simulated density is, apart from the region beyond the Jacobi radius, nearly constant with a value of about 0.4 dex.

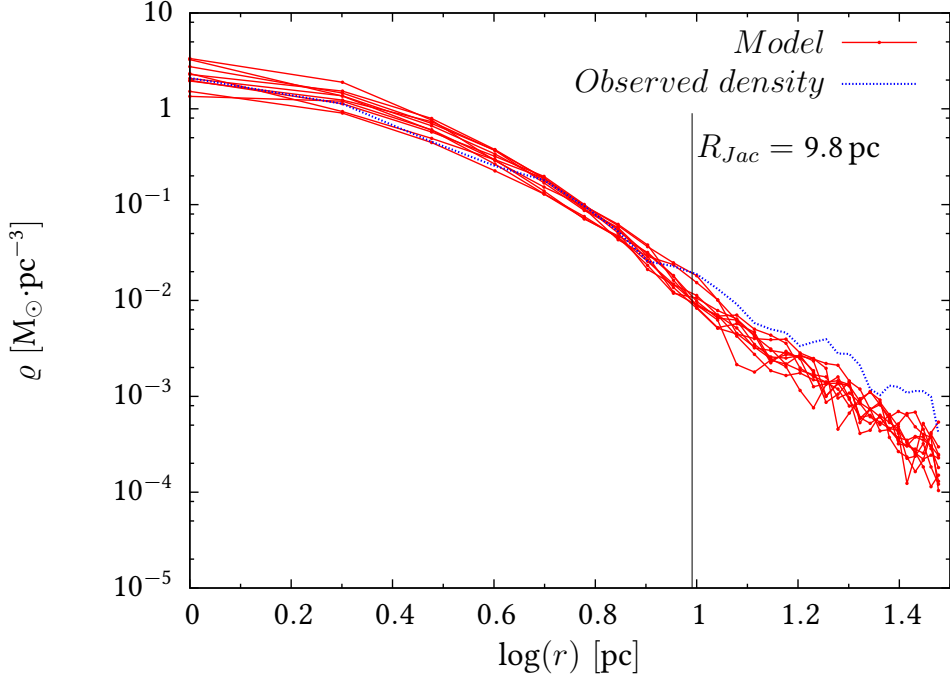


Fig. 7.6.: Density profile of simulation and observation. *The red lines* show the ten model runs of the ensemble 2750W6, *the blue line* shows the observed density profile. The Jacobi radius of the ensemble 2750W6 of (9.8 ± 0.3) pc is marked with a vertical black line.

7.3.5. Mass segregation

To investigate the mass segregation, the mean stellar mass for the observations and for the beginning of the simulations (625 Myr ago) and the end of the simulations (present-day) was calculated. The average cumulative mass is calculated by summing up all the masses of the stars within a given sphere around the centre of the star cluster. Then the cumulative mass is divided by the number of stars within this volume. This leads to a value for the mean mass of a star in the considered volume. By increasing the sphere around the cluster centre one can obtain a value for the average cumulative mass of a star as a function of the radius. The top panel of Figure 7.7 shows the average cumulative mass at the beginning of the simulation and the bottom panel of Figure 7.7 shows the average cumulative mass of simulation and observation at present-day. The result for the observations and the simulation for the present-day is an increasing average cumulative mass in the core of the star cluster. At the tidal radius of 9 pc the average cumulative mass of a star is about $0.75 M_{\odot}$. In the core this value is about

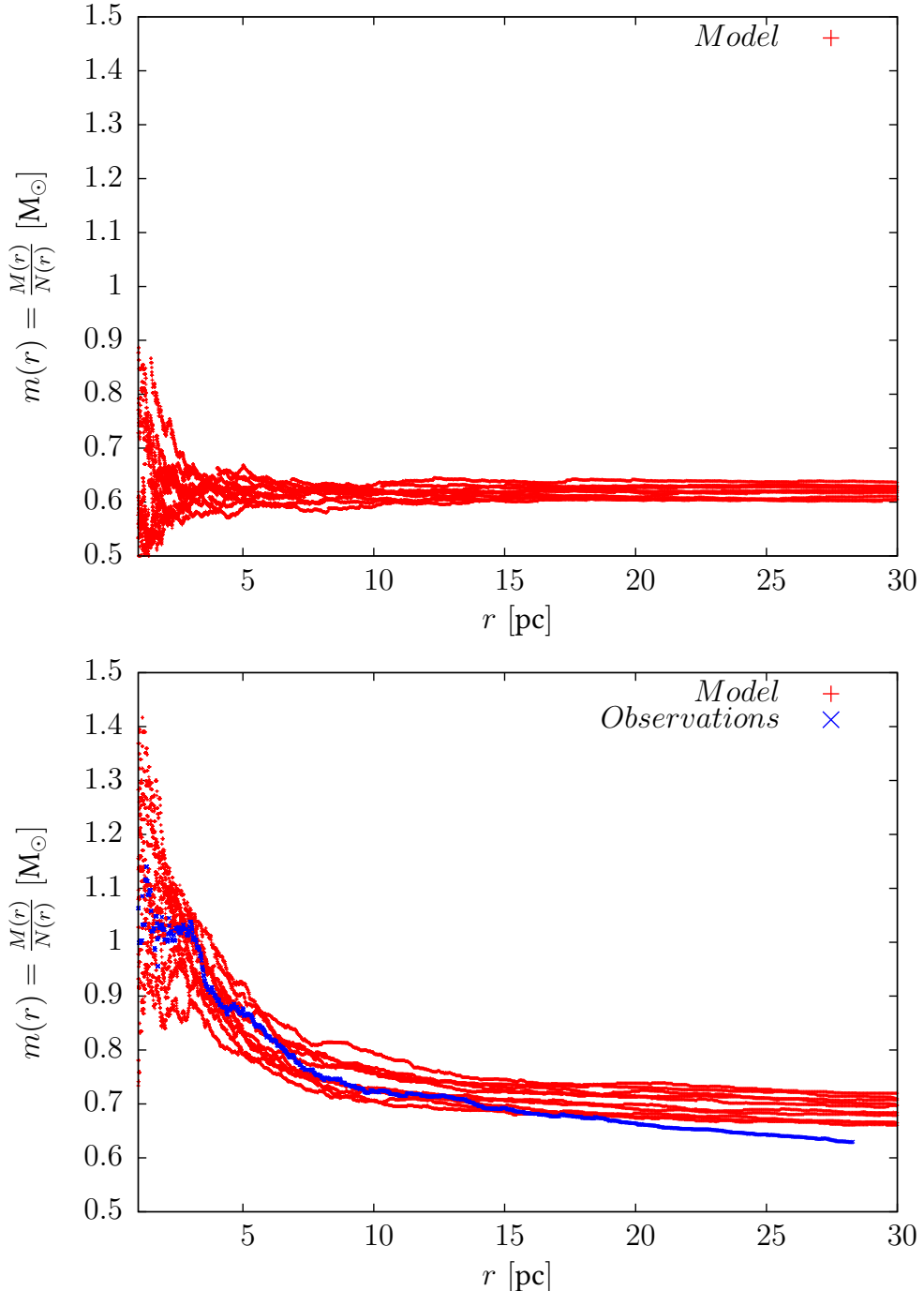


Fig. 7.7.: Average cumulative mass for observations and simulations. *The top panel* shows the average cumulative mass for all model runs of the ensemble 2750W6 at the beginning of the simulation (625 Myr ago). *The bottom panel* shows the present-day average cumulative mass profile of observations (blue) and simulations (red) after 625 Myr of evolution. The higher mean mass in the cluster centre is an unmistakeable sign for mass segregation.

7.4. Evolutionary effect of initial ratio of Jacobi radius to 99% mass radius

Table 7.3.: Parameters of initial ratio of $R_{50\%}/R_{Jac}$ and final ratio of $R_{50\%}/R_{Jac}$ for different initial ratios of $\xi = R_{Jac}/R_{99\%}$

$\frac{R_{Jac}}{R_{99}}$	M [M $_{\odot}$]	$\frac{R_{50\%}}{R_{Jac}}$	$\frac{R_{50\%}}{R_{Jac}}$ (initial)
3	724	0.321 ± 0.006	0.06 ± 0.02
2	643	0.315 ± 0.040	0.106 ± 0.001
1	728	0.305 ± 0.003	0.209 ± 0.003
$\frac{2}{3}$	848	0.300 ± 0.027	0.299 ± 0.004
$\frac{1}{2}$	1009	0.353 ± 0.059	0.347 ± 0.006
$\frac{2}{5}$	1702	0.429 ± 0.025	0.410 ± 0.009

1.15 M $_{\odot}$. This is an unmistakeable sign for mass segregation in the cluster because this shows that on average the masses of the stars in the cluster center are higher than in the outer parts. At the beginning of the simulation the average cumulative mass is nearly the same over the whole volume of the star cluster (apart from some dispersion in the core). Its value is as expected the mean stellar mass of ~ 0.62 M $_{\odot}$, calculated from the IMF. Thus the more massive stars are sinking towards the cluster centre while low mass stars must be kicked out of the star cluster such that at present-day the mean stellar mass within 30 pc is larger than the initial mean stellar mass of ~ 0.62 M $_{\odot}$ (compare also subsection 6.2.4). A further investigation of the mass segregation for the best fitting model of ensemble 2750W6 was done by calculating the velocity dispersion for different mass bins. This showed as expected a smaller velocity dispersion for the high mass stars (see Table A.3 in the Appendix). To show the dispersion in the average cumulative mass profile due to the random initialization all ten runs were plotted in the diagrams in Figure 7.7.

7.4. Evolutionary effect of initial ratio of Jacobi radius to 99% mass radius

The second part of this work contains an analysis of the effect of initial ratio $\xi = R_{Jac}/R_{99\%}$ on the evolution of the star cluster. The higher the value for ξ , the denser the star cluster. The lower the value for ξ the less closely spaced are the stars in the cluster. A study of the effect of this initial property was done by adjusting the

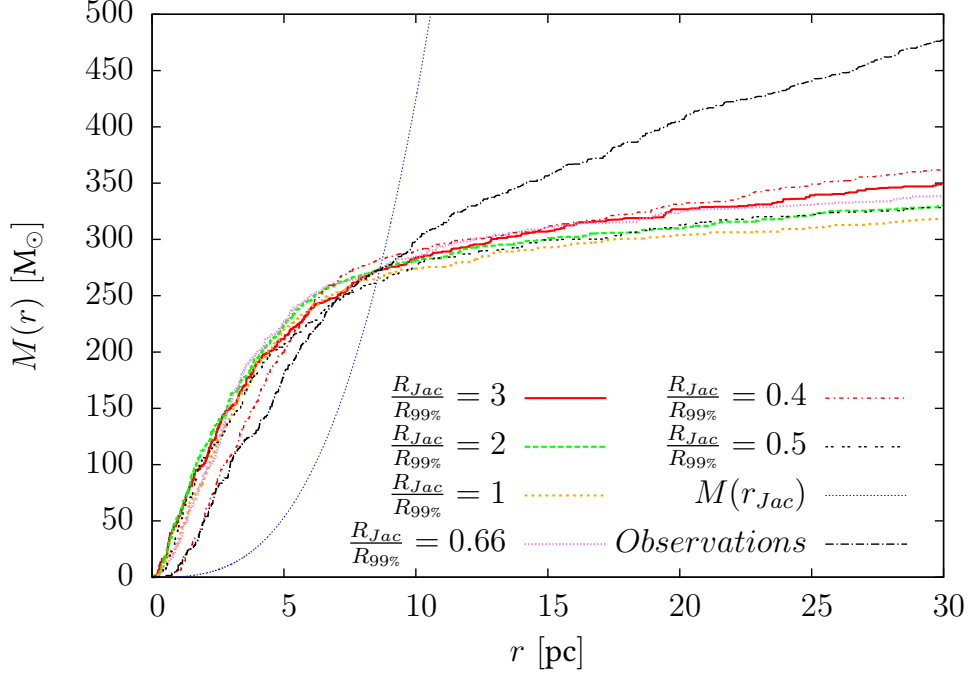


Fig. 7.8.: Cumulative mass profiles for different initial values $\xi = R_{Jac}/R_{99\%}$. The black line shows the observations, the blue line shows the mass within a given Jacobi radius.

simulations such that at the end of a simulation the Jacobi radius of the different models was nearly the same. Simulations were run for five different initial ratios of $\xi = R_{Jac}/R_{99\%}$, each with three runs to get some statistic about the dispersion of the models. Ratios of $\xi = 3, 2, 1, 0.5$ and 0.4 were chosen. The cumulative mass profile was investigated for the value of final ratio of $R_{50\%}/R_{Jac}$ of the half-mass radius to the Jacobi radius. Furthermore the effect on the mass segregation was tested, using the average cumulative mass profile and the minimum spanning tree method of Olczak et al. [2011].

7.4.1. Mass profile - final ratio of half-mass radius to Jacobi radius

To quantitatively study the effect of the initial ratio $\xi = R_{Jac}/R_{99\%}$ on the mass profile, the value for the final ratio of half-mass radius $R_{50\%}$ to Jacobi radius R_{Jac} , $R_{50\%}/R_{Jac}$, was calculated. The half-mass radius $R_{50\%}$ was just calculated from the mass within the Jacobi radius and not from the whole mass within 30 pc. The ratio $R_{50\%}/R_{Jac}$ gives,

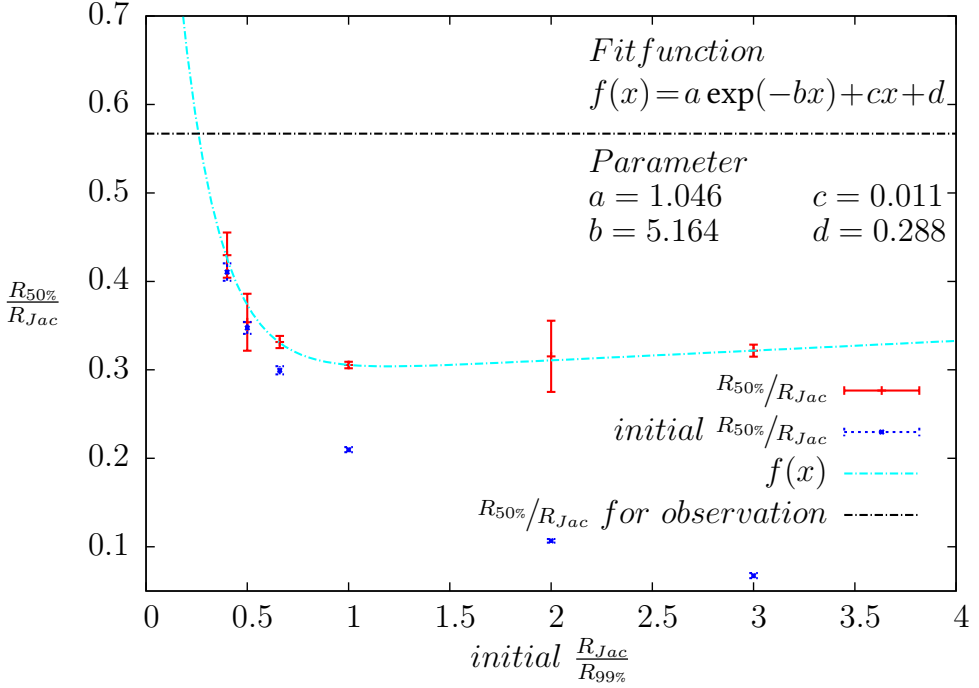


Fig. 7.9.: Final ratio of $R_{50\%}/R_{Jac}$ as a function of initial ratios of $\xi = R_{Jac}/R_{99\%}$. The red points show the final value of $R_{50\%}/R_{Jac}$, the light blue line shows a least square fit of the function $f(x) = a \exp(-bx) + cx + d$ to the simulated data. The parameters of the fit are shown in the top right corner of the plot. The dark blue points show the initial ratio of $R_{50\%}/R_{Jac}$ for the different initial ratios of $\xi = R_{Jac}/R_{99\%}$. The black dotted line shows the observed ratio of $R_{50\%}/R_{Jac} = 0.57$.

similarly to the initial ratio $R_{Jac}/R_{99\%}$, a measure for the mass distribution as a function of the radius from the cluster center. The Jacobi radius is calculated by the program NBODY6TID and the half-mass radius is calculated by summing up the masses of the stars beginning from the cluster centre up to half the mass within the Jacobi radius is met. The distance of the last added star from the cluster centre is then the half mass radius. To guarantee that the different models are self-consistent, and that they represent the Hyades, the models were adjusted such that in the end of the simulation (after 625 Myr of evolution) all have nearly the same mass within the Jacobi radius, namely the same mass as the Hyades. Figure 7.8 shows the resulting cumulative mass profiles of one run for the different models. The values for the initial ratio of $R_{50\%}/R_{Jac}$ and final ratio of $R_{50\%}/R_{Jac}$ for different initial ratios of $\xi = R_{Jac}/R_{99\%}$ can be found in Table 7.3. Figure 7.9 shows a plot of the final ratio of $R_{50\%}/R_{Jac}$ as a function of initial

7. Simulation results

ratios of $\xi = R_{Jac}/R_{99\%}$. The red points show the final value of $R_{50\%}/R_{Jac}$ at the end of the simulation. The blue points show the initial ratio of $R_{50\%}/R_{Jac}$ for the different initial ratios of ξ . For small values of ξ , and hence for a less dense star cluster, there is nearly no change in the ratio of $R_{50\%}/R_{Jac}$ for the initial and the final values. But for large values of ξ , the ratio of $R_{50\%}/R_{Jac}$ changes from about 0.1 at the beginning of the simulation to 0.33 at the end of the simulation. Thus, regardless of the initial density of a star cluster, it converges on a final ratio of half mass radius to Jacobi radius of $R_{50\%}/R_{Jac} \sim 0.33$.

In Figure 7.9 the light blue line shows a least square fit of the function $f(x) = a \exp(-bx) + cx + d$ to the simulated data. The parameters of the fit are shown in the top right corner of the plot. The black dotted line shows the observed ratio of $R_{50\%}/R_{Jac}$. The crossing point of the black and the light blue line is at about $\xi = 0.3$. This suggests that the Hyades started their evolution with an initial value of $\xi = 0.3$, which corresponds well to the value of ξ for the Pleiades derived by Schlüter [2012]. In fact this value of an overfilling initial star cluster can be estimated from the star formation efficiency and the formula for the tidal radius under the assumption that the composition of cluster and gas formed a nearly Roche lobe filling formation. Given that the star-formation efficiency is:

$$SFE = \frac{M_{cl}(t)}{M_{gas,i} + M_{gas,acc}(t)} \approx \frac{M_{cl}}{M_{gas,i}} \quad (7.4)$$

where $M_{cl}(t)$ is the cluster mass as a function of time, $M_{gas,i} = M_{gas+cl}$ the initial gas mass and $M_{gas,acc}(t)$ the accreted gas mass (Dib et al. [2013]). For simplicity this was taken to be zero and the cluster mass was taken to be independent of time (e.g. the cluster mass shortly before gas expulsion). With the assumption that the initial 99% mass radius of the cluster is more or less the same as the Jacobi radius of the cluster gas formation, it follows:

$$\frac{R_{Jac,cl}}{R_{99\%}} \approx \frac{R_{Jac,cl}}{R_{Jac,gas+cl}} = \left(\frac{M_{cl}}{M_{gas,i}} \right)^{1/3} = (SFE)^{1/3} \quad (7.5)$$

With values of 1% to 60% for the star formation efficiency SFE (Dib et al. [2013]) the ratio of initial Jacobi radius to 99% mass radius can be estimated between 0.2 and 0.8. This should be the value to start the simulations since gas expulsion is not considered

7.4. Evolutionary effect of initial ratio of Jacobi radius to 99% mass radius

Table 7.4.: Values for \hat{d} for the Kolmogorov-Smirnov-test for models with different values of ξ . The three values for the three different runs of the individual values of ξ give an overview over the dispersion due to the random initialization of the single models.

ξ	\hat{d}		
$^{2/5}$	1.50	1.32	1.09
$^{1/2}$	2.92	2.76	1.62
$^{2/3}$	3.10	2.46	2.26
1	2.94	2.93	2.69
2	3.20	3.28	2.21
3	2.91	2.98	2.73

in the simulation, due to its instantaneous occurrence (Baumgardt & Kroupa [2007]). The gas expulsion time scale ($\sim 10^5$ Myr) is much shorter than the initial crossing time ($\sim 10^6$ Myr) of the cluster. Thus the theory of star cluster formation provides an explanation to the overfilled initial cluster, or to put the other way around, the initial conditions of cluster formation determine the star-formation efficiency of the primordial molecular cloud.

7.4.2. Agreement of observation and simulation for different ratios of Jacobi radius to 99% mass radius

To quantify the agreement of the cumulative mass profile of the models for different values of ξ with the observed cumulative mass profile, a Kolmogorov-Smirnov-test was applied. A comparison of the values for \hat{d} is shown in Table 7.4. The model with the best agreement to the observational data is the one with a value of $\xi = 2/5$ and a value of $\hat{d} = 1.09$ to 1.50. This corresponds to a significance level of 5%. All other values for \hat{d} are higher than 2.21 (besides one for $\xi = 1/2$) and therefore their cumulative mass profile is with a chance of 99.99% due to a distribution function different from that of the observation. This supports the assumption made from Figure 7.9 that the Hyades formed with an initial value of $\xi = 2/5$ or smaller.

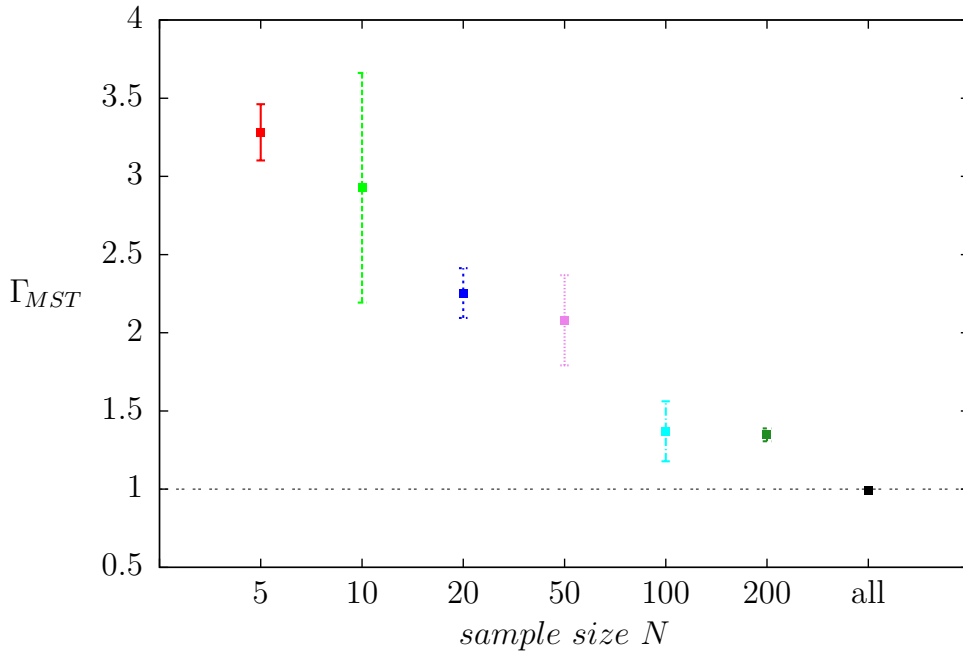


Fig. 7.10.: Mass segregation for a simulation with initial ratio $R_{Jac}/R_{99\%} = 1$. Shown are from left to right the cumulative values for Γ_{MST} for the 5 (red), 10 (light green), 20 (blue), 50 (purple), 100 (light blue) and 200 (dark green) most massive stars as well as all stars (black). A value of $\Gamma_{MST} = 1$ marks an unsegregated star cluster.

7.4.3. Mass segregation: Minimum spanning tree

Figure 7.10 shows the values of Γ_{MST} for a model of the Hyades with initial ratio of $R_{Jac}/R_{99\%} = 1$ for the 5, 10, 20, 50, 100, 200 and all most massive stars within a radius of 30 pc around the cluster centre. Note that the higher the sample size of massive stars, the lower the value of Γ_{MST} (see subsection 6.2.4). This analysis show that the stars up to the 50 most massive stars are highly segregated compared to an equal-sized random sample of stars. Together with the analysis of the average cumulative mass (Figure 7.7) this is a clear indication that the most massive stars are located in the centre of the star cluster.

The five different models for ξ were similarly tested for their degree of mass segregation in terms of the effect of the initial ratio $R_{Jac}/R_{99\%}$ on the mass segregation. The result of this analysis is shown in Figure 7.11 where the value of Γ_{MST} for the 10 (light green), 20 (blue), 100 (light blue) and all (black) most massive stars was plotted

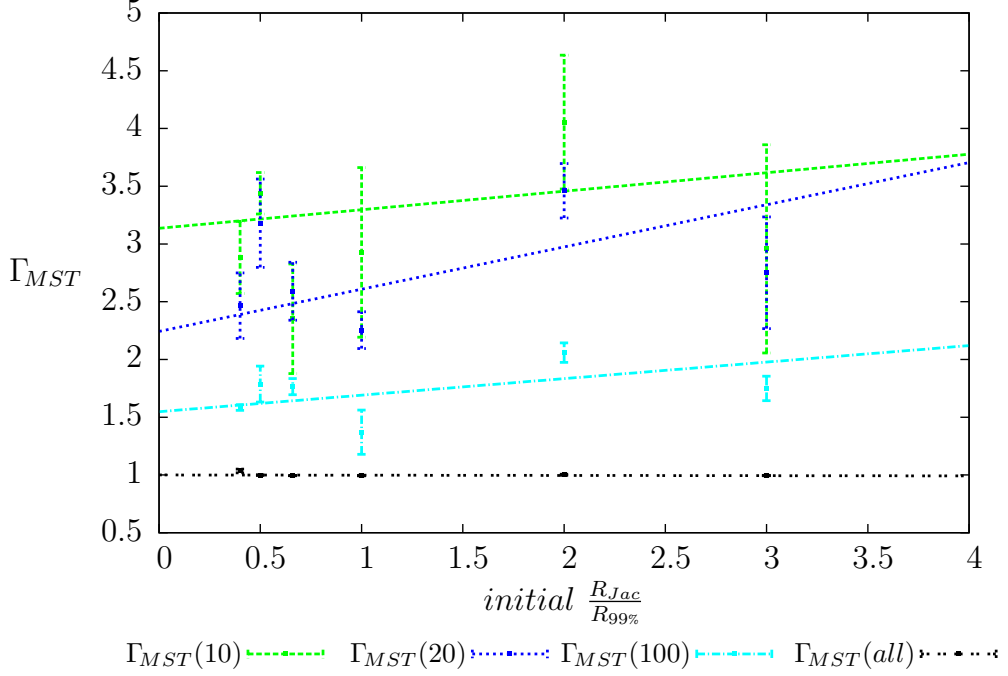


Fig. 7.11.: Comparison of mass segregation for simulations with initial ratios of $R_{Jac}/R_{99\%} = 0.4, 0.5, 1, 2$ and 3 (from left to right). Shown are values for Γ_{MST} for the 10 (green), 20 (blue), 100 (light blue) and all (black) most massive stars. To show the trend in the mass segregation with increasing value of $R_{Jac}/R_{99\%}$ a linear least square fit to the data is plotted as dashed lines.

as a function of initial ratio $R_{Jac}/R_{99\%}$ of the models. As expected, for all models the value of Γ_{MST} for all most massive stars is equal to 1, and the lower the sample size the higher the value of Γ_{MST} becomes. In order to show the trend in the dependency of the degree of mass segregation on the initial ratio of $R_{Jac}/R_{99\%}$ a linear least square fit (dotted lines) was fitted to the data: The more compact the star cluster at the beginning of its evolution the higher the value of Γ_{MST} at the end. Thus more compact star clusters preserve their compactness for the most massive stars even if the whole cluster expands considerably (compare Figure 7.9). This is due to the shorter relaxation time of the massive stars.

7.5. Velocity dispersion, kinematic distance and cluster shape

The third part of this work deals with the velocity dispersion within the star cluster, and the effect of the distance measurements with the convergent point method. For the calculations the ensemble 2750W6 with a value $\xi = 2/5$ was used.

7.5.1. Velocity dispersion

To investigate the velocity dispersion of the Hyades for the ensemble 2750W6 the velocity dispersion according to Equation 3.27 was calculated. For four different radii ($r < 3$ pc, 9 pc, 18 pc and 30 pc) from the cluster centre, the eigenvalues and eigenvectors of the velocity dispersion tensor were determined. In addition, the kinetic energy and the gravitational potential energy of the stars within this radii (neglecting the gravitational force of the outer stars) was calculated. The resulting mean values and their standard errors for the ensemble 2750W6 and the perpendicular velocity dispersion for the observations are shown in Table 7.5. Since the observational data is obtained from the convergent point method, the radial velocity is predicted such that there is, technically speaking, no complete three dimensional velocity information. A calculation of the three dimensional velocity dispersion from a subsample with measured radial velocities was not practicable due to large measurement errors. The same problem arises when Perryman et al. [1998] tried to determine the velocity dispersion for Hyades stars from Hipparcos data (see within Röser et al. [2011, sec. 7]). Therefore, for the observation, only the perpendicular velocity dispersion was calculated and compared to the perpendicular velocity dispersion calculated from the simulated data. For the observations the perpendicular velocity dispersion corrected for the measurement errors within the 9 pc from the cluster centre is $\sim 0.6 \text{ km}\cdot\text{s}^{-1}$. The uncorrected value is calculated to $\sim 0.9 \text{ km}\cdot\text{s}^{-1}$. Hence there is a large uncertainty in determination of the velocity dispersion in the observations.

For the simulation the three dimensional velocity dispersion comes out to be $\sim 0.5 \text{ km}\cdot\text{s}^{-1}$ at which the dispersion in the centre is slightly higher than in the whole volume of radius 9 pc. The comparison of the value for σ_{perp} with the three dimensional velocity dispersion shows that the perpendicular velocity dispersion with a value of $\sim 0.3 \text{ km}\cdot\text{s}^{-1}$ within 9 pc is comparable to the one dimensional velocity dispersion,

7.5. Velocity dispersion, kinematic distance and cluster shape

Table 7.5.: Velocity dispersion, kinetic energy and potential energy of the Hyades for stars within $r < 3$ pc, 9 pc, 18 pc and 30 pc from the cluster centre. For the observation the value corrected for measurement errors and the uncorrected value are shown.

Quantity	Value	
	Simulation	Observation
	corrected	uncorr.
$r < 3$ pc		
E_{kin} [M _{sun} km/s]	16.233 ± 1.812	
E_{pot} [M _{sun} km/s]	32.387 ± 3.295	
E_{pot}/E_{kin}	1.995 ± 0.305	
σ [km·s ⁻¹] (from pot. energy)	0.520 ± 0.028	
σ [km·s ⁻¹]	0.515 ± 0.010	
σ_x [km·s ⁻¹]	0.263 ± 0.008	
σ_y [km·s ⁻¹]	0.293 ± 0.009	
σ_z [km·s ⁻¹]	0.328 ± 0.006	
σ_{perp} [km·s ⁻¹]	0.321 ± 0.007	0.734 ± 0.069
σ_{perp}/σ	0.623 ± 0.007	0.938
$r < 9$ pc		
E_{kin} [M _{sun} km/s]	38.504 ± 3.574	
E_{pot} [M _{sun} km/s]	60.864 ± 4.645	
E_{pot}/E_{kin}	1.581 ± 0.191	
σ [km·s ⁻¹] (from pot. energy)	0.44 ± 0.07	
σ [km·s ⁻¹]	0.478 ± 0.007	
σ_x [km·s ⁻¹]	0.232 ± 0.007	
σ_y [km·s ⁻¹]	0.262 ± 0.006	
σ_z [km·s ⁻¹]	0.326 ± 0.003	
σ_{perp} [km·s ⁻¹]	0.307 ± 0.005	0.618 ± 0.037
σ_{perp}/σ	0.642 ± 0.014	0.958
$r < 18$ pc		
E_{kin} [M _{sun} km/s]	48.003 ± 3.907	
E_{pot} [M _{sun} km/s]	65.143 ± 4.665	
E_{pot}/E_{kin}	1.357 ± 0.146	
σ [km·s ⁻¹] (from pot. energy)	0.41 ± 0.12	
σ [km·s ⁻¹]	0.493 ± 0.005	
σ_x [km·s ⁻¹]	0.266 ± 0.003	
σ_y [km·s ⁻¹]	0.255 ± 0.006	
σ_z [km·s ⁻¹]	0.326 ± 0.004	
σ_{perp} [km·s ⁻¹]	0.313 ± 0.004	0.779 ± 0.037
σ_{perp}/σ	0.661 ± 0.011	1.129
$r < 30$ pc		
E_{kin} [M _{sun} km/s]	61.598 ± 3.918	
E_{pot} [M _{sun} km/s]	66.834 ± 4.631	
E_{pot}/E_{kin}	1.085 ± 0.101	
σ [km·s ⁻¹] (from pot. energy)	0.40 ± 0.12	
σ [km·s ⁻¹]	0.546 ± 0.005	
σ_x [km·s ⁻¹]	0.339 ± 0.005	
σ_y [km·s ⁻¹]	0.258 ± 0.005	
σ_z [km·s ⁻¹]	0.341 ± 0.005	
σ_{perp} [km·s ⁻¹]	0.326 ± 0.004	0.969 ± 0.036
σ_{perp}/σ	0.597 ± 0.009	1.309

7. Simulation results

Table 7.6.: Present-day axis ratios and orientation of the velocity ellipsoid and axis ratio and orientation of the velocity ellipsoid after 12 Myr of evolution calculated from the simulations for four radii regions of the Hyades. A represents the highest semi-major axis, C the lowest. The angle Ψ is measured between the projection of the eigenvector to the highest eigenvalue onto the xz-plane and the x-axis, Φ is the angle between the projection of the same eigenvector onto the xy-plane and the x-axis and Θ is measured between the y-axis and the projection of the eigenvector to the eigenvalue B onto the zy-plane (compare Figure 3.2).

	$\frac{B}{A}$	$\frac{C}{A}$	$\Psi [^\circ]$	$\Phi [^\circ]$	$\Theta [^\circ]$
r< 3 pc					
Model present-day	0.83	0.50	3.59	2.56	8.12
Model start	0.81	0.76	9.54	12.67	37.12
r< 9 pc					
Model present-day	0.73	0.41	3.21	23.31	4.04
Model start	0.94	0.75	6.12	3.56	1.04
r< 18 pc					
Model present-day	0.61	0.43	7.05	57.23	2.34
Model start	0.95	0.65	3.87	3.46	0.76
r< 30 pc					
Model present-day	0.49	0.42	13.07	78.56	79.02
Model start	0.95	0.55	3.77	4.28	0.51

although it is slightly too high such that the ratio of σ_{perp} to σ is slightly higher than the expected value of $\frac{1}{\sqrt{3}} \approx 0.58$. Furthermore the velocity dispersion in z-direction is for all radii larger than the velocity dispersion in x- or y-direction.

Comparing the velocity dispersion perpendicular to the direction towards the convergent point between simulation and observation reveals a difference of about a factor of two between those two values in all considered radii regions. This is consistent with the results Röser et al. [2011] get for their sample of stars. They derived the velocity dispersion in three dimensions from the perpendicular velocity for their sample of the Hyades, obtaining values ranging between $(0.88 \pm 0.11) \text{ km}\cdot\text{s}^{-1}$ and $(0.74 \pm 0.21) \text{ km}\cdot\text{s}^{-1}$ for different mass bins and different radii of $r < 9 \text{ pc}$ and $r < 3 \text{ pc}$ (see Röser et al. [2011, Table 3]). The velocity dispersion for four different mass intervals for the simulation

can be found in Table A.3 in the Appendix. The values Röser et al. [2011] calculated for σ_{perp} is about a factor of two greater than the one they obtained from the virial theorem. There are two explanations for this. Firstly, the measurement of the proper motions from which the perpendicular velocity is derived is somewhat inaccurate. Hence the velocity dispersion turns out to be too high, or the measurement errors are underestimated such that the correction for them is too low, which also leads to an observed velocity dispersion higher than the real one. Since the correction for the measurement errors is very large it is possible that the proper motion measurements are one reason for the difference. As a second reason it might be, that there are stars within the observed sample which have an unresolved faint companion. This raises the velocity dispersion in the cluster due to the orbital motion of the two stars. For detailed discussion of the velocity dispersion within the observations see Röser et al. [2011, sec. 7].

The inner part of the star cluster, namely the region within 3 pc, is consistent with the virial theorem. Whereas within 9 pc the ratio of potential energy and kinetic energy differs much from the value of two. This is due to the fact that the Hyades are not an isolated system for which the virial theorem holds but a system perturbed in the outer parts by the tidal field of the Galaxy. Furthermore, the velocity dispersion calculated from the potential energy for this two regions matches the one calculated from the velocity dispersion tensor. In the regions within 18 pc and 30 pc the calculated velocity dispersion from the virial theorem deviates from that calculated from the velocity dispersion tensor even if for the 18 pc region it still matches the value from the dispersion tensor within its uncertainty ranges. Nevertheless for this radii regions the virial theorem was not expected to hold, so that this calculation can be treated as an estimate for the deviation from equilibrium.

The squared axis ratios of the velocity ellipsoid for the best fitting model of ensemble 2750W6 and its orientation in the Galactic coordinate system, according to the prescription in subsection 3.3.2, was calculated for both the present-day and the start of the simulation (about 12 Myr). The largest semi-major axis is named A , the second highest B and the lowest C . The results for the four radii regions used above are shown in Table 7.6. The present-day velocity ellipsoid is strongly flattened with the largest semi-major axis (but the lowest velocity dispersion) in nearly x direction. In the inner part (3 pc and 9 pc) the velocity ellipsoid is nearly aligned with the coordinate system

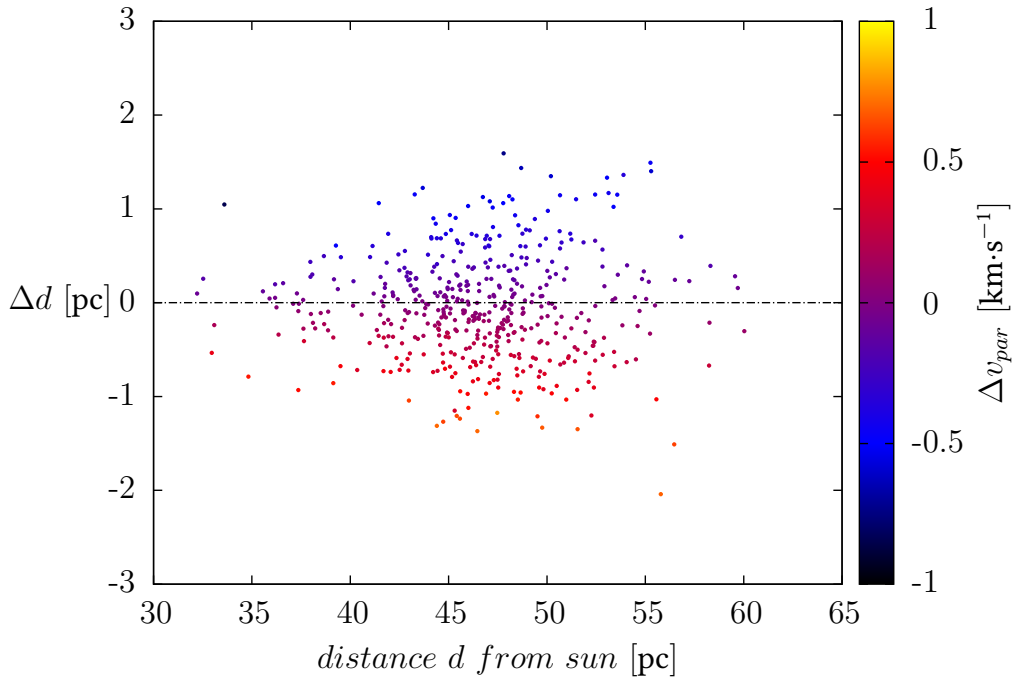


Fig. 7.12.: Distance change due to distance determination with the convergent point method for Hyades stars within 15 pc from the cluster centre. The distance dispersion is (0.55 ± 0.03) pc. For each star the velocity difference between the velocity parallel to the direction towards the convergent point, determined from the actual velocity given by the simulation, and the one determined by the convergent point method is color coded.

with the smallest velocity dispersion in x-direction and the highest in z-direction. With increasing radius the inclination of the angle Φ increases due to the tidal tails, such that for the whole 30 pc region the orientation in the xy-plane is rotated by nearly 80° . Hence the leading and trailing tidal tail (compare top left picture in Figure 7.15) run nearly parallel to the y-axis.

7.5.2. Kinematic distance

The simulation provides full position and velocity information for all stars. Therefore a comparison between the distance determined by the convergent point method and the real distance of a star is possible. In order to achieve proper motion information for

every star from the simulation the proper motion with respect to its position on the sky is calculated from the given space velocity according to Equation 4.4. From the cluster centre of mass velocity the direction towards the convergent point for each star position is calculated. Then the rotation from Equation 4.7 is applied to get the proper motion components in direction to the convergent point and perpendicular to it. In the next step the distance to every star is calculated with Equation 4.10 and compared to the original value. The distance change for the stars within 15 pc from the cluster centre as a function of the distance from the sun is shown in Figure 7.12. If all stars were selected the contamination of the distance change from the outer stars, mainly in the beginning of the tidal tails, leads to a systematic asymmetry (see Figure A.3b in the Appendix). Therefore, only the region up to 15 pc was chosen for comparison. The distance change is symmetric with a maximum distance change of about 2 pc for the stars with a distance of about 47 pc to 50 pc from the sun. Anyway these are not necessarily stars in the centre of the star cluster, but those whose distance from the Sun is of these values (see color coding in Figure A.3b). Therefore this can also be stars from the outer parts of the star cluster, which explains that the distance change at the “centre distance” of 47 pc to 50 pc is the highest although the velocity dispersion in the centre is the lowest. The color coding shows the velocity difference between the assumed cluster velocity in the direction towards the convergent point at the position of the star and its actual velocity in this direction. This indicates clearly, that, due to their internal velocity dispersion, for those stars which have a velocity component in direction towards the convergent point larger than the assumed cluster centre of mass velocity for this point on the sky, a distance lower than the original distance is calculated. For those stars which have a velocity component in direction towards the convergent point smaller than assumed, a larger distance is calculated. This is the result one would expect since a lower velocity leads to a lower calculated proper motion and this means a star is farther away from the Sun.

The dispersion of the distance change is $\Delta_{dist} = (0.55 \pm 0.03)$ pc. To check whether the distance change could be due to internal velocity dispersion one can look at the ratios

$$\frac{\Delta d}{d} \quad \text{and} \quad \frac{\Delta v}{v} \quad (7.6)$$

of the distance change Δd to the distance d of the stars from the sun and the velocity

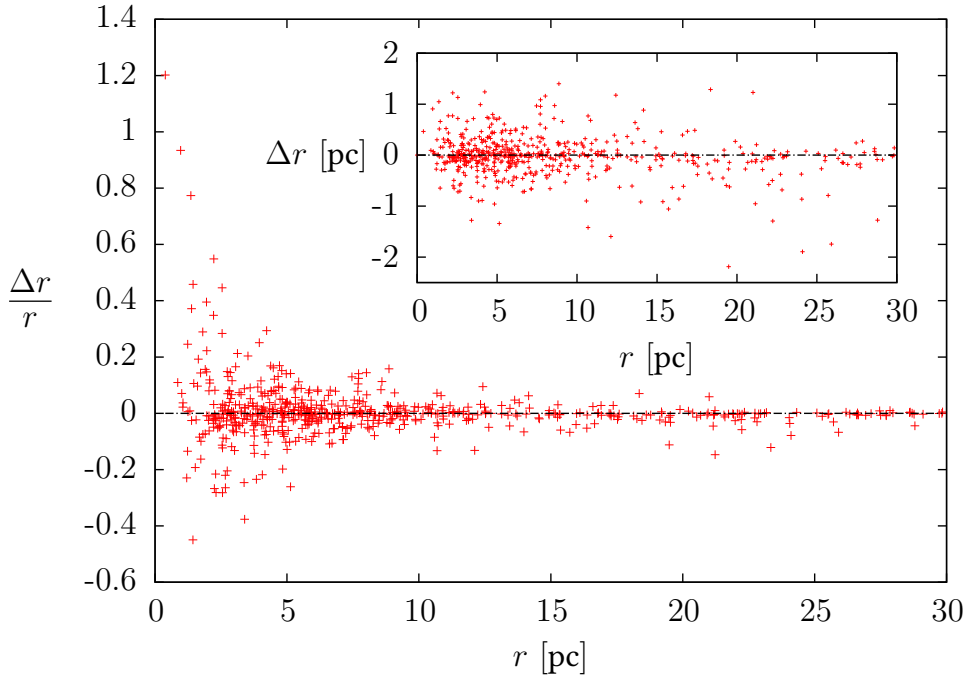


Fig. 7.13.: Relative radius change for Hyades stars within 30 pc from the cluster centre. The inset shows the absolute radius change for the stars within 30 pc from the cluster centre.

change Δv to the actual velocity v . These ratios are connected via the Equation 4.9 in the following way:

$$\frac{\Delta v}{v} = \frac{\Delta \mu}{\mu} = \frac{\Delta \varpi}{\varpi} = \frac{\Delta d}{d + \Delta d} \quad (7.7)$$

where μ and $\Delta \mu$ are the proper motion and the proper motion change respectively. ϖ and $\Delta \varpi$ refer to the secular parallax and its change. For small distance changes Δd compared to the distance d this can be approximated by:

$$\frac{\Delta v}{v} \approx \frac{\Delta d}{d} \quad (7.8)$$

With $\Delta v = \sigma \approx 0.5 \text{ km}\cdot\text{s}^{-1}$ the velocity dispersion and $v \approx 50 \text{ km}\cdot\text{s}^{-1}$ the cluster space velocity (this must be used because it is the velocity from which the proper motion is calculated) one obtains a value of $\Delta v/v = 0.01$. With the dispersion in the distance determination of $\Delta_{dist} = 0.56 \text{ pc}$ and a distance of $d \approx 50 \text{ pc}$ of the Hyades from the sun one calculates the ratio $\Delta d/d \approx 0.01$. This gives a very good agreement for the

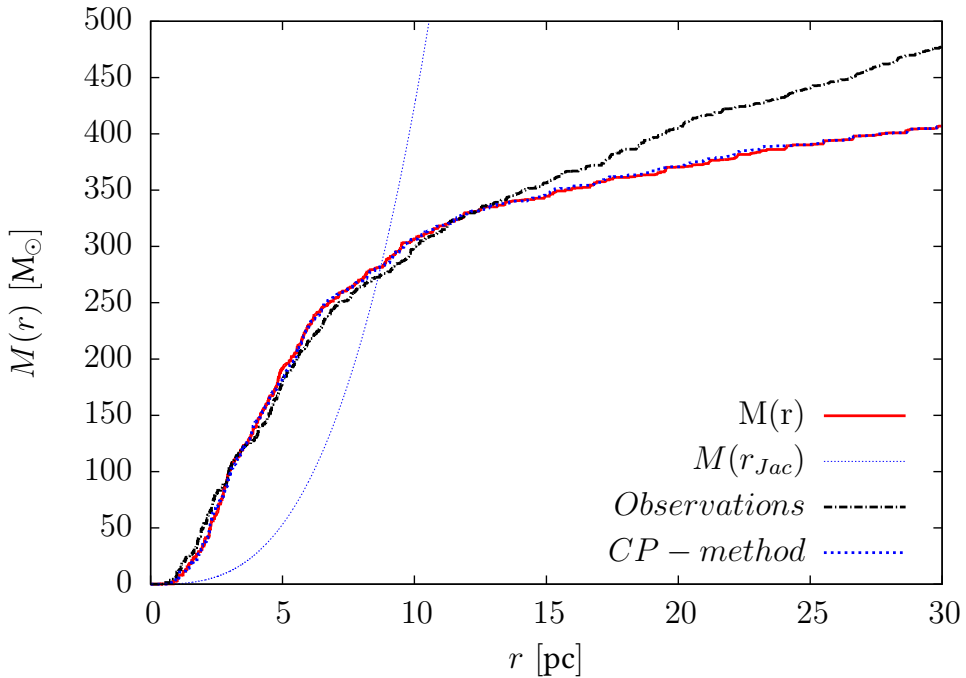


Fig. 7.14.: Present-day cumulative mass profile of the Hyades within 30 pc from the cluster centre. The *black* line shows the observational data, the *red* line shows the pure simulated data and the *blue* line shows the cumulative mass profile calculated under the usage of the convergent point method for the distance determination of the stars.

Equation 7.8 and supports the assumption that the distance change is related to the internal velocity dispersion of the stars. Nevertheless this leads to a systematic error in the distance determination up to $\sim 5\%$.

The relative radius change of all stars compared to the cluster centre and the absolute radius change is shown in Figure 7.13. However, since the mean distance change is nearly zero, the impact on the cumulative mass profile is rather small. A comparison of the cumulative mass profile of the original distance and the one calculated from the convergent point method is shown in Figure 7.14. The two cumulative mass profiles are similar.

Table 7.7 shows the values of the perpendicular velocity calculated with the actual distance and the distance calculated with the convergent point method. A recalculation of the perpendicular velocity dispersion for the best fitting model of ensemble 2750W6 after determining the distances of the stars with the convergent point method shows

Table 7.7.: Perpendicular velocity dispersion calculated before and after determining the distances of the stars with the convergent point method for stars within $r < 3$ pc, 9 pc, 18 pc and 30 pc from the cluster centre for the present-day state. The calculation was applied to the best fitting model of ensemble 2750W6.

Quantity	Value			
	r < 3 pc	r < 9 pc	r < 18 pc	r < 30 pc
σ_{perp}	0.332	0.299	0.312	0.330
$\sigma_{perp,neu}$	0.332	0.298	0.311	0.329

no significant difference in the velocity dispersion. Hence the difference of a factor of two between observed velocity dispersion and calculated velocity dispersion in the simulation is not due to the calculation of the observed velocity from the proper motion with the kinematic parallax.

7.5.3. Cluster shape

In a final step, a detailed analysis of the Hyades shape was done. For the best fitting model of ensemble 2750W6 and the observations the second order momenta tensor of the Hyades space coordinates according to Equation 3.25 was calculated and transformed into diagonal form. Then the axis ratios of the semi-major axis were calculated and the orientation of the principal axis relative to the coordinate axis of the Galactic coordinate system was determined. The results are shown in Table 7.8 where the axis ratios are, once again, the ratios of the squared semi-major axis lengths. These values are qualitative, because without using the other models the random noise of the ensemble was neglected, and for the observations the measurement errors for the position of the stars were also neglected. However, the main feature revealed by this analysis is an elongated shape with the highest extension in x-direction and the smallest in z-direction. This is the shape one would expect from the effective potential given in Equation 3.23 and which can be seen in Figure 7.15. Nevertheless the axis ratios of $y/x = 2/3$ and $z/x = 1/2$ calculated from the effective potential are only reached for the whole 30 pc region and not, as expected, for the Jacobi radius of about 9 pc. For the star cluster up to the Jacobi radius, the axis ratios $\sqrt{B/A} = 0.94$ and $\sqrt{C/A} = 0.89$ are calculated. This means the extension is nearly the same for the highest and the

Table 7.8.: Axis ratios and orientation of semi-major axis of the second order momenta tensor of the Hyades space coordinates for stars within $r < 3$ pc, 9 pc, 18 pc and 30 pc from the cluster centre for the present-day state and the start of the best fitting model of the simulations as well as for the observations. The symbols are the same as for the velocity ellipsoid. For the observation the numbers in parentheses refer to the clean sample with $v_{perp} < 2 \text{ km}\cdot\text{s}^{-1}$.

Quantity	Value				
	$\frac{B}{A}$	$\frac{C}{A}$	$\Psi [^\circ]$	$\Phi [^\circ]$	$\Theta [^\circ]$
r< 3 pc					
Model present-day	0.85	0.80	16.208	41.38	9.84
Model start	0.95	0.93	30.01	52.81	44.74
Observations	0.86 (0.85)	0.72 (0.72)	28.82 (27.83)	38.51 (37.57)	4.49 (3.66)
r< 9 pc					
Model present-day	0.89	0.79	1.78	5.30	13.83
Model start	0.91	0.89	5.07	26.91	13.61
Observations	0.83 (0.84)	0.76 (0.76)	3.76 (3.68)	3.48 (4.79)	21.10 (21.26)
r< 18 pc					
Model present-day	0.59	0.49	1.36	22.85	9.09
Model start	0.97	0.90	0.15	18.94	7.82
Observations	0.77 (0.799)	0.63 (0.64)	4.55 (1.26)	24.44 (24.70)	23.28 (26.45)
r< 30 pc					
Model present-day	0.46	0.37	2.82	39.00	0.06
Model start	0.98	0.91	5.55	31.70	5.51
Observations	0.71 (0.92)	0.59 (0.66)	1.87 (3.95)	33.24 (12.22)	19.93 (5.47)

second highest semi-major axis and slightly flattened in the third direction. Thus the Hyades have a oblat shape and not as expected a nearly prolat shape. This may be due to evolutionary effects and perturbations during 625 Myr of evolution, whereas the axis ratios calculated from the effective potential are just an unevolved case under the influence of a tidal field. Moreover, for the calculation of the second order momenta all stars in a spherical volume with certain radius around the cluster centre were used and not, as Figure 3.1 implies, an ellipsoidal volume. Apart from the outer regions of the star cluster, where the tidal tails dominate the simulations and the contamination with field stars is high for the observation, the values of the axis ratios of observation and simulation agree. The top left panel in Figure 7.15 shows well the leading (in positive x- and y-direction) and trailing tail (in negative x- and y-direction) of the star cluster.

7. Simulation results

The orientation of the star cluster is most reliably for the stars within the Jacobi radius of 9 pc because for this region most stars can be assumed as gravitationally bound and, furthermore, the tidal tails are not dominating. Beyond the 9 pc region the tidal tails dominate the orientation of the star cluster (whose orientation is also interesting to calculate) and in the inner part the star cluster should nearly be spherical such that the determination of the orientation angles is not that reliable. The cluster ellipsoid up to 9 pc has its major principal axis almost pointing to the x-direction. The angle between the projection of this principal axis onto the xz-plane and the x-axis is about $\Psi = 1.8^\circ$. For the angle between the projection of the major principal axis on the xy-plane and the x axis a value of about $\Phi = 5^\circ$ is calculated. In contrast, the beginning of the tidal tails at 30 pc lies nearly in the xy-plane with an angle $\Phi = 39^\circ$ between the x-axis and the direction of the major principal axis in the xy-plane (for the velocity ellipsoid a value of $\Phi \approx 80^\circ$ was calculated). Overall the observational data shows the same trend as the simulation data, although some values differ considerably, e.g. the Θ -value. But this can only be a qualitative analysis since uncertainty ranges for both, simulations and observations are not given. For detailed observational analysis see also Röser et al. [2011, sec. 5.1]. The values calculated there are in good agreement with the ones calculated here.

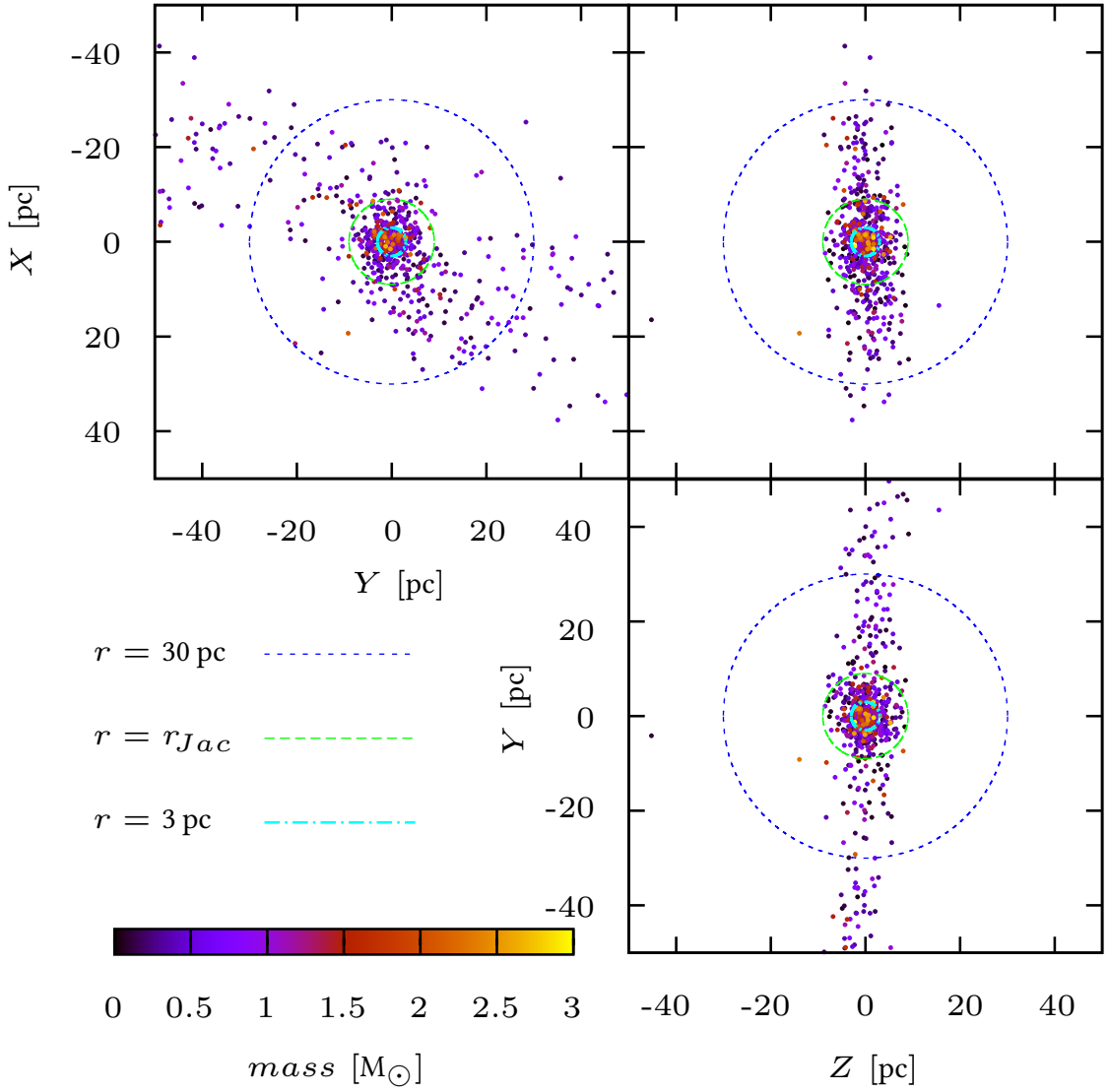


Fig. 7.15.: Present-day spatial distribution of the Hyades stars. The coordinate axis are aligned with the galactic coordinate system while the origin is put into the cluster barycentre. *The top left* picture shows the Hyades in the xy-plane, *the top right* picture shows the Hyades in the xz-plane and *the bottom right* picture shows the Hyades in the yz-plane. The color coding shows the masses of the stars, the dark blue circle shows a radius of 30 pc from the cluster centre, the green circle shows the 9 pc radius and the light blue one the 3 pc radius from the cluster centre.

8. Conclusion

In the framework of this thesis the ensemble 2750W6, an improved model of the Hyades adapted from new PanSTARRS1 observations by Goldman et al. [in press], was investigated to study the dynamics of the star cluster and the effects of the distance determination with the convergent point method. In a first step the scattering of the ensemble due to the random initialization of the model IMF in the N -body code was studied. From this, a high dispersion in the cumulative mass profile was found, while the effect on the present-day mass function was rather small. A quantitative measure of the agreement of the cumulative mass profiles was given by a Kolmogorov-Smirnov-test. In the second part, the effect of the initial ratio of R_{Jac} to $R_{99\%}$ on the evolution of the Hyades was investigated and an initial Roche Lobe overfilling of the Hyades discovered. Detailed analysis was undertaken for the cumulative mass profile and the mass segregation. For this purpose the ratio of half-mass radius to Jacobi radius as a measure of compactness of the Hyades cluster was calculated for models with different initial ratios of R_{Jac} to $R_{99\%}$. The results were derived as a function of initial ratio of R_{Jac} to $R_{99\%}$ and compared to the present-day value of the Hyades. This showed that the Hyades with a present-day value of $R_{50\%}/R_{Jac} = 0.57$ should initially started evolution with a value of 0.3 for the initial ratio of R_{Jac} to $R_{99\%}$. This highly overfilled initial state is compatible with the theory of nearly instantaneous expulsion of the primordial gas of the molecular cloud at the time when the stars start hydrogen burning. The dynamical time is far longer than the time scale needed for the gas expulsion, therefore the stars could not follow the change in potential and the star cluster starts evolving as an overfilled cluster. Furthermore it was shown that this value can be derived from the star forming efficiency of the molecular cloud and its tidal radius. Another interesting feature revealed by this analysis is that the final ratio of half-mass radius to Jacobi radius is nearly independent of the initial ratio of R_{Jac} to $R_{99\%}$ if this value is higher than 1. The analysis of the initial ratio of R_{Jac} to $R_{99\%}$ on the mass

8. Conclusion

segregation using the minimum spanning tree method showed a dependency of the degree of mass segregation on the initial ratio of $R_{Jac}/R_{99\%}$. The more compact the star cluster is, when it starts its evolution, the higher the degree of mass segregation at the present time, given that the different star cluster models end up with nearly the same value for the Jacobi radius.

The investigation of the effect of the convergent point method on the distance determination yield that the determined distance implies a systematic error of up to maximal 4% due to the internal velocity dispersion in the cluster. This is an intrinsic property of the convergent point method and can be explained by the assumption that all stars share the same space velocity. But since the stars in the cluster are in orbital motion around the cluster centre this is not valid. Nevertheless, the effect on star cluster properties like the cumulative mass profile are negligible since the mean distance error is zero. Furthermore the prediction of the convergent point method, that the perpendicular velocity can hold as an estimate of the velocity dispersion within the cluster, was examined. This study revealed a difference of a factor of two between the simulated perpendicular velocity dispersion and the observed one. There are two different explanations for this phenomenon, first the measurement errors of the proper motions are underestimated and hence the correction for them is too small or the larger velocity dispersion in the observations is caused by unresolved binary systems. Since all simulations in this work are single star simulations, the second explanation can be tested by running further simulations with binary systems.

The dynamics of the Hyades in the model were further tested by calculating the ratio of potential and kinetic energy, and comparing it to that for virial equilibrium. For the inner regions, up to the Jacobi radius, the Hyades are nearly in virial equilibrium. For the outer regions, the virial equilibrium is disturbed by the tidal forces of the Galaxy pulling the stars into the tidal tails. Further efforts were made by calculating the orientation of the velocity ellipsoid and the cluster shape of the Hyades in the simulation. The velocity ellipsoid comes out to show the highest velocity dispersion in nearly z-direction, perpendicular to the Galactic plane, while the values for the other two semi-major axis are almost the same. Throughout the whole cluster an inclination for the velocity ellipsoid in the xy-plane due to the tidal forces of the Galaxy can be measured. The cluster shape is a flattened ellipsoid, almost aligned with the Galactic coordinate system with the largest extension in x-direction towards the Galactic centre

and the lowest in z-direction.

The mass loss, the luminosity function and the stellar evolution were not analyzed. These quantities would serve as further possibilities of comparison between simulation and observation. In this thesis some quantities were just calculated for one model or just the simulations without calculating the corresponding quantities for the observations. The former quantities can merely be used as qualitative analysis since the N -body noise was neglected, the latter ones are analysis of the model and have to be compared to the observations in further studies to quantify the quality of the models. Furthermore the effect of binary systems in the star cluster were not investigated. Since the orbital motion of binary stars is much larger than the orbital motions of the stars around the cluster centre, the inclusion of binaries in the simulation could solve the problem of the inconsistency between the velocity dispersion of the simulations and the observations. For this purpose further simulations especially including binaries are required.

A. Appendix

A.1. Physical constants

Constants	
Gravitational constant	$G = (6.673\,84 \pm 0.000\,80) \cdot 10^{-11} \text{ m}^3 \cdot \text{kg}^{-1} \cdot \text{s}^{-2}$
	$G = 4.5179 \cdot 10^{-30} \text{ pc}^3 \cdot M_{\odot}^{-1} \cdot s^{-2}$
	$G = 4.48 \cdot 10^{-3} \text{ pc}^3 \cdot M_{\odot}^{-1} \cdot \text{Myr}^{-2}$
	$G = (222.3)^{-1} \text{ pc}^3 \cdot M_{\odot}^{-1} \cdot \text{Myr}^{-2}$
Mass of the sun	$1 M_{\odot} = 1.989 \cdot 10^{33} \text{ g}$
Parsec	$1 \text{ pc} = 3.085\,678\,02 \cdot 10^{18} \text{ cm}$
Megayear	$1 \text{ Myr} = 3.155\,814\,998\,4 \cdot 10^{13} \text{ s}$
Solar radius	$R_0 = (8.0 \pm 0.5) \text{ kpc}$
Circular frequency at 8 kpc	$9.488 \cdot 10^{-16} \text{ s}^{-1}$
Circular speed at 8 kpc	$234.215\,36 \text{ km} \cdot \text{s}^{-1}$
κ (conversion of proper motion)	4.740 47
Conversion	
	$1 \text{ pc} \cdot \text{Myr}^{-1} = 0.977\,775\,320 \text{ km} \cdot \text{s}^{-1}$
	$1 \text{ km} \cdot \text{s}^{-1} = 1.022\,729\,84 \text{ pc} \cdot \text{Myr}^{-1}$

A.2. Detailed discussion of the Kolmogorov-Smirnov-test

The Kolmogorov-Smirnov-test analyses whether two random variables are generated by the same empirical distribution function. Therefore the two cumulative distribution functions are calculated and the maximum vertical difference between the two functions is calculated. Since this statistical test should be used to determine whether the simulated cumulative mass function follows the same distribution than the observed one the two

A. Appendix

cumulative mass profiles are normalized. But this is in special cases misleading as will be discussed below. Consider a reference cumulative profile (blue line in the left picture in Figure A.1) and two cumulative profiles which should be compared to this reference (red and green line in the left picture in Figure A.1). Since the Kolmogorov-Smirnov-test is sensitiv for the maximum difference of the *normalized* cumulative profiles, Figure A.1 shows clearly that for a somewhat better fitting cumulative mass profile (the green one) the Kolmogorov-Smirnov-test calculates a higher value of \hat{d} and hence a worse agreement of the two profiles than for the somewhat worse fitting profile (red one). This may be in the sense, that the red curve and the blue curve have much more the same shape (curvature and slope), the right answer but in the sense, that one would get a measure for the differences of the curves (and to this also accounts the absolute difference), this is misleading. Therefore another test has to be applied or a selection by eye for the absolute difference of the curves has to go ahead the Kolmogorov-Smirnov-test. Another statistical test for the quality of the agreement of the two profiles could be the χ^2 -test.

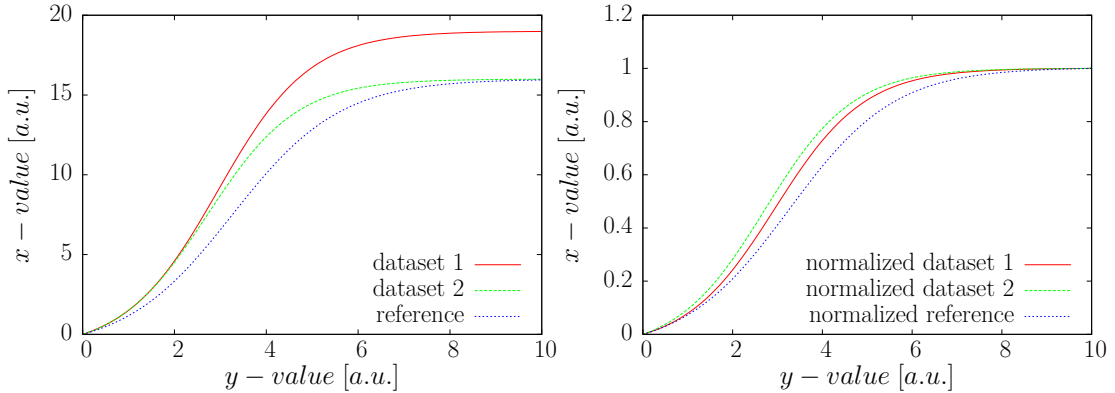


Fig. A.1.: Three arbitrary cumulative profiles from which two are compared to the third by the Kolmogorov-Smirnov-test. *The left picture* shows the calculated cumulative profiles, while *the right picture* shows the *normalized* cumulative profiles.

A.3. Additional data

Table A.1.: Present-day comparison of the number of stars and the mass within different radii from the cluster centre for observation and simulation. The values for the simulation are ensemble averages with their corresponding 1σ standard errors.

Quantity	Value	
	Observation	Simulation
Lowest mass m_l	$0.09 M_{\odot}$	$0.083 M_{\odot}$
Highest mass m_h	$2.6 M_{\odot}$	$2.7 M_{\odot}$
Maximum radius r_{max}	30 pc	30 pc
Number of stars $N(r_{max})$	773(668)	594.2 ± 57.9
Total mass $M(r_{max})$	$477.8 M_{\odot}$ ($424.71 M_{\odot}$)	$(408.6 \pm 36.5) M_{\odot}$
Jacobi radius r_J	8.4 pc(8.2 pc)	$(9.8 \pm 0.3) pc$
Number of stars $N(r_J)$	363(334)	432.5 ± 62.1
Total mass $M(r_J)$	$270.7 M_{\odot}$ ($252.8 M_{\odot}$)	$(321.2 \pm 40.9) M_{\odot}$
Core radius r_c	3 pc	3 pc
Number of stars $N(r_c)$	100(91)	123 ± 31
Total mass $M(r_c)$	$102.8 M_{\odot}$ ($95.5 M_{\odot}$)	$(119.6 \pm 25.4) M_{\odot}$
Completeness limit	$0.1 M_{\odot}$	

Table A.2.: Number of Neutron stars and White dwarfs for the ensemble 2750W6 for different radii from the cluster centre.

Quantity	2750W6
Total	
Carbon/Oxygen White dwarfs	29.7 ± 4.4
Oxygen/Neon White dwarfs	1.9 ± 1.0
Neutron stars	2 ± 1
$r < 30$ pc	
Carbon/Oxygen White dwarfs	13.2 ± 2.6
$r < 9$ pc (final - inside Jacobi radius)	
Carbon/Oxygen White dwarfs	10.9 ± 1.4
$r < 3$ pc (final - core)	
Carbon/Oxygen White dwarfs	3.5 ± 1.3

A. Appendix

Table A.3.: Comparison of velocity dispersion for different mass intervals for the best fitting model of ensemble 2750W6 for the present-day and the beginning of the simulations. Only stars within a radius of 9 pc from the cluster centre were considered.

Quantity	Value	
	Simulation present-day	Simulation start
$m < 0.4 M_{\odot}$		
σ [km·s $^{-1}$]	0.51	0.73
σ_x [km·s $^{-1}$]	0.22	0.39
σ_y [km·s $^{-1}$]	0.26	0.43
σ_z [km·s $^{-1}$]	0.38	0.44
σ_{perp} [km·s $^{-1}$]	0.33	0.43
$0.4 M_{\odot} < m < 0.8 M_{\odot}$		
σ [km·s $^{-1}$]	0.48	0.73
σ_x [km·s $^{-1}$]	0.23	0.41
σ_y [km·s $^{-1}$]	0.23	0.41
σ_z [km·s $^{-1}$]	0.35	0.45
σ_{perp} [km·s $^{-1}$]	0.30	0.44
$m > 0.8 M_{\odot}$		
σ [km·s $^{-1}$]	0.43	0.72
σ_x [km·s $^{-1}$]	0.21	0.40
σ_y [km·s $^{-1}$]	0.25	0.38
σ_z [km·s $^{-1}$]	0.27	0.46
σ_{perp} [km·s $^{-1}$]	0.26	0.42
$m > 1 M_{\odot}$		
σ [km·s $^{-1}$]	0.40	0.74
σ_x [km·s $^{-1}$]	0.20	0.41
σ_y [km·s $^{-1}$]	0.23	0.39
σ_z [km·s $^{-1}$]	0.26	0.47
σ_{perp} [km·s $^{-1}$]	0.23	0.44

Table A.4.: Initial parameters for the best fitting model of ensemble 2750W6

Quantity	Value
King Parameter W_0	6
Particle number N_0	2750
Mean stellar mass \bar{m}	$0.619 M_{\odot}$
Total mass M_0 calculated	$1702.25 M_{\odot}$
Total mass M_0 from IMF	$1696.98 M_{\odot}$
Jacobi radius r_J	15.85 pc
99% mass radius $R_{99\%}$	35.86 pc
ratio $R_{Jac}/R_{99\%}$	0.44

A.4. Additional diagrams

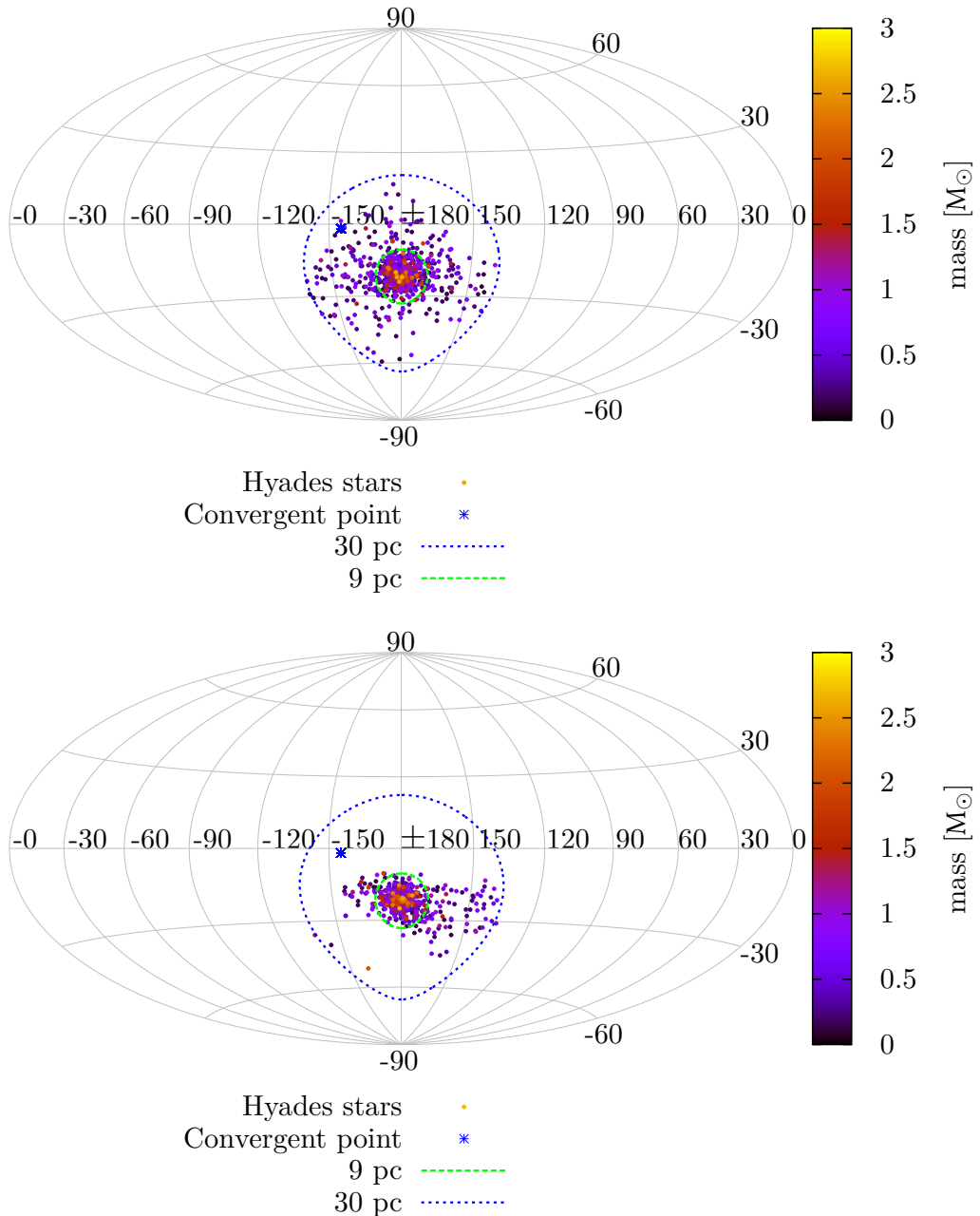
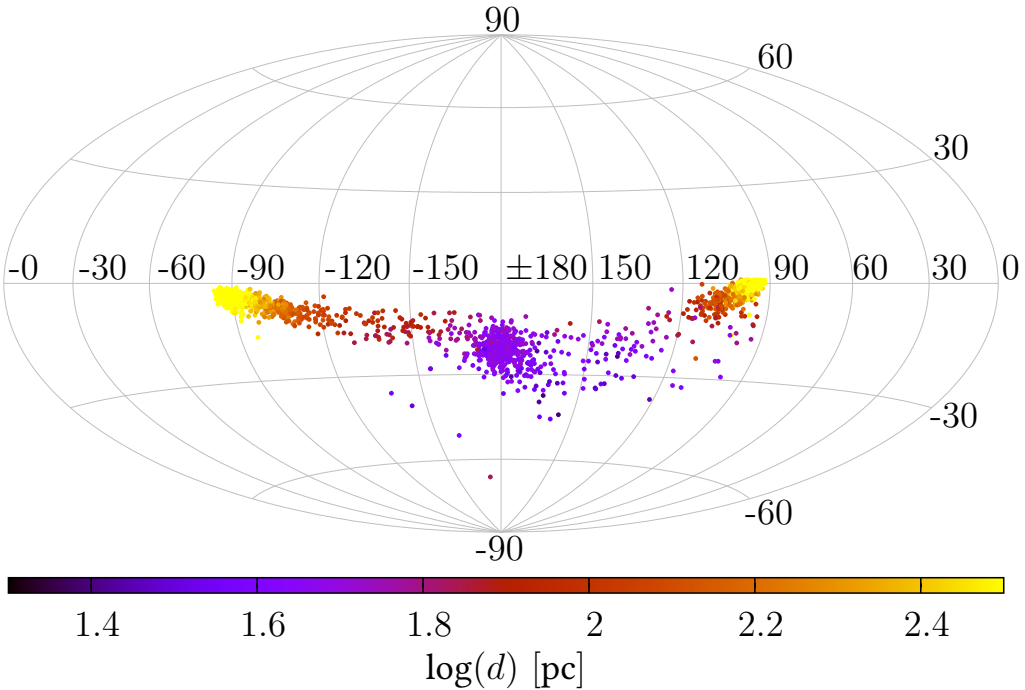
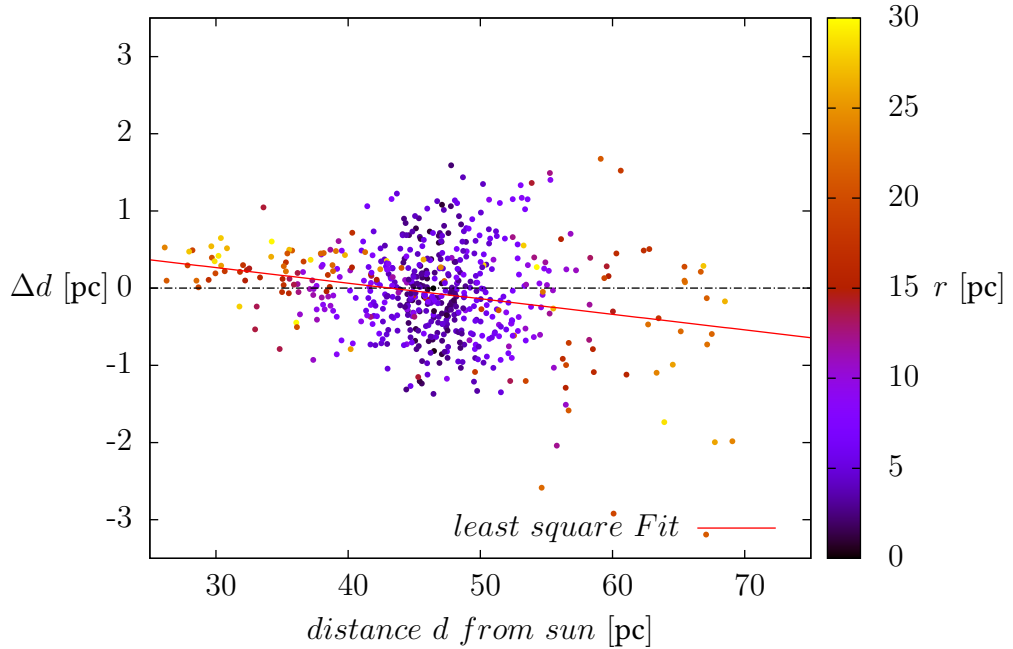


Fig. A.2.: Present day Aitoff projection of the Hyades in galactic longitude and latitude coordinates. *Top* the observations by Goldman et al. [in press], *Bottom* the best fitting model of ensemble 2750W6.



(a) Present-day Aitoff projection of the Hyades with tidal tails in galactic longitude and latitude coordinates.



(b) Distance change by usage of the convergent point method for the best fitting model of ensemble 2750W6. The color coding shows the distance of the stars from the cluster centre. The fit function for the least square fit is given by $g(x) = mx+b$ with determined parameters $m = -0.020 \pm 0.003$ and $b = (0.871 \pm 0.168)$ pc

References

- Aarseth, S. J. 1999, PASP, 111, 1333
- Aarseth, S. J. 2003, Gravitational N-Body Simulations
- Ahmad, A., & Cohen, L. 1973, Journal of Computational Physics, 12, 389
- Baumgardt, H., & Kroupa, P. 2007, MNRAS, 380, 1589
- Binney, J., & Tremaine, S. 2008, Galactic Dynamics, 2nd edn. (Princeton University Press), 920
- Casertano, S., & Hut, P. 1985, ApJ, 298, 80
- Copenhagen University, O., Institute, A. O., Cambridge, Uk, & Real Instituto Y Observatorio de La Armada, F. E. S. 2006, VizieR Online Data Catalog, 1304, 0
- Dehnen, W. 1993, MNRAS, 265, 250
- Dib, S., Gutkin, J., Brandner, W., et al. 2013, ArXiv e-prints, arXiv:1306.6338
- Ernst, A. 2012, <http://www.rzuser.uni-heidelberg.de/~ernst/nb6tidmanual.pdf>
- Ernst, A., Just, A., Berczik, P., & Olczak, C. 2011, A&A, 536, A64
- Ernst, A., Just, A., Berczik, P., & Petrov, M. I. 2010, A&A, 524, A62
- Goldman, B., Röser, S., Schilbach, E., et al. in press
- Gower, J. C., & Ross, G. J. S. 1969, Journal of the Royal Statistical Society. Series C (Applied Statistics), 18, 54
- Gürkan, M. A., Freitag, M., & Rasio, F. A. 2004, ApJ, 604, 632

References

- Hurley, J. R., Pols, O. R., & Tout, C. A. 2000, MNRAS, 315, 543
- Khalisi, E., & Spurzem, R. 2006, Version for the Cambody summerschool in Cambridge 2006
- King, I. 1962, AJ, 67, 471
- King, I. R. 1966, AJ, 71, 64
- Miyamoto, M., & Nagai, R. 1975, PASJ, 27, 533
- Nitadori, K., & Aarseth, S. J. 2012, MNRAS, 424, 545
- Olczak, C., Spurzem, R., & Henning, T. 2011, A&A, 532, A119
- Perryman, M. A. C., Brown, A. G. A., Lebreton, Y., et al. 1998, A&A, 331, 81
- Piskunov, A. E., Kharchenko, N. V., Röser, S., Schilbach, E., & Scholz, R.-D. 2006, A&A, 445, 545
- Plummer, H. C. 1911, MNRAS, 71, 460
- Roeser, S., Demleitner, M., & Schilbach, E. 2010, AJ, 139, 2440
- Röser, S., Schilbach, E., Piskunov, A. E., Kharchenko, N. V., & Scholz, R.-D. 2011, A&A, 531, A92
- Schlüter, P. 2012, Bachelor Thesis, University Heidelberg
- Schönrich, R., Binney, J., & Dehnen, W. 2010, MNRAS, 403, 1829
- Smirnov, N. 1939, Bulletin de l'Universite de Moscow, Serie internationale (Mathematiques), 2, 3
- Smirnov, N. 1948, The Annals of Mathematical Statistics, 19, pp. 279
- Spurzem, R. 1999, Journal of Computational and Applied Mathematics, 109, 407
- Tremaine, S., Richstone, D. O., Byun, Y.-I., et al. 1994, AJ, 107, 634

References

van Altena, W. F. 2013, Astrometry for Astrophysics, 1st edn. (Cambridge University Press)

van Leeuwen, F. 2009, A&A, 497, 209

List of Figures

1.1.	Tidal tails of the Hyades as they evolve in the simulation 2750W6	3
3.1.	Sketch of the last closed equipotential surface of the effective potential of a star cluster in the tidal field of the Galaxy.	19
3.2.	Star cluster ellipsoid and its orientation in the Galactic coordinate system.	21
3.3.	Rotation curve of the Milky Way	23
4.1.	Connection between space velocity and proper motion and the occur- rence of a convergent point as a result of projection	28
4.2.	Decomposition of a space velocity vector into its components	29
4.3.	Observed proper motion components parallel and perpendicular to the direction towards the convergent point	30
5.1.	Three dimensional orbit of the Hyades	37
7.1.	Average realization of the three-part broken power law initial mass function of ensemble 2750W6	52
7.2.	Average realization of the three-part broken power law mass function of ensemble 2750W6 after 625 Myr of evolution	53
7.3.	Present-day cumulative mass profile of observation and ensemble 2750W6	55
7.4.	Best-fitting model according to the Kolmogorov-Smirnov-test.	56
7.5.	Comparison of the PDMFs of observations and ensemble 2750W6 for stars within 3 pc, 9 pc and 30 pc from the cluster centre	57
7.6.	Density profile of simulation and observation	59
7.7.	Average cumulative mass for observations and ensemble 2750W6 . . .	60
7.8.	Cumulative mass profiles for different initial values $\xi = R_{Jac}/R_{99\%}$	62
7.9.	Final ratio of $R_{50\%}/R_{Jac}$ as a function of initial ratio of $\xi = R_{Jac}/R_{99\%}$. . .	63

7.10. Mass segregation for a simulation with initial ratio $R_{Jac}/R_{99\%} = 1$	66
7.11. Comparison of mass segregation for simulations with different initial ratios of $R_{Jac}/R_{99\%}$	67
7.12. Distance change due to distance determination with the convergent point method for Hyades stars within 15 pc from the cluster center.	72
7.13. Relative radius change for Hyades stars within 30 pc from the cluster centre. The inset shows the absolute radius change for the stars within 30 pc from the cluster centre.	74
7.14. Present-day cumulative mass profile of the Hyades within 30 pc from the cluster center.	75
7.15. Present-day spatial distribution of the Hyades stars.	79
A.2. Present-day Aitoff projection of the Hyades in galactic longitude and latitude coordinates.	90

List of Tables

5.1.	Galaxy parameters for the 3PLK Milky Way model	33
6.1.	Parameters of the Hyades determined from the observations	42
6.2.	Values of D_α for different statistical significances α	45
7.1.	Parameters for the determination of the scaling factor \bar{R}	50
7.2.	Initial parameters of the ensemble 2750W6	51
7.3.	Parameters of initial ratio of $R_{50\%}/R_{Jac}$ and final ratio of $R_{50\%}/R_{Jac}$ for different initial ratios of $\xi = R_{Jac}/R_{99\%}$	61
7.4.	Values for \hat{d} for the Kolmogorov-Smirnov-test for models with different values of ξ	65
7.5.	Velocity dispersion, kinetic energy and potential energy of the Hyades for stars within $r < 3$ pc, 9 pc, 18 pc and 30 pc from the cluster centre. For the observation the value corrected for measurement errors and the uncorrected value are shown.	69
7.6.	Present-day axis ratios and orientation of the velocity ellipsoid and axis ratio and orientation of the velocity ellipsoid after 12 Myr of evolution calculated from the simulations.	70
7.7.	Perpendicular velocity dispersion calculated before and after determining the distance with the convergent point method.	76
7.8.	Axis ratios and orientation of semi-major axis of the second order momenta tensor of the Hyades space coordinates for stars within $r < 3$ pc, 9 pc, 18 pc and 30 pc from the cluster centre.	77
A.1.	Present-day comparison of the number of stars and the mass within different radii from the cluster centre for observation and simulation. .	87

List of Tables

A.2.	Number of Neutron stars and White dwarfs for the ensemble 2750W6 for different radii from the cluster centre.	87
A.3.	Comparison of velocity dispersion for different mass intervals for the best fitting model of ensemble 2750W6	88
A.4.	Initial parameters for the best fitting model of ensemble 2750W6	89

Danksagung

“So long, and thanks for all the fish.”

(Douglas Adams)

Am Ende meiner Bachelorarbeit möchte mich bei allen bedanken, die mich dabei und während meines bisherigen Studiums unterstützt haben und mir somit diese Arbeit ermöglicht haben:

- Zuerst einmal möchte ich mich bei Prof. Dr. Andreas Just für die Ermöglichung der Bachelorarbeit und die sehr gute Betreuung bedanken. Wann immer es Probleme bei meiner Arbeit oder Gesprächsbedarf bei den Ergebnissen gab, hat er sich Zeit für mich genommen. Vielen Dank dafür.
- Ein ganz besonderer Dank geht an Dr. Andreas Ernst für das mehrfache Korrekturlesen meiner Arbeit sowie die viele Unterstützung mit dem Simulationsprogramm NBODY6TID und den fachlichen Rat, den ich mir jederzeit abholen konnte. Vielen Dank, Andreas.
- Ein weiterer Dank geht an Dr. Bertrand Goldman für die Bereitstellung der Beobachtungsdaten der Hyaden sowie an Dr. Siegfried Röser für die Hilfe beim Bearbeiten der Beobachtungsdaten und die Erklärungen zur CPM.
- Bei Avon möchte ich mich dafür bedanken, dass er sich die Zeit genommen hat, meine Arbeit auf Sprachrichtigkeit zu korrigieren. Thank you Avon!
- Ganz besonders möchte ich meinen Eltern danken, die mich in meinem bisherigen Lebensweg immer unterstützt und ermutigt haben, meinen Weg zu gehen.
- Ich möchte meiner Freundin Meike Kespoli danken, dass sie mir mit ständigem Rat bei Seite stand und mich am Ende immer wieder an die wichtigen Dinge meiner Arbeit erinnert hat wenn ich mal wieder in den Tiefen der L^AT_EX-Typographie versunken war und meine Zeit mit dem Ausprobieren der Möglichkeiten des Programms verbracht habe statt sinnvoll zu arbeiten.
- Zuletzt möchte ich allen anderen, die bisher ungenannt geblieben sind und die mich in meinem Studium begleitet haben, für die schöne Zeit danken.

Erklärung

Ich versichere, dass ich diese Arbeit selbstständig verfasst und keine anderen als die angegebenen Quellen und Hilfsmittel benutzt habe. Heidelberg, den 17.7.2013,